Floquet and dissipative engineering in mesoscopic systems

Memoria de la tesis presentada por

MÓNICA BENITO GONZÁLEZ

para optar al grado de Doctora en Ciencias Físicas

Departamento de Física de la Materia Condensada
Instituto de Ciencia de Materiales de Madrid (CSIC)

Directora: GLORIA PLATERO COELLO
Tutor: ALFREDO LEVY YEYATI

MADRID, FEBRERO 2017

To my parents

ACKNOWLEDGEMENTS

Durante estos años he tenido la fortuna de interaccionar con muchas personas que de alguna manera han contribuido al desarrollo de esta tesis y a las que quiero agradecer. En primer lugar, quería agradecer a mi directora de tesis, Gloria, por acogerme desde el primer día y finalmente darme la oportunidad de realizar esta tesis. También por su confianza y su cercanía. Además, quería dedicar un agradecimiento especial tanto a Fernando como a Álvaro por trabajar conmigo en los inicios, transmitiéndome todo lo que sabían y contestando a todas mis preguntas. En esta tarea también agradezco enromemente a Sigmund por su tiempo, sus consejos, su confianza en mi trabajo y su entusiasmo por enseñarme cosas.

I would also like to thank my supervisors during the stays abroad, Ignacio Cirac and Tobias Brandes, for their great hospitality and the always enlightening discussions. During that times, I was extremely lucky to discover new research fields by working with Carlos, Georg and Martin. I thank Carlos for his motivational personality and for being always available for teaching, discussing, simply helping, or enjoying the free time. I thank Georg for his hospitality and for giving me the motivation that I needed at the end of this thesis. Last but not least, I am really grateful to Martin, who taught me and supervised my work for a long time, encouraging me every day to go further. On top of that I could also learn from his organizative and writting skills.

Por si esto fuera poco, también tengo que agradecer a mis compañeros de despacho, comidas, cafés y salidas. A Fernando, por las discusiones que me sirvieron para unificar distintos puntos de vista y por ayudarme siempre con cualquier problema relacionado con el ordenador, además de por su amistad, por esas salidas, congresos, y por ser el mejor compañero de despacho. A Robert, por estar siempre dispuesto a ayudar y también a salir a ver el fútbol. A Miguel, por ser tan cercano y por interesarse siempre por mi trabajo. También a Rafa, Juanmi, Mathias, Alejandro, Fito, Yago, José Carlos, Tobias, Jordi, Guillem, Rubén, Leandro, Chema, Carlos y alguno más que me olvidaré, porque con todos he compartido algún buen rato.

I am grateful to the people of Max Planck group for their hospitality, especially Alex, for the discussions and for worrying about my adaptation to the group. I also thank Tao for his lessons and the stories, and Carlitos for being a perfect officemate. Finally I would like to thank other collegues like Yue, Erez, Gemma, Alessandro, and all the others. Of course, I also thank my collegues in Berlin for the hospitality and the organized visits to the Biergarten: Víctor, Javi, Sebastián, Wassilij, and the others.

Por supuesto, también tengo que agradecer a mis amigos físicos por lo que aprendí con ellos durante la carrera. Así, agradezco a Javi, por su gran amistad más allá de las circunstancias. También a Marta, por enseñarme tanto y por motivarme a entrar en el campo de la materia condensada. A Mar, por su locura y por los días de estudio en su casa. Y a Juan y Julio, para completar el grupo de jotas y emes. No me puedo olvidar de mis amigos no físicos, que siempre están ahí para hablarme de otras cosas más relacionadas con la vida y ayudarme a desconectar. Agradezco enormemente su amistad a Gonzalo, a Cristina y a Rubén porque nunca fallan.

Además, agradezco a mi familia por su apoyo constante y por ayudarme siempre que he necesitado algo. A mis padres, por inculcarme el valor del trabajo y el esfuerzo y por darme siempre todo lo que ha estado en su mano. A mis hermanos porque son los mejores y punto. También a mis abuelos por su cariño y a todo el resto de mi familia, sobre todo a los primos por los buenos ratos.

Finally, I would like to thank Michael for the discussions about physics, for forcing me to end them at the proper time, for the continued support, his positivity, and love.

Table of Contents

List of publications

Part of the work presented in this thesis has given rise to the following publications and preprints:

P.1 *Floquet engineering of long-range p-wave superconductivity.*
M. Benito, A. Gómez-León, V. Bastidas, T. Brandes and G. Platero. Phys. Rev. B **90**, 205127 (2014).

P.2 *Floquet Majorana fermions in superconducting quantum dots.*
M. Benito and G. Platero. Physica E: Low-dimensional Systems and Nanostructures, **74**, 608 (2015).

P.3 *Degenerate parametric oscillation in quantum membrane optomechanics.*
M. Benito, C. Sánchez-Munoz and C. Navarrete-Benlloch. Phys. Rev. A **93**, 023846 (2016).

P.4 *Edge-sate blockade of transport in quantum dot arrays.*
M. Benito, M. Niklas, G. Platero and S. Kohler. Phys. Rev. B **93**, 115432 (2016).

P.5 *Topological instabilities in ac-driven bosonic systems.*
G. Engelhardt, M. Benito, G. Platero and T. Brandes, Phys. Rev. Lett. **117**, 045302 (2016).

P.6 *Dissipative long-range entanglement generation between electronic spins.*
M. Benito, M. J. A. Schuetz, J. I. Cirac, G. Platero and G. Giedke. Phys. Rev. B **94**, 115404 (2016).

P.7 *Transport, shot noise, and topology in ac-driven dimer arrays.*
M. Niklas, M. Benito, S. Kohler, G. Platero, Nanotechnology **27**, 454002 (2016).

P.8 *Full-counting statistics of time-dependent conductors.*
M. Benito, M. Niklas, S. Kohler. Phys. Rev. B **94**, 195433 (2016).

P.9 *Topologically-enforced bifurcations in superconducting circuits.*
G. Engelhardt, M. Benito, G. Platero and T. Brandes, preprint, arXiv:1611.01467 (2016).

Abstract

External electromagnetic fields and engineered environments influence the behavior of quantum systems. The tailored application of such tools is surely a key ingredient for quantum information processing, no matter the type of quantum technology behind. This thesis focuses on the theoretical description of implementations based on recent advances of the semiconductor industry towards quantum control and confinement.

The interaction with electromagnetic fields has been intensively utilized for manipulating quantum systems, but the rather modern concept of Floquet engineering goes beyond that and provides an especially predictive tool for generating novel materials that may not exist in a static fashion. The time periodicity of the resulting models often leads to a failure of the methods commonly applied to solve quantum static problems and, even nowadays, the set of theoretical tools is not complete. Since in this thesis several periodically driven systems are analyzed, we often face the lack of effective tools and, thus, have to develop new methods.

In the context of engineered environments, the method of dissipative engineering implies a new concept applicable to the development of quantum information processing. As this ensemble of novel strategies benefits from dissipation, it fights decoherence without the need of more isolation and opens the way to long-distance quantum communication via common specific environments.

The content of this thesis is organized according to the degree of isolation of the quantum system of interest from the environment. In this way, after two introductory chapters, we present two chapters that treat periodically driven closed quantum systems, followed by two chapters about the statistics of transported charges through a weakly coupled conductor, while the last chapter is devoted to the development of a dissipative strategy to generate long-distance quantum correlations.

The emerging field of topology in condensed matter has importance along this thesis. Our main interest in the topologically non-trivial materials lies in the topological edge states they support. Firstly, we dedicate some works to the pure task of analyzing topology-related features of periodically driven systems, such as new type of edge states. Secondly, we shine some light on the interplay between topology and transport statistics and propose a way to measure the topological phase. Finally, we employ the recent development of transporting channels based on topological edge states for our already mentioned dissipative strategy which, in particular, aims at building up quantum entanglement between spatially-separated qubits.

Resumen

La aplicación de campos electromagnéticos externos y el contacto con el entorno influencia el comportamiento de los sistemas cuánticos. La utilización adaptada de estas herramientas es ciertamente un ingrediente clave para el procesamiento de información cuántica independientemente del tipo de tecnología cuántica que se emplee. Esta tesis se centra en la descripción teórica de implementaciones basadas en avances recientes de la industria de semiconductores hacia el control y confinamiento cuántico.

La interacción con campos electromagnéticos ha sido intensamente empleada para manipular sistemas cuánticos, pero existe el concepto más moderno de ingeniería vía Floquet que va más allá proporcionando una herramienta predictiva para generar nuevos materiales que no existan de forma estática. La periodicidad temporal de los correspondientes modelos a menudo invalida la posibilidad de utilizar los métodos comúnmente aplicados para resolver problemas cuánticos estáticos y hasta ahora el conjunto de herramientas no es completo. Como en esta tesis analizamos varios sistemas manipulados periódicamente, debemos desarrollar nuevos métodos para ellos.

El nuevo método de ingeniería vía disipación es aplicable también al procesamiento de información cuántica. Como este conjunto de estrategias se beneficia de la disipación, es intrínsecamente robusto frente a decoherencia y podría permitir comunicación cuántica a larga distancia mediante el uso de entornos comunes apropiados.

El contenido de esta tesis está organizado de acuerdo al grado de aislamiento del sistema cuántico de interés. Así, después de dos capítulos introductorios, presentamos dos capítulos que tratan sistemas cerrados forzados periódicamente, seguidos de dos capítulos sobre la estadística de transporte a través de conductores débilmente acoplados al entorno, mientras que el último capítulo se dedica al desarrollo de una estrategia disipativa para generar correlaciones cuánticas a larga distancia.

El emergente campo de topología en física de la materia condensada es importante a lo largo de esta tesis. Nuestro principal interés en materiales topológicamente no triviales se debe a los estados de borde topológicos que poseen. Primero dedicamos algunos trabajos a la tarea de analizar características topológicas de sistemas forzados periódicamente, como la existencia de nuevos tipos de estados de borde. Para seguir, investigamos la relación entre topología y estadística de transporte de carga y proponemos una forma de medir la fase topológica. Finalmente, empleamos el reciente avance en canales de transporte basados en estados de borde toplógicos para nuestra estrategia disipativa que, en particular, pretende generar entrelazamiento entre qubits espacialmente separados.

CHAPTER 1

INTRODUCTION

The possibility to access the quantum nature of matter at the mesoscopic level has opened a new era in condensed matter physics. Its success is based on the low dimensionality reached for the charge carriers, i.e., on the strong confinement of spatial dimensions to length scales comparable to the particle's wavelength. The semiconductor industry has been able to confine charge carriers to two dimensions (two-dimensional electron gas (2DEG)), one dimension (quantum wires) and even zero dimensions (quantum dots (QDs)) [1]; see Fig. 1.1.

Apart from a fundamental reason, the practical goal of the mesoscopic matter quantization is to include it among the serious candidates for the technological implementation of quantum information processing (QIP) [2, 3]. One may think of using this well-controlled quantum devices in a variety of ways, for instance for quantum simulation and the more ambitious concept of quantum computation, both taking advantage of unique quantum properties such as superpositions and entanglement [4]. The concept of quantum simulator means the preparation of a quantum device to act as another quantum system that we wish to simulate [5]. A universal quantum computer is a device which makes use of quantum-mechanical properties to perform operations on data [6]. Although the conditions for its fabrication are really demanding [7], nowadays there is a huge variety of candidates based on different physical systems [8–10], such as trapped ions [11, 12], cold atoms in optical lattices [13–16], cavity quantum electrodynamics [17, 18], donors in silicon [19], nitrogen-vacancy centers in diamond [20] or superconducting circuits [21].

A 2DEG is fabricated by introducing charge carriers at the interface of semiconductor material layers with different band gaps, e.g., GaAs and AlGaAs [1]. The possibility to observe physics of charges in two dimensions allowed for the discover of the quantum Hall (QH) effect in a mesoscopic physics experiment where quantized magnitudes were measured for the first time [22]. If one confines the charge carriers in two spatial dimensions, one gets a quantum wire or one-

dimensional electron gas where charges move only in one dimension. The most interesting application of these semiconducting nanowires for this thesis is that, with the appropriate ingredients, they form the basis of what is called topological quantum computation since they support very special boundary modes known as Majorana bound states (MBSs) or Majorana fermions [23–26]. Concerning the zero-dimensional systems or QDs [27, 28], there are several types. One can define them by adding potential barriers to quantum wires or carbon nanotubes or by surface gates situated on top of a 2DEG to locally deplete small regions and control the number of electrons there, often called gate-defined lateral QDs. Also self grown quantum dots in InAs are fabricated. For more details on the different types of QDs see Refs. [29–32].

It is often interesting in these confined systems to introduce an extra dimension related to time. In all the mentioned systems, the interaction with time-dependent external electromagnetic fields is a powerful tool to manipulate internal properties while keeping quantum coherence [33–38]. In particular, the application of a *periodic driving* provides a versatile method to engineer Hamiltonians, often named Floquet engineering because of the theoretical method used to treat such time-periodic systems [39–41]. Engineering by periodic driving has become a trend in the field of Bloch-band topology since it allows one to modify the topological properties in a controllable way and even to create novel phases not existent in time-independent systems [42–47].

As lateral QDs are controlled via electrical means, it is relatively easy to interchange electrons between the QD and the 2DEG and detect their charge state via current measurements. By measuring the current through a QD for different external voltages one can construct the so called stability diagrams to identify the stable regions with a fix number of electrons inside the QD and the boundaries between two (or more) charge configurations, where there might be electronic current through the QD [30, 48]. It is even experimentally possible to fabricate multiple QDs separated by a tunneling barrier and create quantum states with superpositions of states localized in spatially separated dots, which paves the way to perform scalable quantum computation [31]. Major building blocks such as initialization, single-shot readout, coherent control of single spins, and two-qubit gates between adjacent spins have been demonstrated successfully in proof-of-principle experiments [49–54]. However, at present the integration of several qubits into a scalable architecture still remains a formidable challenge [30, 55, 56]. A large amount of wiring and control electronics needs to be accommodated on a very small scale, since interactions between QDs are very short-range, limiting QIP setups to nearest-neighbor interactions. Therefore, a scalable design is likely to require *long-range* couplings over distances of several micrometers [10, 57–59].

Another challenge is the control over the undesired influences of environments, such as phonons, fluctuating charges, nuclear spins, etc., which tend to corrupt genuine quantum properties such as entanglement by a phenomenon called *decoherence*. The common strategy against this has been to isolate qubits as much as possible, but nowadays novel approaches such as *dissipative engineering* open the way to actively harness the inevitable interaction between

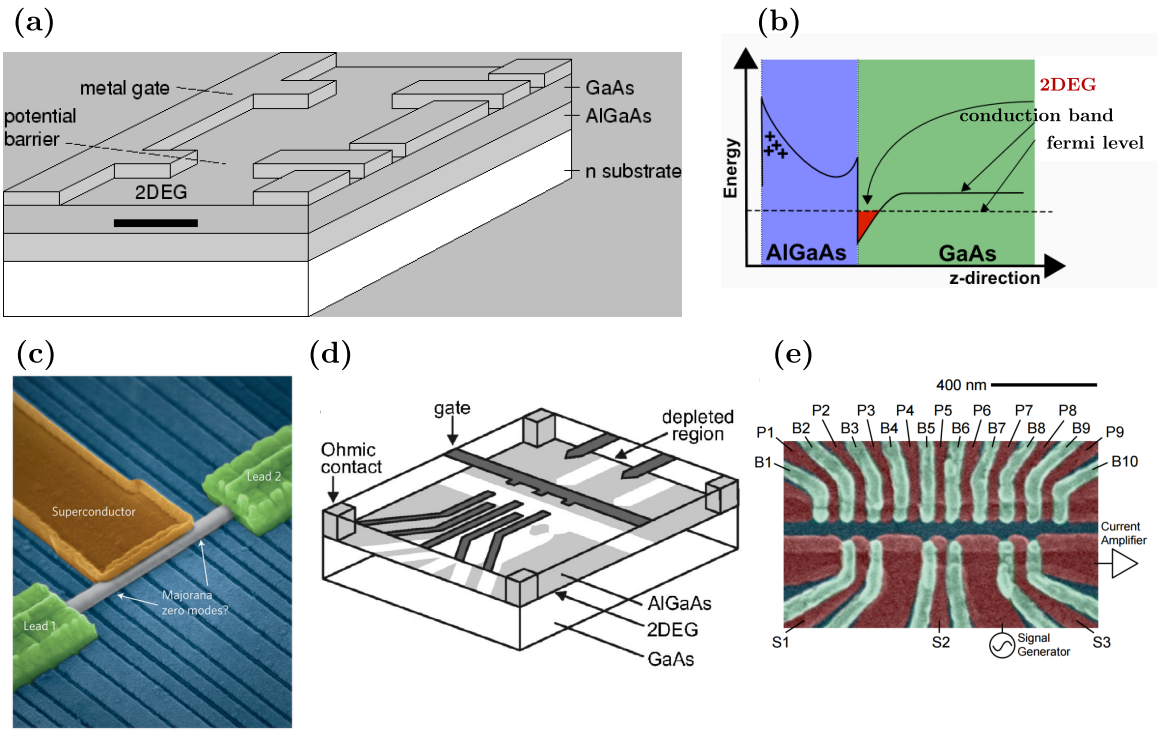

FIGURE 1.1. (a) 2DEG with electrons confined at the interface between GaAs and AlGaAs. The metallic gate induces the desired potential barrier in the plane of the 2DEG. (b) Energy profile of the heterostructure in (a). (c) Nanowire in proximity to a superconductor and connected to two metallic leads, where the appearance of MBSs is expected. (d) Schematic view of a lateral QD device defined by metal surface electrodes. Negative voltages applied to metal gate electrodes (dark gray) lead to depleted regions (white) in the 2DEG (light gray). (e) False-color scanning electron microscope image of the gate architecture to achieve a linear array of 9 QDs. Tunnel couplings are controlled using barrier gates B1, B2, ..., B10. Panel (c) is from Ref. [26], (d) from Ref. [30] and (e) from Ref. [56].

system and environment [60–68]. In this approach, which has been successfully implemented experimentally [69–72], by suitable engineering the continuous coupling of the system to its environment, dissipation turns into a driving force behind the emergence of quantum phenomena.

Outline of this thesis

Chapter 2 is devoted to introducing a few concepts utilized along this thesis. First, we explain how to treat quantum systems driven by time-periodic fields by means of Floquet theory, which allows one to get more insight into the system by means of the obtention of the time-independent

effective Hamiltonians that drive the stroboscopic dynamics. This type of Floquet engineering can also be applied to quantum systems weakly coupled to particle reservoirs, open quantum systems, whose dynamics cannot be described with a Hamiltonian but one needs a formalism that includes incoherent processes. For this purpose, we introduce a master equation formalism. Under certain conditions, an effective time-independent Hamiltonian for the periodically driven central quantum system may still be useful for understanding transport properties. Another strategy to deal with quantum systems, totally different from isolation from the environment, is the method of dissipative or reservoir engineering. In chapter 2 we explain this concept in more detail with a couple of examples. Finally, we give a short introduction to the concept of topology in condensed matter, focusing on the topological edge states of the physical systems considered along this thesis: QH effect, MBSs in a topological superconductor and the dimer chain.

In **chapter 3**, we apply the method of Floquet engineering to find new topological phases for a driven topological superconductor. Moreover, we analyze the dynamics of the topological edge states, so called Floquet Majorana bound states (FMBSs). This work is published in [**P.1**]. In **chapter 4**, published in [**P.2**], we consider a short chain of driven QDs, where the FMBSs loose their topological character but otherwise are more tunable.

In **chapter 5**, we introduce the concept of full-counting statistics (FCS) to obtain information about the central quantum systems via measurements of the transported charge. Importantly, we generalize an interesting way to compute the current cumulants beyond the variance [**P.8**]. Using this formalism, we analyze the statistics of transport through a topological system in **chapter 6**, a chain of dimers implemented in an array of QDs, and relate the results to the existence of topological edge states [**P.4**]. Moreover, we employ again Floquet engineering and show that the Floquet topological phases of a driven dimer chain can also be detected by transport measurements [**P.7**].

Finally, in **chapter 7** we use the method of dissipative engineering in order to propose a setup to generate steady-state entanglement between spins situated in spatially separated QDs [**P.6**]. To mediate a long-range coupling, we propose two alternatives: QH edge states or surface acoustic waves (SAWs).

CHAPTER 2

THEORETICAL BACKGROUND

In this chapter we introduce the most important physical and mathematical concepts for the main contents of this thesis. First we explore different approaches for manipulation of quantum systems; from Floquet engineering for closed or weakly coupled systems to dissipative engineering for open quantum systems. Then, we introduce the concept of topology in condensed matter and apply it to the most relevant physical systems for this thesis.

2.1 Floquet engineering

The time evolution of a quantum-mechanical system is governed by the Schrödinger equation

$$i\partial_t|\psi(t)\rangle = H(t)|\psi(t)\rangle \ , \tag{2.1}$$

where $|\psi(t)\rangle$ is the vector associated to the physical state and $H(t)$ is the Hamiltonian operator. In the equation above we set $\hbar = 1$, as in the rest of this thesis. If the Hamiltonian does not depend on time, it is easy to see that the states $|\psi_\nu(t)\rangle = |\phi_\nu\rangle e^{-iE_\nu t}$, where $\{E_\nu, |\phi_\nu\rangle\}$ are the eigenvalues and eigenvectors of the Hamiltonian,

$$H|\phi_\nu\rangle = E_\nu|\phi_\nu\rangle \ , \tag{2.2}$$

are a complete set of solutions. For a given initial state $|\psi(t_0)\rangle$, the state at any later time reads

$$|\psi(t_0+t)\rangle = \sum_\nu c_\nu|\phi_\nu\rangle e^{-iE_\nu t}, \tag{2.3}$$

where the amplitudes c_ν are $c_\nu = \langle\psi(t_0)|\phi_\nu\rangle$. Then the phase acquired by the state $|\psi_\nu(t)\rangle$ during the time evolution is related to the energy.

If the Hamiltonian is time-dependent, one can formally integrate the Schrödinger equation to express the time evolution of a generic state as

$$|\psi(t_0+t)\rangle = U(t_0+t,t_0)|\psi(t_0)\rangle \ , \tag{2.4}$$

where the time evolution operator is

$$U(t_0+t,t_0) = \mathscr{T}\exp\left\{-i\int_{t_0}^{t_0+t} H(t')dt'\right\} . \tag{2.5}$$

Here $\mathscr{T}$ is the time ordering operator, which complicates enormously the computation.

In the case of a Hamiltonian that depends periodically on time with period T, such that $H(t+T) = H(t)$, Floquet theory can be applied and one can get more physical insight into the behavior of the system [39–41]. This is the reason for the interest in these so called Floquet systems. The time periodicity implies that there exists a complete set of time-dependent states, called Floquet states, with the form

$$|\psi_\nu(t)\rangle = e^{-i\epsilon_\nu t}|\phi_\nu(t)\rangle \ , \tag{2.6}$$

where $|\phi_\nu(t)\rangle$ are time-periodic functions, $|\phi_\nu(t+T)\rangle = |\phi_\nu(t)\rangle$, called Floquet modes and ϵ_ν are the so called quasienergies [40, 41]. The phase acquired by the state as it evolves over one period is then proportional to the quasienergy ($\epsilon_\nu T$). Importantly, they are defined only up to an integer multiple of the frequency $\omega = 2\pi/T$, unlike the energies. By definition, Eq. (2.4), the one-period time evolution operator fulfills

$$U(t_0+T,t_0)|\phi_\nu(t_0)\rangle = e^{-i\epsilon_\nu T}|\phi_\nu(t_0)\rangle \ , \tag{2.7}$$

which is often called Floquet equation and is a way to find the quasienergies and the Floquet modes $|\phi_\nu(t_0)\rangle$ for $t_0 \in (0,T)$. Given an initial state $|\psi(t_0)\rangle$, if we determine the amplitudes $\{c_\nu\}$, given by $c_\nu = \langle\psi(t_0)|\phi_\nu(t_0)\rangle$ (note that these amplitudes are also time-independent), the state at arbitrary time reads

$$|\psi(t_0+t)\rangle = \sum_\nu c_\nu|\phi_\nu(t_0+t)\rangle e^{-i\epsilon_\nu t}, \tag{2.8}$$

which is an equation analogous to Eq. (2.3) for time-periodic systems.

When one faces a time-dependent problem, it is often a good first step to find an appropriate rotation of the reference frame where the dynamics simplifies. In the following, the effect of a rotation of frame is clarified for a Floquet system. A rotation of frame given by the unitary transformation $\mathscr{S}(t)$ modifies the states, $|\tilde{\psi}(t)\rangle = \mathscr{S}^\dagger(t)|\psi(t)\rangle$, and the Hamiltonian,

$$\tilde{H}(t) = \mathscr{S}^\dagger(t)H(t)\mathscr{S}(t) - i\mathscr{S}^\dagger(t)\partial_t\mathscr{S}(t) \ . \tag{2.9}$$

The original Floquet modes transformed in the same way, $|\tilde{\phi}_\nu(t)\rangle = \mathscr{S}^\dagger(t)|\phi_\nu(t)\rangle$, fulfill the periodicity property

$$|\tilde{\phi}_\nu(t+T)\rangle = \mathscr{S}^\dagger(t+T)\mathscr{S}(t)|\tilde{\phi}_\nu(t)\rangle \ , \tag{2.10}$$

i.e., the periodicity of the Floquet modes is modified unless the unitary transformation has the periodicity of the Hamiltonian, in which case $\mathscr{S}^\dagger(t+T)\mathscr{S}(t)=1$. By using the definition of the one-period time evolution operator in the new reference frame, $\tilde{U}(t_0+T,t_0)|\tilde{\psi}_\nu(t_0)\rangle = |\tilde{\psi}_\nu(t_0+T)\rangle$, one can easily derive the analog of the Floquet equation for the transformed Floquet modes,

$$\tilde{U}(t_0+T,t_0)|\tilde{\phi}_\nu(t_0)\rangle = e^{-i\epsilon_\nu T}\mathscr{S}^\dagger(t_0+T)\mathscr{S}(t_0)|\tilde{\phi}_\nu(t_0)\rangle \ . \tag{2.11}$$

As a consequence, the relation between quasienergies ϵ_ν and eigenvalues of $\tilde{U}(t_0+T,t_0)$ depends on $\mathscr{S}(t)$, i.e., on the chosen reference frame, if the unitary transformation $\mathscr{S}(t)$ does not have the periodicity of the Hamiltonian. In chapter 3 we describe a situation where a transformation with a *different* period than the Hamiltonian is useful.

Among the possible transformations with the periodicity of the Hamiltonian, a very special one, $\mathscr{S}_F(t+T)=\mathscr{S}_F(t)$, can be formally constructed such that it leaves the Hamiltonian time-independent, $H_F = \mathscr{S}_F^\dagger(t)H(t)\mathscr{S}_F(t) - i\mathscr{S}_F^\dagger(t)\partial_t\mathscr{S}_F(t)$ [73]. In this special frame, the time evolution operator is trivial $\tilde{U}(t_0+t,t_0)=e^{-iH_Ft}$ and the original time evolution operator reads

$$U(t_0+t,t_0) = \mathscr{S}_F(t_0+t)e^{-iH_Ft}\mathscr{S}_F^\dagger(t_0) \ . \tag{2.12}$$

Moreover, the quasienergies are simply the eigenvalues of the time-independent Hamiltonian H_F, i.e., the quasienergies are the energies detected in the appropriated reference frame where the problem becomes time-independent. Eq. (2.12) is a decomposition of the time evolution into a initial kick operator $\mathscr{S}_F^\dagger(t_0)$, the evolution under the effective Hamiltonian H_F and a final kick operator $\mathscr{S}_F(t_0+t)$.

Importantly, there exists no unique operator that would leave the Hamiltonian time-independent. For example, the operator $\mathscr{S}'_F(t)=\mathscr{S}_F(t)\mathscr{S}_F^\dagger(t_0)$ is associated to the time-independent Hamiltonian $H_F^{t_0}=\mathscr{S}_F(t_0)H_F\mathscr{S}_F^\dagger(t_0)$ and the Eq. (2.12) becomes

$$U(t_0+t,t_0) = \mathscr{S}_F(t_0+t)\mathscr{S}_F^\dagger(t_0)e^{-iH_F^{t_0}t} \ . \tag{2.13}$$

With this decomposition of the time evolution, it is evident that the stroboscopic dynamics, defined as the dynamics for times corresponding to integer periods of the driving, is dominated by the effective Hamiltonian $H_F^{t_0}$ since

$$U(t_0+T,t_0) = e^{-iH_F^{t_0}T} \ . \tag{2.14}$$

In spite of the parametric dependence of this Hamiltonian on the initial time t_0, the spectrum of quasienergies should not depend on it.

The finding of any of these two transformations would yield very useful information. However, the exact transformation can be obtained only in a very restricted set of problems. In general, one needs to apply perturbation theory to obtain a high-frequency expansion (in powers of ω^{-1}) for these effective Hamiltonians. The expansion for the Hamiltonian H_F is called van Vleck expansion [74] and the expansion for $H_F^{t_0}$ is called Floquet-Magnus expansion [75]. For more details on these series and for an expression for the first orders terms see Appendix A.

Now we are in the position to introduce the concept of *Floquet engineering* [74, 76]. Floquet engineering consists in generating strategies to manipulate the quantum systems by time-periodic driving protocols and the knowledge of the corresponding effective time-independent Hamiltonians. By means of the appropriated driving protocol, one can manipulate a quantum system such that its stroboscopic dynamics is governed by an interesting time-independent Hamiltonian. This method has been employed to obtain dynamic localization [33–37], novel topological band structures [42–47] or photon-assisted tunneling in open quantum systems [77–84]. In the context of Floquet engineering one needs to take into account that a time-periodic system with a given time-independent effective Hamiltonian is not the same as the corresponding time-independent system. For instance, the quasienergies are only defined modulo ω, which can have serious consequences for the particular application. In this thesis we explore novel topological phases of matter in a driven topological superconductor in chapter 3 and Floquet Majorana bound states (FMBSs) in short quantum dot (QD) arrays in chapter 4. Finally, in chapter 6 we consider Floquet engineering in an open quantum system.

2.2 Open quantum systems

The dynamics of an isolated or *closed* system, meaning that it does not interchange information with any other system, is coherent and governed by a Schrödinger equation. If the whole universe were considered as a closed system, any quantum-mechanical process could be described by the Schrödinger equation with the corresponding Hamiltonian. However, treating that Hamiltonian is practically impossible. A typical example where incoherent process come into play is a small central system interacting with a macroscopic environment, also known as *open* quantum system. The impossibility to treat the quantum degrees of freedom of the macroscopic object leads to a much more efficient treatment of the problem which implies the appearance of incoherent processes in the reduced dynamics of the small central system. This is what happens in a transport setup where a central system can interchange particles with the environment, which may consist of one or more macroscopic leads. In this case the interaction with the environment builds statistical mixtures of pure states, which are known as mixed states and are described via the density operator. There are various techniques to trace out the leads degrees of freedom under certain conditions with the aim of having simple equations for the dynamical evolution of the reduced density matrix, or the density matrix describing the central system ϱ, defined as the partial trace over the leads (or baths) of the total density matrix $\mathscr{W}$, i.e., $\varrho = \mathrm{tr}_{\mathrm{B}}\mathscr{W}$.

In Appendix B we derive the dynamical evolution for the density matrix of a central system coupled to leads. The starting point is the von Neumann equation,

$$\dot{\mathscr{W}}(t) = -i\left[H_S + H_B + H_I, \mathscr{W}(t)\right] , \tag{2.15}$$

which describes the evolution of the total density matrix in terms of the total Hamiltonian, which consists in a central system part H_S, a Hamiltonian for the leads (or baths) H_B, and

the interaction between them H_I. The goal is a master equation that governs the evolution of the reduced density matrix ϱ. To avoid the long derivation in this introduction, we restrict ourselves to discussing master equations that are local in time and have constant coefficients. As demonstrated in Ref. [85], the most general evolution that preserves the properties of the density matrix is given by a Lindblad form master equation

$$\dot{\varrho} = -i\left[H,\varrho\right] + \sum_{\alpha} \frac{\gamma_\alpha}{2}\left(2L_\alpha \varrho L_\alpha^\dagger - L_\alpha^\dagger L_\alpha \varrho - \varrho L_\alpha^\dagger L_\alpha\right) , \tag{2.16}$$

where H is an effective Hamiltonian, while L_α for $\alpha \in (1, N^2-1)$ are called Lindblad operators. The rates γ_α are non-negative and N is the dimension of the Hilbert space (recall that the dimension of the density matrix is $N \times N$). The operators L_α and H depend on the details of the interaction. To simplify the notation, let us define the Lindblad dissipators,

$$\mathscr{D}(x)\varrho = 2x\varrho x^\dagger - x^\dagger x\varrho - \varrho x^\dagger x , \tag{2.17}$$

and the Liouvillian $\mathscr{L}$,

$$\mathscr{L}\varrho = -i\left[H,\varrho\right] + \sum_{\alpha} \frac{\gamma_\alpha}{2}\mathscr{D}(L_\alpha)\varrho , \tag{2.18}$$

as the total superoperator. In a transport setup with weak coupling and Markovian leads (see Appendix B), every lead will contribute to the total Liouvillian with two types of Linblad dissipators: one transfers electrons to the system and the other takes them away. The parameters γ_α are incoherent tunnel rates.

While quantum information processing (QIP) is usually performed in closed systems, the possibility to couple a QD or a chain of QDs to leads (a source and a drain of electrons) may be useful as well. It not only can be exploited for qubit readout, but also allows one to determine the relevant system parameters. Thanks to the Coulomb repulsion between electrons confined to small system sizes, states with different electron number are energetically well separated, which in general allows one to treat a few-electron problem instead of working in the full Hilbert space. Upon increasing the source-drain voltage bias, an increasing number of levels beocomes relevant such that a current measurement provides the spectrum of the QDs. The dominating feature in the current-voltage profile is provided by the repulsion energy which causes Coulomb blockade [48]. When electron spins and phonons come into play, additional blockade phenomena may influence the current-voltage characteristics. For example, the Pauli exclusion principle may cause a spin blockade in double [86, 87] and triple QDs [58]. Moreover, in suspended QDs, an entering electron may emit a phonon and become trapped until it reabsorbs a phonon, which is known as phonon blockade [88].

In these transport setups, not only the average current provides information but also its fluctuations. Some blockade phenomena are less pronounced in the current, but have a strong impact on the current noise. Most prominently, the strong coupling of an electron in a molecular wire with a vibrational degree of freedom may lead to a switching between conducting and almost isolating configurations and cause Franck-Condon blockade. Then the transport becomes

avalanche-like, which drastically enhances the shot noise [89, 90]. A similar effect occurs in capacitively coupled transport channels, where noise measurements reveal that a mutual channel blockade causes electron bunching [91, 92].

In chapter 5, we develop a scheme for the computation of the full-counting statistics (FCS) of transport described by Markovian master equations with an arbitrary time dependence. Then in chapter 6, we analyze the transport through a simple topological system and propose a transport blockade mechanism based on an interplay of Coulomb repulsion and topology. Under certain conditions, the concept of Floquet engineering is also applicable to open quantum systems, where for example the periodic driving of the central system may be responsible for a suppression or enhancement of the current. In chapter 6, the mentioned blockade is shown to emerge also in a periodically driven system, which could facilitate the experimental setup for its measurement.

2.3 Dissipative engineering

As briefly explained above, the concept of *dissipative engineering* consists in suitably engineering the continuous coupling of the central system to its environment in order to actively utilize dissipation to create and stabilize quantum coherences. In this way, dissipation turns into a driving force behind the emergence of coherent quantum phenomena, instead of being a corrupting mechanism [60]. A tremendous progress has been made towards the implementation of this approach for quantum state preparation [61, 63–66, 70–72, 93–99] with the ultimate goal to achieve quantum computation [62, 67, 68] or quantum simulation [69]. These dissipative methods come with potentially significant advantages since they are unaffected by timing and preparation errors and are inherently robust against weak random perturbations, allowing one e.g. to stabilize entanglement for arbitrary long times.

As enlightening examples, let us consider two different generic dissipative entanglement-generating dynamics for a system of two spin-1/2 fermions described by the density matrix ρ. The first master equation is [94]

$$\dot{\rho} = \alpha\mathscr{D}\left(\mu S_1^+ + \nu S_2^+\right)\rho + \beta\mathscr{D}\left(\nu S_1^- + \mu S_2^-\right)\rho, \tag{2.19}$$

where $S_i^\pm$, $(i = 1,2)$ denote the raising and lowering operators for spin i and $\mathscr{D}(x)\rho$ is a Lindblad dissipator (see Eq. 2.17). For all rates $\alpha, \beta{>}0$, the dissipative evolution given in Eq. (2.19) drives the system into the steady state $|\Psi_{\rm ss}\rangle = \mu|\uparrow\downarrow\rangle - \nu|\downarrow\uparrow\rangle$, which is unique and entangled for all $\mu, \nu{>}0$, $\mu{\neq}\nu$. While the entanglement is largest as $\mu \to \nu$, for $\mu = \nu$ the steady state is no longer unique (as it is the case if one of the rates is zero). When there is more than one steady state, the long-time behavior depends on the initial state and may be strongly affected by small perturbations. For example, this is the case for $\beta = 0$ (that is, without the second Lindblad dissipator) in Eq. (2.19). Still, a pure unique entangled steady state can be recovered by adding a suitable Hamiltonian term [95], e.g., with the master equation

$$\dot{\rho} = -2i\Omega\left[S_1^x + S_2^x, \rho\right] - \Delta\left[S_2^- S_1^+ - S_2^+ S_1^-, \rho\right] + \gamma\mathscr{D}\left(S_1^+ + S_2^+\right)\rho, \tag{2.20}$$

with $S_i^x = \left(S_i^+ + S_i^-\right)/2$. Here, the corresponding steady state reads $|\Psi_{\rm ss}\rangle \propto |\uparrow\uparrow\rangle + i\sqrt{2}\Omega/\Delta|S\rangle$, where $|S\rangle = (|\uparrow\downarrow\rangle - |\downarrow\uparrow\rangle)/\sqrt{2}$ is the maximally entangled singlet state.

In chapter 7, we engineer an environment for two spatially separated spin-1/2 fermions such that their dynamics is approximately governed by the master equations (2.19) and (2.20).

Robustness.—In the context of dissipative engineering, normally the target state is the steady state of the dynamics described by a Liouvillian superoperator $\mathscr{L}$, i.e., the eigenvector with zero eigenvalue $\mathscr{L}\rho = 0$. An important advantage of dissipative state preparation schemes is their robustness, i.e., that the relevant qualitative and quantitative features of the target state are preserved under perturbations $\mathscr{L}_1$ of the dynamics. It is a feature of the contractive dynamics generated by Lindblad-form Liouvillians that the schemes are inherently unaffected by transient, timing, and preparation errors; moreover, perturbations do not affect the steady-state eigenvalue, which remains 0. Standard perturbation theory (cf., e.g., [100, 101]) shows that the changes to the steady state (and to the other eigenvalues) remain small (for a nondefective/nondegenerate $\mathscr{L}$) as long as the strength of the perturbation is small compared to the smallest (in modulus) nonzero eigenvalue of $\mathscr{L}$. This latter number is lower bounded by the "dissipative" or "spectral" gap of $\mathscr{L}$, determined by the eigenvalue of the Liouvillian with the largest real part different from zero, i.e., $\epsilon = -\max\{\mathrm{Re}(\lambda_i)\}$, where λ_i are the nonzero eigenvalues of the Liouvillian.

2.4 Topology in condensed matter: edge states

Condensed matter physics deals with diverse phases of matter, transitions between them, and how their physical properties are affected by factors such as an applied pressure, doping, spin of the particles, and temperature [1]. In the last decades, an additional family of phases of matter, whose interest lies on *independence* on the parameters, has attracted intense attention: topological phases. Topology is a branch of mathematics concerned with properties that are preserved under continuous deformations, i.e., without abrupt changes. The typical example is the equivalence between our breakfast cup and a donut since both possess the same number of holes. Analogously, topological phenomena in condensed matter imply physical properties insensitive to details of the material, which obviously suggests their potential for novel technological applications [102, 103].

The topological aspects have been successfully applied to the well established Bloch-band theory for solids and the distinct topological phases are usually labeled by topological indices. In insulators, the topological protection is related to discrete symmetries and the existence of a bulk gap. It is not possible to have a topological phase transition (TPT), i.e., a transition between phases with distinct topological index, without the bulk gap closing, which necessarily implies an abrupt change, unless the symmetries break. Precisely for this reason, in a physical boundary between two materials with distinct topological phases, the energy gap has to close. This is the naive explanation for the appearance of subgap boundary modes.

In many cases, these edge states of topological origin become perfect conducting channels due

to the bulk-gap topological protection. They also allow for the storage of quantum information in a non-local way making it robust against local perturbations, which paves the way to fault tolerant quantum computation.

The Berry phase [104] is the most important concept in the topological Bloch-band theory. Although originally the Berry phase was introduced in the context of adiabatic evolution of eigenstates under switching of external parameters, we introduce it directly in the context of Bloch-band topology [105, 106]. According to the Bloch's theorem the translational invariance in a material implies that the eigenstates follow $\psi_{\nu,\mathbf{q}}(\mathbf{r}+\mathbf{a}) = e^{i\mathbf{q}\cdot\mathbf{a}}\psi_{\nu,\mathbf{q}}(\mathbf{r})$, where ν is the band index, $\mathbf{a}$ is the lattice vector and $\mathbf{q}$ the crystal momentum. If the momentum $\mathbf{q}$ is forced to perform a closed loop $\mathscr{C}$, the Bloch state will pick up a Berry phase

$$\gamma_\nu = \oint_{\mathscr{C}} d\mathbf{q} \cdot \langle u_\nu(\mathbf{q}) | i\nabla_{\mathbf{q}} | u_\nu(\mathbf{q}) \rangle \ , \tag{2.21}$$

where $|u_\nu(\mathbf{q})\rangle$ is the periodic part of the Bloch function, $u_{\nu,\mathbf{q}}(\mathbf{r}+\mathbf{a}) = u_{\nu,\mathbf{q}}(\mathbf{r})$ with $\psi_{\nu,\mathbf{q}}(r) = e^{i\mathbf{q}\cdot\mathbf{r}}u_{\nu,\mathbf{q}}(\mathbf{r})$, Fourier-transformed into momentum space. If the system is one-dimensional, the only way to realize a closed loop is to sweep the entire Brillouin zone, in which case the Berry phase is called Zak phase [107]. In principle, this phase can assume any value, but in a system with spatial inversion symmetry it is quantized and, thus, restricted to the values 0 and π [105, 108]. In higher dimensions, it is more useful to define the Berry curvature as

$$\Omega_\nu(\mathbf{q}) = \nabla_{\mathbf{q}} \times \langle u_\nu(\mathbf{q}) | i\nabla_{\mathbf{q}} | u_\nu(\mathbf{q}) \rangle \ , \tag{2.22}$$

whose integration on a closed manifold is an important topological index called Chern number, responsible for quantization effects as the integer quantum Hall (QH) effect discussed below.

Thus the Zak phase and the Chern number are topological indices directly related to the Berry phase and the Berry curvature, respectively. But this is not the end of the story. In the last years, more and more types of topological phases have been classified according to new topological indices, whose main property is that they remain invariant as long as a TPT does not occur. For example, some one-dimensional topological systems cannot be fully classified by the Zak phase. Here, the winding number is a more convenient quantity, as is the case for a one-dimensional system with time-reversal, particle-hole and chiral symmetry [108–110]. A general two-band Bloch Hamiltonian of this type can be always written in the form

$$H(k) = h_0 I + h_x \sigma_x + h_y \sigma_y \ , \tag{2.23}$$

with I the 2×2 identity matrix and σ_α the Pauli matrices. As the eigenvectors are

$$|u_\pm\rangle = \frac{1}{\sqrt{2}} \begin{pmatrix} \pm 1 \\ \frac{h_x + i h_y}{\sqrt{h_x^2 + h_y^2}} \end{pmatrix} , \tag{2.24}$$

with eigenvalues $E_\pm = \pm\sqrt{h_x^2 + h_y^2}$, the Zak phase for the lower band reads

$$Z = \frac{1}{2}\int_{-\pi}^{\pi} dk \frac{h_x \partial_k h_y - h_y \partial_k h_x}{h_x^2 + h_y^2} \pmod{2\pi} \ . \tag{2.25}$$

The winding number, defined as

$$W = \frac{1}{2\pi}\int_{-\pi}^{\pi} dk \frac{h_x \partial_k h_y - h_y \partial_k h_x}{h_x^2 + h_y^2} \,, \tag{2.26}$$

can have any integer value which describes the total number of times that the vector (h_x, h_y) travels counterclockwise around the origin, a quantity that actually explains some physical effects since it counts the number of edge states at the boundary between two topological phases. Importantly, a phase transition can only occur where the energy gap closes, $h_x = h_y = 0$. There, the winding number is ill-defined [111].

In the following, we introduce three different systems whose topological aspects, in particular the corresponding edge states, will be important along this thesis. The first one is a two-dimensional QH system with one-dimensional edge states and the other two, Kitaev and Su-Schrieffer-Heeger (SSH) models, are one-dimensional systems with interesting zero-dimensional edge states. Note that we use the word edge for the boundary of the material, irrespective of the dimension.

2.4.1 Quantum Hall Effect

The discovery of the QH effect in 1980 opened a whole new research field in condensed matter physics. In Ref. [22], von Klitzing et al. reported that the Hall conductivity of a two-dimensional electron gas (2DEG) in a strong magnetic field is exactly quantized in units of e^2/h. In a seminal paper Laughlin explained the quantization by reformulating the problem in terms of a pump cycle [115]. Later, Thouless [116] related this quantization to the field of topology. The Hall conductivity is nothing but the Chern number n multiplied by e^2/h, which means that at the boundary of these systems there has to exist a number n of conducting edge states. This implies that, despite that the material is an insulator, it has a conducting edge. In the limit of high magnetic field, the integer n becomes very large, so that the quantization is no longer visible and one recovers the classical Hall effect.

The QH edge states are chiral, which means that the direction of propagation is opposite in the two edges of the material, which avoids backscattering [see Fig. 2.1 (a)]. On top of the fundamental interest in the QH effect, there is growing interest in the development of quantum-optics-like experiments realized with electrons transported via edge states of the QH effect. The reason is that these states provide one-dimensional, chiral and ballistic channels that can transport coherently quantum information [112, 117]. These interesting topologically protected edge states are used in chapter 7 as mediators of long-range coupling between spatially separated electronic spins.

2.4.2 Topological superconductivity: Majorana bound states

The topological band theory for insulators is also applicable to superconductors. In the Bardeen-Cooper-Schrieffer (BCS) theory of superconductivity [118, 119], the Bogoliubov-de Gennes (BdG)

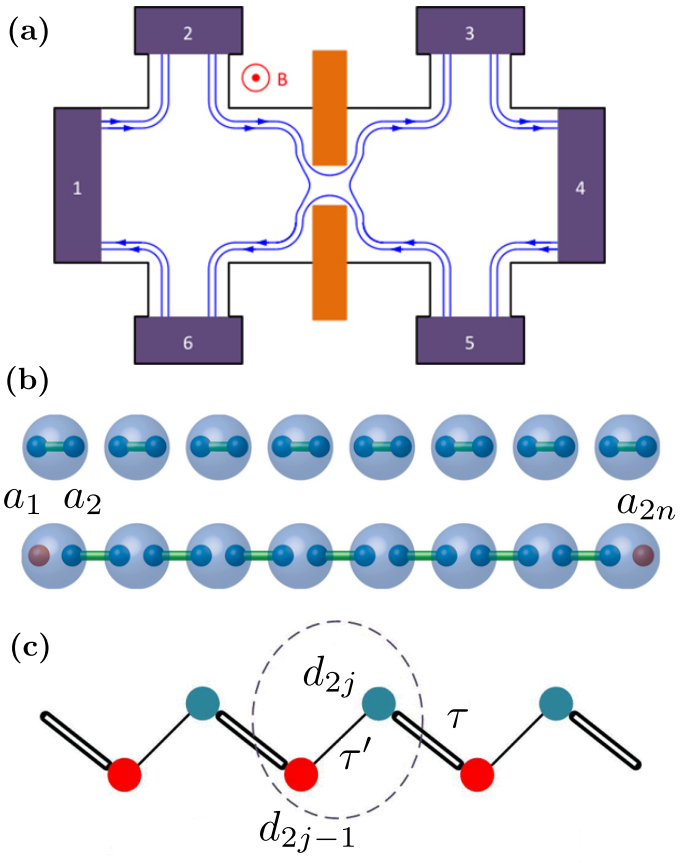

FIGURE 2.1. (a) QH edge states conducting at the boundaries of a 2DEG under the presence of a strong magnetic field. (b) Two phases of the Kitaev chain: Trivial phase (top) has Majorana operators (blue spheres) bound in pairs located on the same site of the physical lattice, represented by translucent spheres. In the topological phase (bottom), the Majorana operators are bound in pairs located in different physical sites. (c) Dimer chain with intra-dimer tunnel coupling τ' and inter-dimer coupling τ. Panel (a) is from Ref. [112], (b) from Ref. [113] and (c) from Ref. [114] (slightly modified).

Hamiltonian [120] allows for computing the spectrum of excitations on top of a mean-field solution. This energy spectrum has a gap related to the energy necessary to break a Cooper pair. Due to the inherent redundancy into the BdG Hamiltonian the excitations γ_E, called quasiparticles, come in pairs with opposite energy, i.e., the BdG Hamiltonian possesses intrinsic particle-hole symmetry in the sense that creating a quasiparticle with energy E is equivalent to removing a quasiparticle with energy $-E$. It means $\gamma_E^\dagger|GS\rangle = \gamma_{-E}|GS\rangle$, where $|GS\rangle$ is the vacuum of excitations fulfilling $\gamma_E|GS\rangle = 0 \ \forall \ E > 0$. The simplest model of a topological superconductor is a BdG Hamiltonian for spinless fermions in one dimension, first introduced by Kitaev [121]. Consider a one-dimensional

lattice with a fermion d_j on each lattice site $j \in (1,n)$. Assume that we are able to induce p-wave superconductivity in such a way that there are interactions between electrons with the same spin in neighboring sites. The corresponding lattice BdG Hamiltonian for this so called one-dimensional Kitaev model is

$$H = \frac{\mu}{2}\sum_{j=1}^{n}\left(2d_j^\dagger d_j - 1\right) - \frac{\tau}{2}\sum_{j=1}^{n-1}\left(d_j^\dagger d_{j+1} + \text{h.c.}\right) - \frac{\Delta}{2}\sum_{j=1}^{n-1}\left(d_j^\dagger d_{j+1}^\dagger + \text{h.c.}\right) , \tag{2.27}$$

where μ is the chemical potential, τ the hopping amplitude and Δ the BCS superconducting pairing. We can now use a discrete Fourier transformation to write the Hamiltonian as

$$H = \sum_{k>0}\Psi_k^\dagger \begin{pmatrix} \mu - \tau\cos k & -i\Delta\sin k \\ i\Delta\sin k & -\mu + \tau\cos k \end{pmatrix}\Psi_k , \tag{2.28}$$

where $\Psi_k^\dagger = (d_k^\dagger, d_{-k})$ and d_k are fermionic operators in Fourier space. To calculate the winding number as in Eq. (2.26), we first rotate the Hamiltonian to the x-y plane, so $h_x = \Delta\sin k$ and $h_y = \mu - \tau\cos k$. The result, given $\tau > 0$, is that the system is topologically trivial, $W = 0$, for $|\mu| > \tau$ and topologically nontrivial otherwise. For $|\mu| < \tau$, the winding number is $W = 1$ if $\Delta > 0$ and $W = -1$ if $\Delta < 0$. To understand the boundary physics of each phase, one can split the fermionic operators into their hermitian constituents

$$a_{2j-1} = d_j + d_j^\dagger; \quad a_{2j} = -i(d_j - d_j^\dagger); \tag{2.29}$$

often called Majorana constituents. In terms of these operators, one can rewrite the Hamiltonian in Eq. (2.27) as

$$H = \frac{\mu}{2}\sum_{j=1}^{n}\left(ia_{2j}a_{2j-1} - 1\right) - \frac{i(\tau+\Delta)}{4}\sum_{j=1}^{n-1}a_{2j}a_{2j+1} - \frac{i(-\tau+\Delta)}{4}\sum_{j=1}^{n-1}a_{2j-1}a_{2j+2} . \tag{2.30}$$

Now it is really enlightening to look into the limiting cases [121]:

- If $\Delta = \tau = 0$ (trivial phase) the Majorana operators on each physical site are coupled, as depicted in the top picture of Fig. 2.1 (b).
- If $\Delta = \tau \neq 0$ and $\mu = 0$ (nontrivial phase) the Majorana operators on neighbor physical sites are coupled, which implies the existence of the isolated Majorana operators a_1 and a_{2n}. This is depicted in the bottom picture of Fig. 2.1 (b). Consequently, the non-local fermionic excitation $(a_1 + ia_{2n})/2$ costs zero energy, therefore the ground state is degenerate with two possible fermionic parities.
- If $\Delta = -\tau \neq 0$ and $\mu = 0$ (nontrivial phase) the isolated Majorana operators are a_2 and a_{2n-1}. Consequently, the non-local fermionic excitation $(a_2 + ia_{2n-1})/2$ costs zero energy and the ground state is also degenerate.

The Majorana basis turns out to be useful not only in these limiting cases but all the way before the phase transition. However, the Majorana boundary excitations are not totally isolated at the edges but they decay exponentially along the length of the chain [121].

The name Majorana excitation comes from the field of particle physics, where the possibility of the existence of a particle that is its own antiparticle was suggested by Ettore Majorana in 1937 [122] and investigated over the years without a definite success [123]. The ground state degeneracy, together with the non-abelian statistics of these operators and the already mentioned non-locality turn the condensed-matter Majorana fermion or Majorana bound state (MBS) into an interesting candidate for fault tolerant topological quantum computation [23–25, 113, 124]. For this reason, the task of detecting these particles in different experimental setups has attracted much attention [24, 125–131].

In the last years, different works have shown how the application of time-dependent electromagnetic fields enriches the properties of these quasiparticles and facilitate their tunability task. For instance, it is possible to generate FMBSs in non-equilibrium systems which also have those interesting properties for quantum computation: non-locality and non-abelian statistics [44, 132]. In chapter 3 we study the new topological phases of a driven Kitaev model and the consequences concerning the number of edge states.

2.4.3 One-dimensional topological insulator: chain of dimers

The probably simplest system exhibiting topological effects is a one-dimensional tight-binding model with alternating tunnel matrix elements or SSH model, originally introduced to describe solitonic effects in polymers [133, 134]. It is characterized by a topological invariant, the winding number, which depends on the ratio between the inter- and intra-dimer coupling and has been measured recently in a dimerized optical lattice [135]. As a consequence of this topological band structure, an edge state emerges at the boundary between two different phases and decays exponentially into the bulk [136].

The Hamiltonian for a chain of dimers is

$$H_{\mathrm{SSH}} = \sum_{j=1}^{n-1} \tau_j d_{j+1}^{\dagger} d_j + \mathrm{h.c.}, \tag{2.31}$$

with the alternating tunnel matrix elements $\tau_j = \tau_0 + (-1)^j \delta\tau$ and the local fermionic annihilation operator d_j. The number of dimers is $n/2$. One can examine this model by keeping τ_0 constant and use $\delta\tau$ as a control parameter. For $\delta\tau < 0$, it describes a chain of weakly coupled dimers which forms two bands with a gap that closes at the transition point $\delta\tau = 0$. When $\delta\tau$ assumes positive values, two edge states emerge.

To find the spectrum of a dimer chain with inter- and intra-dimer couplings τ and τ', respectively, one needs to solve the coupled equations

$$\tau\sigma_+\phi_{j-1} + \tau'\sigma_x\phi_j + \tau\sigma_-\phi_{j+1} = \epsilon_j\phi_j, \tag{2.32}$$

where $\phi_j = \left(d_{2j-1}, d_{2j}\right)^T$ and $j \in (1, n/2)$. For a scheme of a chain of dimers see Fig. 2.1 (c). For

periodic boundary conditions we can work in momentum space and solve

$$\begin{pmatrix} 0 & \tau e^{-ik} + \tau' \\ \tau e^{ik} + \tau' & 0 \end{pmatrix} |u_k\rangle = \epsilon(k)|u_k\rangle. \tag{2.33}$$

The energy spectrum is then

$$\epsilon(k) = \pm\sqrt{\tau^2 + \tau'^2 + 2\tau\tau'\cos k}\,, \tag{2.34}$$

which is gapped except for $\tau = \tau'$ at the points $k = \pm\pi$. The eigenstates are

$$|u_{k,\pm}\rangle = \frac{1}{\sqrt{2}} \begin{pmatrix} e^{-i\theta(k)} \\ \pm 1 \end{pmatrix}, \tag{2.35}$$

where we have defined $\tan\theta(k) = \frac{\tau \sin k}{\tau\cos k + \tau'}$. The winding number is then

$$W = \frac{1}{\pi}\int_{-\pi}^{\pi} \langle u_{k,\pm}|i\partial_k|u_{k,\pm}\rangle = \Theta(\tau - \tau') = \Theta(\delta\tau)\,, \tag{2.36}$$

i.e., the phase is nontrivial when $\delta\tau > 0$. To look for the zero-energy boundary state we consider now a semi-infinite system with a boundary and look for a solution that vanishes at some site such that, e.g., $\phi_0 = 0$. In momentum space this corresponds to the equation

$$\begin{pmatrix} 0 & \tau' \\ \tau e^{ik} + \tau' & 0 \end{pmatrix} |u_{k,\text{edge}}\rangle = 0. \tag{2.37}$$

For $\tau > \tau'$ there exists a nontrivial solution with $k = \pi + i\ln(\tau/\tau')$, which is decaying in position space as $\phi_j \propto \exp(-\kappa j)$ with the exponent $\kappa = \ln(\tau/\tau')$. Thus, for finite arrays, the edge states form a doublet with a level splitting that depends on the ratio τ/τ' and the number of dimers. Close to the phase transition $|\delta\tau| \ll \tau_0$, it becomes $\Delta \approx \tau_0 \exp(-n\delta\tau/\tau_0)$.

The topological properties of these system under the influence of a time-periodic electric field have also been studied [46]. Interestingly, the relation between the intra- and inter-dimer distance comes into play and rich topological phase diagrams are expected.

In chapter 6 we investigate the impact of the edge states on the transport properties when the chain is in contact with an electron source and a drain. Motivated by our results, we propose this setup as a way to measure the topological phase.

CHAPTER 3

FLOQUET ENGINEERING OF TOPOLOGICAL SUPERCONDUCTIVITY

In this chapter, we analyze the topological phases of a driven lattice with spinless fermions with p-wave superconductivity, i.e., the one-dimensional Kitaev model [121] introduced in chapter 2.4. The topological edge states emerging in driven topological superconductors are called Floquet Majorana bound states (FMBSs), because they are the analogous counterpart for Majorana bound states (MBSs) in static systems. The characterization of these excitations allows one to design protocols for their manipulation, which is potentially relevant for braiding operations, essential for fault-tolerant quantum computation [132]. Furthermore, periodic driving opens a new avenue to detect these elusive particles [137, 138].

In the last years, some works have addressed the effect of time-periodic driving fields in topological superconductors. Most of them are restricted to the high-frequency regime. Those addressing lower frequencies are mainly focused on numerical treatments [44, 132, 139, 140]. A more complete analysis was done for periodically kicked systems [141] and step-like periodic pulses [142], including the definition of new topological invariants, while the harmonic driving is treated purely numerically [141]. Our work contains a complete analysis of the monochromatic driving in different frequency regimes where the analytical treatment allows us to characterize different topological phases by means of effective Hamiltonians in rotated reference frames [**P.1**]. Furthermore, we address different ways to drive the Kitaev chain giving rise to a variety of topological phase transitions (TPTs), which could be tested experimentally.

The simple characterization of driven systems for arbitrary frequencies by means of rotations of frame is the most important result of our work. This allows us to obtain the wave function of the MBSs in an easy way and to understand the role of the quasienergies in the TPTs. Moreover, we show that the driving protocols allow one to manipulate the effective interactions between different neighbors, generating effective models that are difficult to implement in time-

independent systems. Apart from this, we establish a connection between the effective interactions generated in the Kitaev model under the effect of driving and the magnetic interactions in the Ising or XY spin models.

In section 3.1 we introduce the model and describe the main tools. In section 3.2 we analyze the case of a driven chemical potential. In this section we present a thorough discussion of the methodology used to determine the TPTs, based on effective Hamiltonians in different frames. In sections 3.3 and 3.4 we consider different driving protocols and discuss the emergence of exotic phases. In particular, we discuss the effective long-range interactions arising under the control of the hopping amplitude. Finally we present our conclusions in section 3.5.

3.1 Model and tools

The system consists of a lattice with $n \gg 1$ sites. Each site j can be either empty or occupied by a spinless fermion represented with the creation(annihilation) operator $d_j^\dagger(d_j)$. It corresponds to the driven version of the one-dimensional Kitaev model [121] (see Eq. 2.27)

$$H(t) = \frac{\mu(t)}{2}\sum_{j=1}^{n}\left(2d_j^\dagger d_j - 1\right) - \frac{\tau(t)}{2}\sum_{j=1}^{n-1}\left(d_j^\dagger d_{j+1} + \text{h.c.}\right) - \frac{\Delta(t)}{2}\sum_{j=1}^{n-1}\left(d_j^\dagger d_{j+1}^\dagger + \text{h.c.}\right), \tag{3.1}$$

where $\mu(t)$ is the chemical potential, $\tau(t)$ the hopping amplitude and $\Delta(t)$ the Bardeen-Cooper-Schrieffer (BCS) superconducting pairing between nearest neighbors in the presence of driving. For periodic boundary conditions, we can use a discrete Fourier transformation to write Eq. (3.1) as $H(t) = \sum_{k>0}\Psi_k^\dagger H_k(t)\Psi_k$, where $\Psi_k^\dagger = (d_k^\dagger, d_{-k})$ is the Nambu basis, d_k are fermionic operators in reciprocal space and

$$H_k(t) = [\mu(t) - \tau(t)\cos k]\sigma_k^z + \Delta(t)\sin k\ \sigma_k^y \tag{3.2}$$

is the bulk Hamiltonian, where σ_k^λ for $\lambda \in \{x, y, z\}$ are the Pauli matrices in Nambu space.

The undriven model, i.e., $\mu(t) = \mu_0$, $\tau(t) = \tau_0$ and $\Delta(t) = \Delta_0$, undergoes a TPT, given that $\tau_0, \Delta_0 > 0$, from a topologically nontrivial phase when $|\mu_0| < \tau_0$ to a topologically trivial behavior for $|\mu_0| > \tau_0$. The Hamiltonian has particle-hole and time-reversal symmetry [143, 144] and therefore the different topological phases can be classified by means of the value of a bulk $\mathbb{Z}$ topological invariant, which corresponds to the winding number, Eq. (2.26). The winding number is $W = 1$ in the nontrivial phase, and $W = 0$ in the trivial one. As explained in chapter 2.4, a Kitaev model in the nontrivial phase with open boundary conditions exhibits MBSs [121].

As explained in chapter 2.4.2, the quasiparticles come in pairs such that a zero-energy excitation will fulfill the Majorana condition $\gamma_0 = \gamma_0^\dagger$. In the driven case, excitations come also in pairs $\gamma_\epsilon(t) = \gamma_{-\epsilon}^\dagger(t)$, where ϵ is the corresponding quasienergy. Due to the periodic structure of the quasienergies (only defined modulo ω), not only $\epsilon = 0$, but also $\epsilon = \pm\frac{\omega}{2}$ excitations fulfill the Majorana condition $\gamma_{0,\frac{\omega}{2}} = \gamma_{0,-\frac{\omega}{2}}^\dagger$ [44]. Therefore a TPT can occur if the quasienergy spectrum closes at those values. Furthermore, both quasienergy gaps can support MBSs and the topological phase is characterized by two $\mathbb{Z}$ topological invariants ($\mathbb{Z}\times\mathbb{Z}$), i.e., two integers. In the following,

we present a method based on reference frame transformations to find the complete topological phase diagram of the driven model, Eq. (3.1). Moreover, our method provides the approximated wave function of the Majorana excitations.

When one applies the method of Floquet engineering to a problem, the choice of the frame of reference is relevant since the expansions to obtain effective Hamiltonians work better in certain frames. In chapter 2.1, we explained the effect of a rotation of the reference frame into the Floquet treatment of a general time-periodic Hamiltonian. In particular, it can be applied to a Bogoliubov-de Gennes (BdG) Hamiltonian in Nambu space. In this case, the transformation into the rotating frame factorizes as $\mathscr{S} = \bigotimes_{k>0} \mathscr{S}_k$. For a given k one can transform the Hamiltonian into the rotating frame as $\tilde{H}_k(t) = \mathscr{S}_k^\dagger H_k(t) \mathscr{S}_k - i \mathscr{S}_k^\dagger \dot{\mathscr{S}}_k(t)$. In Nambu space, Eq. (2.11) implies the eigenvalue problem for the Floquet modes

$$\tilde{U}_k(T,0)|\tilde{\phi}_{\nu,k}(0)\rangle = e^{-i\epsilon_{\nu,k}T} \mathscr{S}_k^\dagger(T) \mathscr{S}_k(0) |\tilde{\phi}_{\nu,k}(0)\rangle \ , \tag{3.3}$$

where $\epsilon_{\nu,k}$ is the ν-th band quasienergy dispersion, $|\tilde{\phi}_\nu(0)\rangle = \bigotimes_{k>0} |\tilde{\phi}_{\nu,k}(0)\rangle$ is the corresponding Floquet mode and $\tilde{U}(T,0) = \bigotimes_{k>0} \tilde{U}_k(T,0)$ is the total one-period time evolution operator. Eq. (3.3) indicates a relation between the eigenvalues of the rotated evolution operator and the quasienergy bands. Therefore, if the convergence condition (see Appendix A),

$$\int_0^T \left\| \tilde{H}_k(t) \right\| dt < \pi \ , \tag{3.4}$$

is fulfilled for every k, it is possible to obtain an effective time-independent Hamiltonian whose eigenvalues are related to the quasienergy bands. According to Eq. (2.14), the Magnus-expanded effective Hamiltonian $\tilde{H}_{\text{eff}} \equiv H_F^0$ is defined as

$$\tilde{U}_k(T,0) = e^{-i\tilde{H}_{\text{eff},k}T} \tag{3.5}$$

and dominates the stroboscopic dynamics.

3.2 Driving the chemical potential

We focus here on the study of the topological properties of the Kitaev model with a monochromatically driven chemical potential. Therefore, we assume $\tau(t) = \tau_0$, $\Delta(t) = \Delta_0$ and

$$\mu(t) = \mu_0 + \frac{\mu_1}{2} \cos \omega t \ , \tag{3.6}$$

where μ_0 is a constant term and $\mu_1/2$ is the amplitude of the driving. As expected, one finds new topological phases that cannot exist in time-independent systems and the existence of two quasienergy gaps will play an important role.

3.2.1 Reference frame choice

Let us first analyze the problem in the laboratory frame, $\tilde{H}(t) = H(t)$. The first Fourier components of the Hamiltonian in Eq. (3.2) read

$$H_{k,0} = \frac{1}{T}\int_0^T dt' H_k(t') = (\mu_0 - \tau_0 \cos k)\sigma_k^z + \Delta_0 \sin k \ \sigma_k^y \ ; \tag{3.7}$$

$$H_{k,\pm 1} = \frac{1}{T}\int_0^T dt' H_k(t') e^{\mp i\omega t} = \frac{\mu_1}{4}\sigma_k^z \ . \tag{3.8}$$

Regardless of the value of the quasimomentum k, the average Hamiltonian over a period $H_{k,0}$ is already a good approximation for the effective Hamiltonian if the frequency is much larger than the bandwidth, $b_w = \mu_0 + \tau_0$, and the driving amplitude, μ_1. However, it will fail to predict the stroboscopic dynamics and the quasienergy spectrum if the frequency is lower or the amplitude is large. It is known that by means of an appropriated rotation of frame the regions of the parameter space that can be explained within an effective Hamiltonian, given by a ω^{-1} expansion, can be enlarged. Here, we work with a whole family of rotating frames given by the transformations

$$\mathcal{S}_k^{\alpha,\dagger}(t) = e^{i\theta^\alpha(t)\sigma_k^z} \ ; \tag{3.9}$$

$$\theta^\alpha(t) = \frac{\alpha\omega}{2}t + \frac{\mu_1}{2\omega}\sin\omega t \ ; \tag{3.10}$$

for $\alpha \in \{0,1,2...\}$. Note that for $\alpha = 0$ this is just the transformation into the interaction picture. The corresponding Hamiltonians in these rotating frames are

$$\tilde{H}_k^\alpha(t) = \left(\mu_0 - \frac{\alpha\omega}{2} - \tau_0\cos k\right)\sigma_k^z - i\Delta_0 \sin k \ e^{2i\theta^\alpha(t)}\sigma_k^+ + i\Delta_0 \sin k \ e^{-2i\theta^\alpha(t)}\sigma_k^- \ . \tag{3.11}$$

Since $\mathcal{S}_k^{\alpha,\dagger}(T)\mathcal{S}_k^\alpha(0) = e^{i\alpha\pi\sigma_k^z}$, Eq. (3.3) becomes

$$\tilde{U}_k^\alpha(T,0)|\tilde{\phi}_{\nu,k}(0)\rangle = e^{-i\epsilon_{\nu,k}T}e^{i\alpha\pi\sigma_k^z}|\tilde{\phi}_{\nu,k}(0)\rangle \ . \tag{3.12}$$

This leads to the eigenvalue equation for the effective bulk Hamiltonian

$$\tilde{H}_{\text{eff},k}^\alpha|\tilde{\phi}_{\nu,k}(0)\rangle = \left(\epsilon_{\nu,k} - \frac{\alpha\omega}{2}\sigma_k^z\right)|\tilde{\phi}_{\nu,k}(0)\rangle \ , \tag{3.13}$$

which implies that the quasienergies and the eigenvalues of the effective Hamiltonian are related by a shift of $\alpha\omega/2$. Due to the periodic structure of the quasienergies, this shift is only relevant if α is odd.

For a given α, the region of convergence of the transformed Hamiltonian $\tilde{H}_k^\alpha(t)$ can be determined from the condition in Eq. (3.4). Let us choose for simplicity $\Delta_0 = \tau_0$ and real parameters $\tau_0, \mu_0 > 0$. As the eigenvalues of this Hamiltonian (Eq. 3.11) do not depend on the amplitude μ_1, the convergence condition is μ_1-independent, while it depends on μ_0, τ_0 and ω in the following way:

$$\mu_0 > \alpha\frac{\omega}{2} \text{ and } \mu_0 - \alpha\frac{\omega}{2} + \tau_0 < \frac{\omega}{2}; \quad \text{or} \quad \mu_0 < \alpha\frac{\omega}{2} \text{ and } \tau_0 + \alpha\frac{\omega}{2} - \mu_0 < \frac{\omega}{2}; \tag{3.14}$$

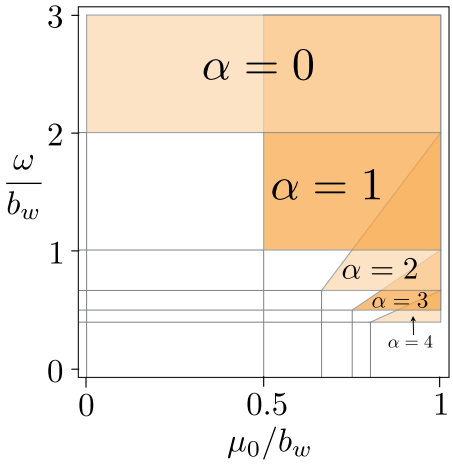

FIGURE 3.1. Regions of convergence of the Magnus expansion of $\tilde{H}_k^\alpha(t)$ for $\alpha \in \{0,1,2,3,4\}$ as a function of μ_0 and ω. In order to obtain a convergent Magnus expansion, the Hamiltonian $\tilde{H}_k^\alpha(t)$ has to fulfill the convergence condition Eq. (3.4) for all the values of k. At high frequency $\omega > 2b_w$, the expansion of $\tilde{H}_k^0(t)$ converges. For $\omega < 2b_w$ the successive $\tilde{H}_k^\alpha(t)$ have convergent expansion for some values of μ_0. We consider a fixed bandwidth $b_w \equiv \mu_0 + \tau_0$.

By fixing the bandwidth, $b_w \equiv \mu_0 + \tau_0$, one can depict the regions of convergence of the Magnus expansion,

$$\frac{\omega}{b_w} > \frac{2}{1+\alpha} \quad \text{and} \quad \frac{\mu_0}{b_w} > \frac{1}{2} + \frac{(\alpha-1)}{4}\frac{\omega}{b_w} \; ; \tag{3.15}$$

for successive $\tilde{H}_k^\alpha(t)$ as a function of μ_0 and ω (see Fig. 3.1). For instance, the expansion of $\tilde{H}_k^0(t)$ converges in the high frequency regime $\omega > 2b_w$. As we lower the frequency, the successive Hamiltonians $\tilde{H}_k^\alpha(t)$ have convergent expansion only for some values of μ_0 as:

$$\alpha = 0: \qquad \omega > 2b_w \text{ and } \mu_0 > 0; \tag{3.16}$$

$$\alpha = 1: \qquad \omega > b_w \text{ and } \mu_0 > \frac{b_w}{2}; \tag{3.17}$$

$$\alpha = 2: \qquad \omega > \frac{2}{3}b_w \text{ and } \mu_0 > \frac{b_w}{2} + \frac{\omega}{4}; \tag{3.18}$$

$$\vdots \qquad \vdots$$

Focussing on a region of the parameter space where one of the transformed Hamiltonians has a convergent Magnus expansion, we can build up an effective Hamiltonian by summing up enough terms of the expansion (see Appendix A). The Fourier components of $\tilde{H}_k^\alpha(t)$ read

$$\tilde{H}_{k,p}^\alpha = \left(\mu_0 - \frac{\alpha\omega}{2} - \tau_0 \cos k\right)\delta_{p,0}\sigma_k^z - i\Delta_0 \sin k \; J_{p-\alpha}\left(\frac{\mu_1}{\omega}\right)\sigma_k^+ + i\Delta_0 \sin k \; J_{-p-\alpha}\left(\frac{\mu_1}{\omega}\right)\sigma_k^- \; , \tag{3.19}$$

where $J_p(x)$ is the pth-order Bessel function of the first kind. The effective Hamiltonian allows for a simple description of the TPTs, as we show in the next section. As explained above, a driven

system can undergo a TPT if the quasienergy spectrum closes at 0 or $\pm\omega/2$, while an effective Hamiltonian can only have closings at zero energy, i.e., when two eigenvalues go to zero. The shift in Eq. (3.13) implies that a Hamiltonian with even α will describe closings of the gap at $\epsilon = 0$ (δ_0) and a Hamiltonian with odd α closings of the gap at $\epsilon = \pm\omega/2$ ($\delta_{\omega/2}$).

By now, we have found regions of the parameter space that can be described with only one effective Hamiltonian $\tilde{H}^{\alpha}_{\text{eff},k}$ for every k (see Fig. 3.1). Beyond that regions, it is sometimes possible to use two effective Hamiltonians, e.g. $\tilde{H}^{\alpha}_{\text{eff},k}$ and $\tilde{H}^{\alpha+1}_{\text{eff},k}$, to get a full convergence of the Magnus expansion in such a way that one of the Hamiltonians reproduces the 0-gap and the other one the $\frac{\omega}{2}$-gap. In the following section we show a couple of examples where this turns out to be useful for the topological classification.

3.2.2 Topological phase diagram

Within the regions of convergence, let us approximate the effective Hamiltonian by the zeroth-order term of the Magnus expansion. Thereby, we can use Eq. (3.19) with $p = 0$ as zeroth-order effective Hamiltonian,

$$\tilde{H}^{\alpha}_{\text{eff},k} = \left(\mu_{\text{eff}} - \tau_0 \cos k\right)\sigma^z_k + \Delta_{\text{eff}} \sin k \; \sigma^y_k \,, \tag{3.20}$$

which describes an effective Kitaev model with $\mu_{\text{eff}} = \mu_0 - \frac{\alpha\omega}{2}$ and $\Delta_{\text{eff}} = \Delta_0 J_{-\alpha}\left(\frac{\mu_1}{\omega}\right)$. We consider real parameters $\Delta_0, \tau_0, \mu_0 > 0$. According to the winding number of this effective Hamiltonian, there is a trivial-nontrivial TPT at $|\mu_{\text{eff}}| = \tau_0$, where the winding number changes from $W_\alpha = 0$ ($|\mu_{\text{eff}}| > \tau_0$) to $W_\alpha \neq 0$ ($|\mu_{\text{eff}}| < \tau_0$). In addition, in the nontrivial region, there are TPTs between different topological phases at critical lines defined by $J_{-\alpha}\left(\frac{\mu_1}{\omega}\right) = 0$. The different topological phases are classified by the winding number $W_\alpha = \text{sgn}\left\{J_{-\alpha}\left(\frac{\mu_1}{\omega}\right)\right\}$. Fig. 3.2 (a) depicts the phase diagram for $\alpha = 0$ and Fig. 3.2 (b) for $\alpha = 1$, for the corresponding regions of validity.

The fact that transformed Hamiltonians with even and odd α describe the 0-gap and the $\omega/2$-gap of the quasienergies, respectively, motives the use of two effective Hamiltonians to classify completely the topological features of the system. Therefore, we use two invariants W_α and $W_{\alpha+1}$, which give a complete topological description encoded in the pair $(W_\alpha, W_{\alpha+1})$. An example of this situation is shown in Fig. 3.2 (c) for $\omega = 1.5 b_w$, in which we extend the phase diagram of Fig. 3.2 (b) to smaller values of μ_0. Fig. 3.1 shows that for $\omega > 2b_w$ the Magnus expansion of $\tilde{H}^0_k(t)$ converges independently of k and μ_0. However, for values of k in a neighborhood of $k = 0$, the Magnus expansion converges even for a lower driving frequency $\omega = 1.5 b_w$. This allows us to extend the phase diagram of Fig. 3.2 (b), because the expansion of $\tilde{H}^1_k(t)$ also converges for values in the neighborhood of $k = \pi$ in the region $0.25 b_w < \mu_0 < 0.5 b_w$ (not shown).

Let us analyze in more detail the origin of each TPT and calculate the critical lines for $\omega = 1.5 b_w$ numerically in order to check the validity of our approximated method. In Fig 3.3 (a) the critical lines corresponding to the 0-gap of quasienergies are shown, while the critical lines of the $\frac{\omega}{2}$-gap are represented in Fig. 3.3 (b). The dark lines indicate the occurrence of TPTs. The combination of both gaps provides the whole topological phase diagram depicted in Fig. 3.3 (c),

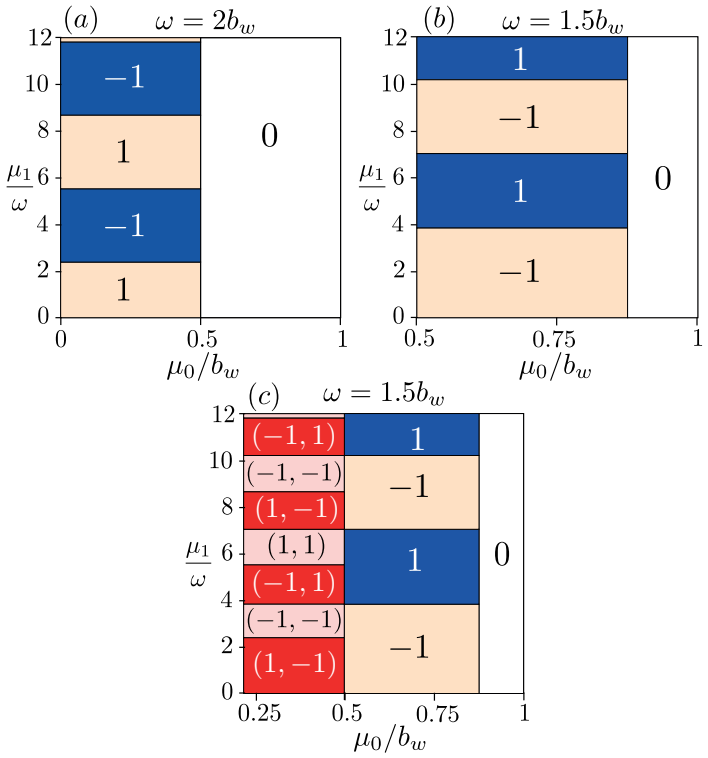

FIGURE 3.2. Phase diagram of the Kitaev model with time-periodic chemical potential. The white regions are topologically trivial ($W = 0$), while the other ones are nontrivial ($W \neq 0$). (a) For $\omega > 2b_w$, $\tilde{H}^0_{\text{eff},k}$ is used to calculate the bulk invariant W_0 for all values of μ_0, because the expansion of $\tilde{H}^0_k(t)$ converges. Transitions between the topological phases $W_0 = +1$ and $W_0 = -1$ occur at zeros of $J_0\left(\frac{\mu_1}{\omega}\right)$. (b) For $\omega = 1.5b_w$, the expansion of $\tilde{H}^1_k(t)$ converges for $\mu_0 > 0.5b_w$. The trivial phase appears for $\mu_0 > 0.875b_w$ and transitions between phases $W_1 = 1$ and $W_1 = -1$ take place at zeros of $J_{-1}\left(\frac{\mu_1}{\omega}\right)$. (c) Extension of the phase diagram shown in (b) to smaller values of μ_0. Besides the phases $W_1 = 0, \pm 1$, we find new topological phases that are described by two topological invariants (W_0, W_1), corresponding to the effective Hamiltonians $\tilde{H}^0_{\text{eff},k}$ and $\tilde{H}^1_{\text{eff},k}$. We consider a fixed bandwidth $b_w \equiv \mu_0 + \tau_0$.

which compares directly to Fig. 3.2 (c). By means of the method developed above, we are able to explain the different phases present in this phase diagram. In the regime $b_w < \omega < 2b_w$ and for any value of k, the convergence condition of Eq. (3.4) for $\tilde{H}^{\alpha=1}_k(t)$ can be reduced to $\mu_0 > 0.5b_w$. On the other hand, the trivial-nontrivial transition occurs at $\mu_0 - \frac{\omega}{2} = \tau_0$, which implies $\mu_0 = \frac{b_w}{2} + \frac{\omega}{4}$. By fixing the frequency, $\omega = 1.5b_w$, we predict TPTs at zeros of the Bessel function $J_{-1}\left(\frac{\mu_1}{\omega}\right)$, which occur at values $\frac{\mu_1}{\omega} \in \{3.8, 7.0, 10.2...\}$, in the regime $0.5b_w < \mu_0 < 0.875b_w$ shown in Fig. 3.3 (b). For smaller values of μ_0, we need to use $\tilde{H}^{\alpha=0}_k(t)$ and $\tilde{H}^{\alpha=1}_k(t)$ and consequently we predict TPTs at zeros of $J_0\left(\frac{\mu_1}{\omega}\right)$ and $J_{-1}\left(\frac{\mu_1}{\omega}\right)$ as in Fig. 3.3 (c).

We show also in Fig. 3.4 the same calculation for $\omega = 0.9b_w$, in order to see that for large

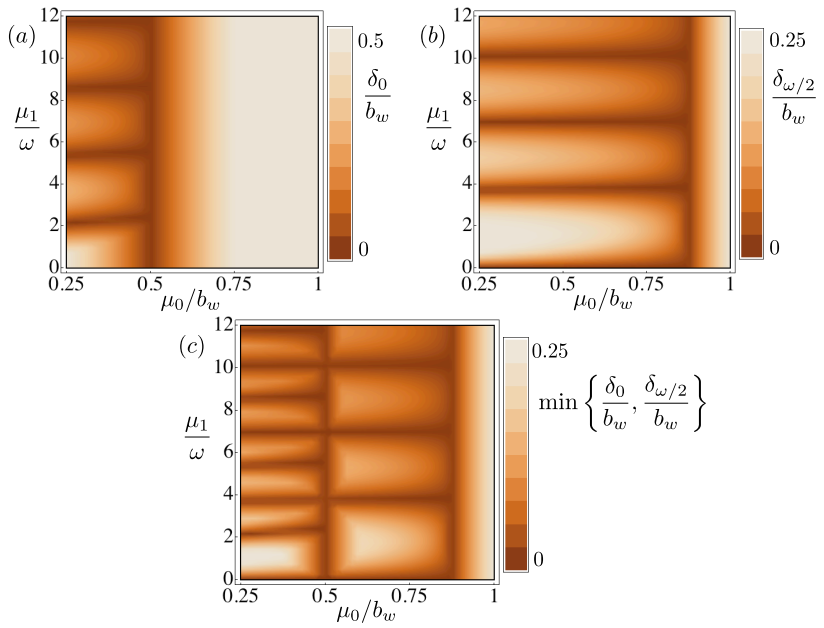

FIGURE 3.3. Critical lines for a Kitaev model with driven chemical potential for $\omega = 1.5b_w$. The dark lines show the closings of the: (a) 0−gap (δ_0), (b) $\frac{\omega}{2}$-gap ($\delta_{\omega/2}$), and (c) both gaps. The full topological phase diagram is given by (c), which agrees very well with the analytical result in Fig. 3.2 (c). We consider a fixed bandwidth $b_w \equiv \mu_0 + \tau_0$.

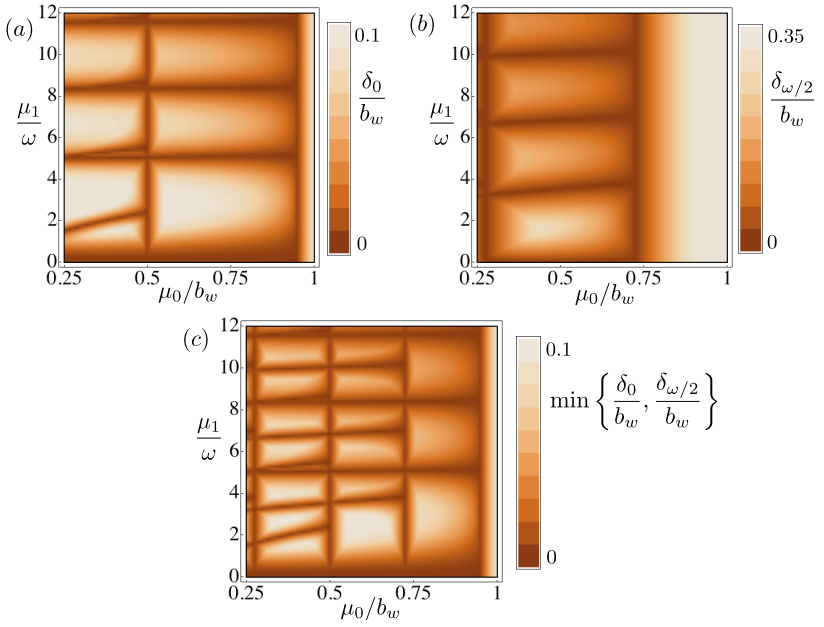

FIGURE 3.4. Critical lines for a Kitaev model with driven chemical potential for $\omega = 0.9b_w$. The dark lines show the closings of the: (a) 0−gap (δ_0), (b) $\frac{\omega}{2}$-gap ($\delta_{\omega/2}$), and (c) both gaps. We consider a fixed bandwidth $b_w \equiv \mu_0 + \tau_0$.

values of μ_0 the analytical approach is useful. For $\frac{2}{3}b_w < \omega < b_w$, the Magnus expansion of $\tilde{H}_k^{\alpha=2}(t)$ converges if $\mu_0 > \frac{b_w}{2} + \frac{\omega}{4}$. For $\omega = 0.9b_w$, this value is $\mu_0 > 0.725b_w$. On the other hand, the trivial-nontrivial transition occurs at $\mu_0 - \omega = \tau_0$. This means $\mu_0 = \frac{b_w}{2} + \frac{\omega}{2} = 0.95b_w$. Then, for values $0.725b_w < \mu_0 < 0.95b_w$, the phase diagram shows TPTs at zeros of $J_2\left(\frac{\mu_1}{\omega}\right)$, which appear at values $\frac{\mu_1}{\omega} \in \{5.1, 8.4, 11.6, ...\}$, as it is shown in Fig. 3.4 (c). For smaller values of μ_0, we predict TPTs at zeros of $J_2\left(\frac{\mu_1}{\omega}\right)$ and $J_1\left(\frac{\mu_1}{\omega}\right)$. However, for even smaller values of μ_0, our analytical approach is not valid anymore and the phase diagram is more complex.

3.2.3 Majorana bound states

The bulk-boundary correspondence involves the existence of end states localized at the boundary between different bulk topologies. In this section we find the time evolution of the MBS at the boundary between a nontrivial topological phase and the vacuum, topologically trivial. Let us assume that one of the transformed Hamiltonians has a convergent expansion for every k in a particular region of the parameter space, as it is depicted in Fig. 3.1. In the case of open boundary conditions, we can use the Majorana constituents $a_{2j-1} = d_j + d_j^\dagger$ and $a_{2j} = -i\left(d_j - d_j^\dagger\right)$ as defined in Ref. [121] to write the zeroth-order effective Hamiltonian in Eq. (3.20) in real space as follows (see Eq. 2.30)

$$\tilde{H}^{\alpha}_{\text{eff}} = \frac{\mu_{\text{eff}}}{2}\sum_{j=1}^{n}\left(ia_{2j}a_{2j-1} - 1\right) - \frac{i\left(\tau_0 + \Delta_{\text{eff}}\right)}{4}\sum_{j=1}^{n-1} a_{2j}a_{2j+1} - \frac{i\left(-\tau_0 + \Delta_{\text{eff}}\right)}{4}\sum_{j=1}^{n-1} a_{2j-1}a_{2j+2}\,. \tag{3.21}$$

In the limiting case $|\mu_{\text{eff}}| \gg |\tau_0 \pm \Delta_{\text{eff}}|$ there are no edge states. In the case $|\mu_{\text{eff}}| \ll |\tau_0 - \Delta_{\text{eff}}|$ and $\Delta_{\text{eff}} \simeq -\tau_0$ the third term dominates and the zero-energy excitations a_2 and a_{2n-1} with a bulk invariant $W_\alpha = -1$ do not appear in the Hamiltonian, but they define the nonlocal fermion $\tilde{f} = \frac{1}{2}(a_2 + ia_{2n-1})$, which is topologically protected [25, 121]. The approximate time evolution of the left end state in the laboratory frame reads

$$\tilde{\gamma}(t) \approx -i\left(d_1 e^{-i\theta^\alpha(t)} - d_1^\dagger e^{i\theta^\alpha(t)}\right)\,. \tag{3.22}$$

In the case where $\mu_{\text{eff}} \ll |\tau_0 + \Delta_{\text{eff}}|$ and $\Delta_{\text{eff}} \simeq \tau_0$, the second term of Eq. (3.21) dominates and the Majorana operators a_1 and a_{2n} do not appear in the Hamiltonian [121]. Similarly to the previous case they are combined into a nonlocal fermion $f = \frac{1}{2}(a_1 + ia_{2n})$. In this regime the system possesses the bulk invariant $W_\alpha = 1$ and the time evolution of the mode localized at the first site reads

$$\gamma(t) \approx d_1 e^{-i\theta^\alpha(t)} + d_1^\dagger e^{i\theta^\alpha(t)}\,. \tag{3.23}$$

Interestingly, at discrete times $t = mT$, the edge states in Eqs. (3.22) and (3.23) are given by $\tilde{\gamma}(mT) \approx -(-1)^{m\alpha} i(d_1 - d_1^\dagger)$ and $\gamma(mT) \approx (-1)^{m\alpha}(d_1 + d_1^\dagger)$, respectively.

For a finite chain with n sites, a numerical calculation allows to obtain the Floquet modes, in particular the edge Floquet modes by focussing on the states at quasienergy 0 or $\pm\omega/2$. In general

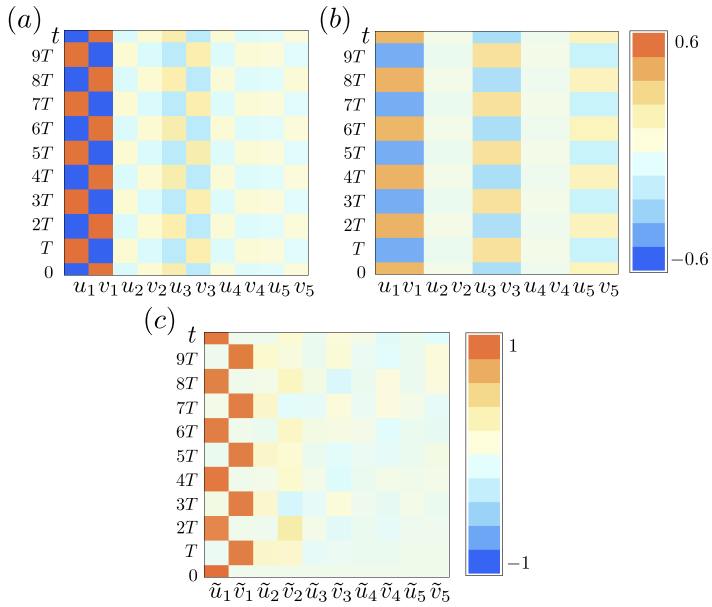

FIGURE 3.5. (a,b) Temporal stroboscopic evolution of the stationary left end state for a finite chain with $N = 60$ sites. The color indicates the value of coefficients u_j and v_j in Eq. (3.24) for the first 5 sites. For a frequency $\omega = 1.5b_w$, we have performed numerical calculations in the case of a driven chemical potential $\mu(t) = \mu_0 + \frac{\mu_1}{2}\cos\omega t$ with $\mu_0 = 0.75b_w$. (a) Depicts the evolution for $\frac{\mu_1}{\omega} = 1$, being $J_{-1}\left(\frac{\mu_1}{\omega}\right) < 0$, and (b) for $\frac{\mu_1}{\omega} = 4.5$, when $J_{-1}\left(\frac{\mu_1}{\omega}\right) > 0$. The stroboscopic dynamic agrees with the predicted one. (c) Shows the evolution of coefficients $\tilde{u}_j$ and $\tilde{v}_j$ (Eq. 3.26) in case $\mu_0 = 0.3b_w$ and $\frac{\mu_1}{\omega} = 1$ imposing the initial condition $\Gamma(0) = d_1$ at $t = 0$. The predicted double period electron-hole oscillations are observed. We consider a fixed bandwidth $b_w \equiv \mu_0 + \tau_0$.

they read

$$\mathbf{\Psi}(t) = \sum_{j=1}^{n} \left[u_j(t) d_j + v_j(t) d_j^\dagger \right] . \tag{3.24}$$

In order to compare our analytical results with numerical calculations, we consider the Eqs. (3.22) and (3.23) for $\alpha = 1$. For instance we perform the calculation for the parameters $\omega = 1.5b_w$ and $\mu_0 = 0.75b_w$, while the bandwidth is fixed $b_w \equiv \mu_0 + \tau_0$, in a chain with $n = 60$ sites. We numerically calculate the coefficients $u_j(t)$ and $v_j(t)$ for a state with quasienergy $\epsilon = \pm\omega/2$. In order to verify that Eq. (3.22) gives the correct stroboscopic dynamics for $\tilde{\gamma}(mT)$, we plot the imaginary part of the coefficients $u_j(t)$ and $v_j(t)$ in Fig. 3.5 (a). One can see that at discrete times $t = mT$ they are approximately in agreement with our analytical results. In addition, Fig. 3.5 (b) depicts the real part of $u_j(t)$ and $v_j(t)$ at discrete times and shows the qualitative agreement with the stroboscopic evolution $\gamma(nT)$ obtained from Eq. (3.23). The states spread along the vicinity of the end, but the weight of the states along the chain decreases exponentially.

In a case with end states in the gaps $\epsilon = 0$ and $\epsilon = \omega/2$ simultaneously we require the use of the effective Hamiltonians $\tilde{H}^{\alpha}_{\text{eff},k}$ and $\tilde{H}^{\alpha+1}_{\text{eff},k}$. For instance, in the phase with the invariant

$(W_0, W_1) = (1, -1)$, there are two MBSs, one in each gap

$$\begin{aligned} \gamma_{\epsilon=0}(t) &\approx d_1 e^{-i\theta^0(t)} + d_1^\dagger e^{i\theta^0(t)} \,, \\ \gamma_{\epsilon=\frac{\omega}{2}}(t) &\approx -i\left(d_1 e^{-i\theta^1(t)} - d_1^\dagger e^{i\theta^1(t)}\right) \,, \end{aligned} \tag{3.25}$$

for parameters $\omega = 1.5 b_w$, $\mu_0 = 0.3 b_w$ and $\mu_1/\omega = 1$. The fact that two non-degenerate (in quasienergy) end states are present in the system generates interferences characteristic of driven topological systems [44, 45]. In order to see the interference of states in both gaps we are interested in the study of the time evolution of the system for a given initial condition. According to the approximated MBSs, if the initial excitation is $\Gamma(0) = d_1$ it can be written as $\Gamma(0) \approx \left[\gamma_{\epsilon=0}(0) + i\gamma_{\epsilon=\frac{\omega}{2}}(0)\right]/2$. Therefore, the evolved excitation is known to be $\Gamma(t) \approx \left[\gamma_{\epsilon=0}(t) + i\gamma_{\epsilon=\frac{\omega}{2}}(t)\right]/2$ at all times. At discrete times $t = mT$ the system exhibits a doubly periodic stroboscopic dynamics $\Gamma(mT) \approx \frac{d_1}{2}[1 + (-1)^m] + \frac{d_1^\dagger}{2}[1 - (-1)^m]$. The numerically obtained evolution of the excitation after an imposed initial condition can be written as

$$\mathbf{\Gamma}(t) = \sum_{j=1}^{N} [\tilde{u}_j(t) d_j + \tilde{v}_j(t) d_j^\dagger] \,. \tag{3.26}$$

We show the predicted doubly periodic oscillations in Fig. 3.5 (c), where we plot the real part of the numerically obtained coefficients $\tilde{u}_j(t)$ and $\tilde{v}_j(t)$ of $\Gamma(t)$ in Eq. (3.26) at discrete times, for the initial condition $\Gamma(0) = d_1$. These oscillations are due to the interference of states in both gaps.

3.3 Driving the hopping and BCS pairing

In this section we apply the findings of last section to study the Kitaev model considering a different driving protocol, which introduces different topological phases with more end states. We consider a Kitaev chain of spinless fermions d_j given in Eq. (3.1) with a constant chemical potential μ_0 and time-periodic hopping and BCS pairing such that

$$\Delta(t) \equiv \tau(t) = \tau_0 + \frac{\tau_1}{2} \cos \omega t \,. \tag{3.27}$$

Using the equivalence of Kitaev and Ising model and a duality transformation, the resolution of the problem is straightforward (see Appendix C).

The phase diagrams for the present configuration are like the ones found in the previous section (see Fig. 3.2), but with a different value of the topological invariants. The phase diagram in the high-frequency regime is shown in Fig. 3.6 (a). The bulk invariant can be tuned from trivial ($W_0 = 0$) to nontrivial ($W_0 = 2$), depending on strength of the driving, while in the case of a driven chemical potential the trivial region remains trivial at high frequency independently of the strength of the driving.

In the case $\tau_0 > \mu_0$, the chain supports end states of the form given in Eq. (3.23), while no end states are present if $\tau_0 < \mu_0$ and $J_0\left(\frac{\tau_1}{\omega}\right) > 0$. To study the existence of end states in the new

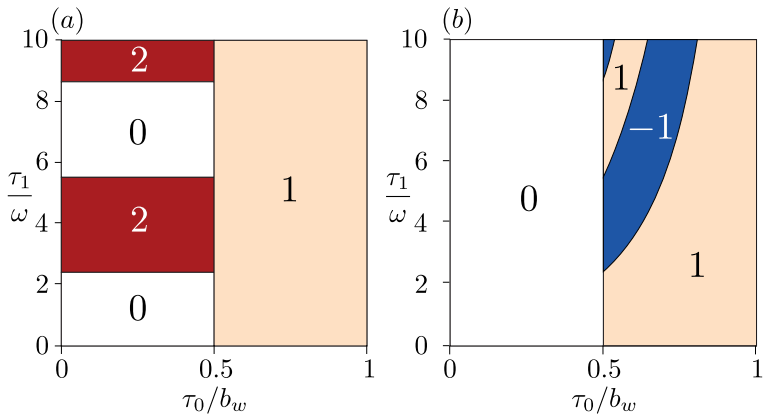

FIGURE 3.6. Phase diagram for $\omega > 2b_w$ in the case of $\mu(t) = \mu_0$, (a) $\Delta(t) = \tau(t) = \tau_0 + \frac{\tau_1}{2}\cos\omega t$, (b) $\Delta(t) = \tau_0$ and $\tau(t) = \tau_0 + \frac{\tau_1}{2}\cos\omega t$. The white region is topologically trivial ($W = 0$), light-orange ($W = 1$) and blue ($W = -1$) are nontrivial phases with one pair of end states and the brown region ($W = 2$) is a nontrivial phase with two pairs of end states. We consider a fixed bandwidth $b_w \equiv \mu_0 + \tau_0$.

phase ($\tau_0 < \mu_0$ and $J_0\left(\frac{\tau_1}{\omega}\right) < 0$), we write the second-neighbors interaction term in Eq. (C.14) in terms of Majorana constituents [121] $a_{2j-1} = d_j + d_j^\dagger$ and $a_{2j} = -i\left(d_j - d_j^\dagger\right)$ as $H \propto i\sum_j a_{2j-2}a_{2j+1}$. Therefore, if the chain is semi-infinite the Majorana operators a_1 and a_3 will not appear in the Hamiltonian, therefore holding two MBSs in the same edge:

$$\gamma_a(t) \simeq d_1 e^{-i\theta^0(t)} + d_1^\dagger e^{i\theta^0(t)}\,, \tag{3.28}$$

$$\gamma_b(t) \simeq d_3 e^{-i\theta^0(t)} + d_3^\dagger e^{i\theta^0(t)}\,. \tag{3.29}$$

To sum up, we have found an effective Kitaev model with second-neighbors hopping and BCS pairing and, consequently, a topological phase hosting two MBSs in the same edge.

3.4 Driving the hopping

Finally, and for completeness, we are interested in the consequences of a driving just on the hopping term of the Kitaev model Eq. (3.1). We consider a constant chemical potential μ_0, BCS pairing Δ_0, and a monochromatic driving of the hopping strength

$$\tau(t) = \tau_0 + \frac{\tau_1}{2}\cos\omega t\,. \tag{3.30}$$

We obtain a solution in the high-frequency limit by means of a transformation into the interaction picture

$$\mathscr{S}_k = e^{i\frac{\tau_1}{2\omega}\sin\omega t\cos k\sigma_k^z}\,. \tag{3.31}$$

The high-frequency effective Hamiltonian is

$$\tilde{H}_{\text{eff},k} = (\mu_0 - \tau_0\cos k)\sigma_k^z + \Delta_0\sin k\; J_0\left(\frac{\tau_1}{\omega}\cos k\right)\sigma_k^y\,. \tag{3.32}$$

The high-frequency phase diagram for $\Delta_0 = \tau_0$ is shown in Fig. 3.6 (b). The transition between trivial and nontrivial phases takes place at $\mu_0 = \tau_0$. More gap closings are found when $J_0\left(\frac{\tau_1}{\omega}\cos k\right) = 0$ and $\mu_0 - \tau_0 \cos k = 0$. This implies $J_0\left(\frac{\tau_1}{\omega}\frac{\mu_0}{\tau_0}\right) = 0$, as long as $\mu_0 < \tau_0$.

Performing the inverse Fourier transformation to the last term in Eq. (3.32) in order to obtain the real space representation is not straightforward due to the k-dependence in the argument of the Bessel function. To simplify, we can use the expansion of the Bessel function in power expansion of its argument

$$J_0(x) = \sum_{m=0}^{\infty} \frac{(-1)^m}{m!^2}\left(\frac{x}{2}\right)^{2m} \tag{3.33}$$

and the expansion

$$(\cos k)^{2m} = \left(\frac{e^{ik} + e^{-ik}}{2}\right)^{2m} = \sum_{r=0}^{2m} \frac{1}{2^{2m}} \binom{2m}{r} e^{2i(m-r)k} \ , \tag{3.34}$$

where the binomial theorem was used, to get

$$J_0\left(\frac{\tau_1}{\omega}\cos k\right) = \sum_{m=0}^{\infty}\sum_{r=0}^{2m} \frac{(-1)^m}{m!^2}\left(\frac{\tau_1}{4\omega}\right)^{2m} \binom{2m}{r} e^{2i(m-r)k} \ . \tag{3.35}$$

By defining the coefficients

$$C_{m,r} = \frac{(-1)^m}{2(m!)^2}\left(\frac{\tau_1}{4\omega}\right)^{2m} \binom{2m}{r} \ . \tag{3.36}$$

this is simplified to

$$J_0\left(\frac{\tau_1}{\omega}\cos k\right) = \sum_{m=0}^{\infty}\sum_{r=0}^{2m} 2C_{m,r} e^{2i(m-r)k} \tag{3.37}$$

and the effective Hamiltonian in Eq. (3.32) (after simple algebraic manipulations) can be written as

$$\tilde{H}_{\text{eff},k} = (\mu_0 - \tau_0 \cos k)\sigma_k^z + \Delta_0 \sum_{l=1,3\ldots} g_l(\tau_1/\omega)\sin kl \ \sigma_k^y \ , \tag{3.38}$$

where we have defined the function $g_l(\tau_1/\omega)$ as

$$g_l(\tau_1/\omega) = 2\sum_{m=0}^{\infty}\left[C_{m,m-\frac{l-1}{2}} - C_{m,m-\frac{l+1}{2}}\right] \ . \tag{3.39}$$

Now it is trivial to compute the Hamiltonian in real space, which reads

$$\tilde{H}_{\text{eff}} = \frac{\mu_0}{2}\sum_{j=1}^{n}\left(2d_j^\dagger d_j - 1\right) - \frac{\tau_0}{2}\sum_{j=1}^{n-1}\left(d_j^\dagger d_{j+1} + h.c.\right) - \frac{\Delta_0}{2}\sum_{j=1}^{n-1}\sum_{l=1,3\ldots} g_l(\tau_1)\left(d_j^\dagger d_{j+l}^\dagger + h.c.\right) \ , \tag{3.40}$$

Despite its apparent simplicity, the BdG Hamiltonian Eq. (3.32) encloses a rich physical meaning. The second term generates new features of the BCS pairing, which arise from effective long-range hopping in real space.

We show the function $g_l(\tau_1)$ in Fig. 3.7. As expected, for small τ_1 the first-neighbors interaction is larger. However, as the amplitude of the driving increases the next-neighbors interactions become important. Since the sign between the first-neighbors and third-neighbors interaction is opposite (compare Fig. 3.7), the winding number changes sign as it was shown in Fig. 3.6 (b).

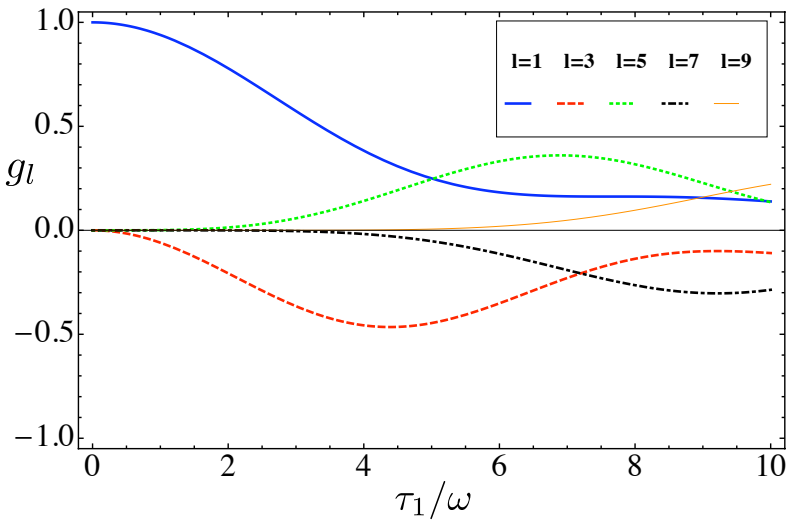

FIGURE 3.7. BCS superconducting pairing strength g_l as a function of τ_1/ω for neighbors $l = 1,3,5,7,9$. Note that the sign of the interaction is $(-1)^{\frac{l-1}{2}}$.

3.5 Conclusions

We have discussed the non-equilibrium TPTs in the Kitaev model with three different driving protocols. In all cases, we focus on the effect of monochromatic control of the parameters. By means of rotations of frame, we get a completely analytical description of the topological phase diagram in a wide range of frequencies for some values of the parameters. Moreover, we are able to provide an approximated wave function for the MBSs. The advantage of our analytical approach is that it allows to easily predict the TPTs at any frequency regime i.e., not only in the high frequency regime but also at intermediate and low frequencies. Our approach allows the comparison with future experiments performed into a full range of frequency regimes of the external driving as far as we restrict ourselves to the given convergence regions.

The Kitaev chain is a simple model that considers spinless fermions. A physical realization of this model is a one-dimensional nanowire with Rashba spin-orbit interaction, Zeeman splitting and proximity induced s-wave superconductivity [126]. In this realization, the periodic variation of the chemical potential in the wire is possible by means of an alternating gate voltage applied to the substrate, as suggested in [139]. Another proposed realization of the Kitaev chain consists in using semiconductor quantum dots (QDs) coupled to superconducting grains [145]. In this setup the access to the other parameters is more suitable because the relations between the experimental and effective parameters is simpler [146].

The equivalence between Kitaev model and Ising model allows to use a simple duality transformation to the resolution of a Kitaev chain whose tunneling and BCS parameters are varied in time harmonically. In this case, new features are found, like the appearance of two

MBSs at high frequency. Finally, by only driving the hopping, very interesting effective models with long-range superconductivity arise.

Our analysis addressing three different ways of driving with harmonic time-dependent potentials gives a full picture of the consequences of the topological phases at arbitrary frequencies. It allows to design the most efficient way to search signatures of FMBSs by appropriated drive of the system. For a brief explanation of the equivalence of these properties in the spin chain basis see Appendix C, where we emphasize the novelties detected.

CHAPTER 4

FLOQUET MAJORANA BOUND STATES IN SUPERCONDUCTING QUANTUM DOTS

In every system with particle-hole symmetry, the quasiparticle excitations come in pairs $\gamma_{-E}^{\dagger} = \gamma_E$, therefore they fulfill the Majorana condition as long as the energy can be tuned to zero. One of the simplest and most tunable systems with particle-hole symmetry is a double quantum dot (QD) connected via a common superconducting lead. It is well known that the proximity effect induces Cooper pairs correlations across the QDs effectively generating superconductivity [147–149]. This system was proposed in Ref. [150] for the obtention of the so called poor man's Majorana bound states (MBSs). Later the same idea was extended to a triple QD [151] and to a driven double QD [152]. The advantage of generating and detecting MBSs in configurations of a few QDs connected to s-wave superconductors is their great tunability. Proposals in nano-wires [24, 125, 126] or long QD chains [121, 145, 146], however, imply topological protection for the MBSs.

The work in this chapter is another example of Floquet engineering. We consider two different configurations of QDs in proximity to superconducting leads such that Cooper pair correlations are induced between neighboring QDs as long as the coherence length is larger than the distance between them. We include periodically driven metallic gates and search for the conditions for appearance of Floquet Majorana bound states (FMBSs) [**P.2**].

The chapter is organized as follows: In section 4.1 we present the model, in section 4.2 we discuss the generation of FMBSs in a double and a triple superconducting QD and in section 4.3 we present our conclusions.

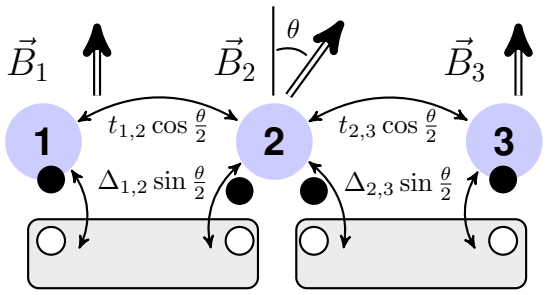

FIGURE 4.1. Scheme of the three QDs coupled via superconductors. The existence of Cooper pairs generates correlations of the type $d_{i,\sigma}d_{i+1,\bar{\sigma}}$ in the effective Hamiltonian for the QDs. Three different magnetic fields are applied to the QDs, where the middle one is rotated by an angle θ with respect to the others. This angle controls the ratio $\Delta_{i,i+1}/t_{i,i+1}$.

4.1 Undriven system

Systems of QDs coupled to s-wave superconductors have been a subject of study [148, 149, 153] because the proximity effect induces Cooper pair correlations that can be easily detected due to the low number of degrees of freedom in the QDs. In a system where neighboring QDs are coupled via superconducting leads as in Fig. 4.1, in the limit of a large superconducting gap the leads can be traced out and one can get the effective Hamiltonian for the QDs [154, 155]

$$H=\sum_{i,\sigma}\mu_{i,\sigma}d^{\dagger}_{i,\sigma}d_{i,\sigma}+\sum_{i,\sigma}\left(t_{i,i+1}d^{\dagger}_{i,\sigma}d_{i+1,\sigma}+\Delta_{i,i+1}d_{i,\sigma}d_{i+1,\bar{\sigma}}+\text{h.c.}\right)\,, \tag{4.1}$$

which contains effective superconductivity between neighboring QDs. The fermionic operator $d^{\dagger}_{i,\sigma}$ creates an electron with spin σ in the i-th QD. The symbol $\bar{\sigma}$ denotes the opposite spin to σ, which can be $\sigma=\uparrow,\downarrow$. μ_i is the onsite energy in the i-th QD, the parameter $t_{i,i+1}$ is the effective hopping amplitude between the i-th QD and the $(i+1)$-th QD through the superconductor by virtual occupation of the above gap excitations and $\Delta_{i,i+1}$ is the effective Bardeen-Cooper-Schrieffer (BCS) superconducting pairing due to the superconductor connecting the i-th QD and the $(i+1)$-th QD. If a large magnetic field is applied to the QDs only one spin comes into play. The magnetic fields $\vec{B}_i$ in the different QDs have to be non-collinear in order to have s-wave type Cooper pair correlations [150]. In this configuration it is more natural to work in the basis of the quantization axes given by the magnetic field in each QD. According to Fig. 4.1, we have to perform the rotation

$$d_{2,\sigma}\rightarrow\cos\frac{\theta}{2}d_{2,\sigma}+\sigma\sin\frac{\theta}{2}d_{2,\bar{\sigma}}\,, \tag{4.2}$$

as the magnetic field in the central QD forms an angle θ with the magnetic fields in the left and right QDs. The low-energy physics is then described by the simpler Hamiltonian

$$H=\sum_{i}\mu_i d^{\dagger}_i d_i+\sum_{i}\left\{t'_{i,i+1}d^{\dagger}_i d_{i+1}+\Delta'_{i,i+1}d_i d_{i+1}+\text{h.c.}\right\}\,, \tag{4.3}$$

where we have defined: $d_i \equiv d_{i,\downarrow}$, $\mu_i \equiv \mu_{i,\downarrow}$, $t'_{i,i+1} \equiv t_{i,i+1}\cos\theta/2$ and $\Delta'_{i,i+1} \equiv \Delta_{i,i+1}\sin\theta/2$. The hopping amplitude and the superconducting pairing are renormalized and their renormalization depends on θ. This dependence introduces a simple way to tune the coupling parameters of the system externally [150]. The latter Hamiltonian is written in Nambu basis, $\Psi = \left(d_1, d_1^\dagger, \ldots, \ldots, d_n, d_n^\dagger\right)^T$, as

$$H = \frac{1}{2}\Psi^\dagger h \Psi + \frac{1}{2}\sum_i \mu_i \ . \tag{4.4}$$

Then the eigensystem of the matrix h, $h\mathbf{v}_i = \lambda_i \mathbf{v}_i$, determines the quasiparticles, given by $\gamma_i = \mathbf{v}_i \cdot \Psi$. A zero-energy solution, $\lambda_i = 0$, implies the presence of a pair of Majorana-like excitations.

For a double QD h reads

$$h = \begin{pmatrix} \mu_1 & 0 & t'_{1,2} & -\Delta'_{1,2} \\ 0 & -\mu_1 & \Delta'_{1,2} & -t'_{1,2} \\ t'_{1,2} & \Delta'_{1,2} & \mu_2 & 0 \\ -\Delta'_{1,2} & -t'_{1,2} & 0 & -\mu_2 \end{pmatrix} . \tag{4.5}$$

Under the conditions $\Delta'_{1,2} = \pm t'_{1,2}$ and $\mu_1 = 0$, there are two MBSs that read

$$\gamma_1 = \frac{1}{\sqrt{2}}\left(d_1 \mp d_1^\dagger\right) ; \tag{4.6}$$

$$\gamma_2 = \frac{1}{\sqrt{2}\sqrt{1+\delta^2}}\left\{\left(d_2 \pm d_2^\dagger\right) - \delta\left(d_1 \pm d_1^\dagger\right)\right\} ; \tag{4.7}$$

where $\delta = \mu_2/2t'_{1,2}$. Only in the case where $\mu_2 = 0$ they are spatially separated [150].

For a triple QD h reads

$$h = \begin{pmatrix} \mu_1 & 0 & t'_{1,2} & -\Delta'_{1,2} & 0 & 0 \\ 0 & -\mu_1 & \Delta'_{1,2} & -t'_{1,2} & 0 & 0 \\ t'_{1,2} & \Delta'_{1,2} & \mu_2 & 0 & t'_{2,3} & -\Delta'_{2,3} \\ -\Delta'_{1,2} & -t'_{1,2} & 0 & -\mu_2 & \Delta'_{2,3} & -t'_{2,3} \\ 0 & 0 & t'_{2,3} & \Delta'_{2,3} & \mu_3 & 0 \\ 0 & 0 & -\Delta'_{2,3} & -t'_{2,3} & 0 & -\mu_3 \end{pmatrix} . \tag{4.8}$$

Assuming $\Delta'_{i,i+1} = \pm t'_{i,i+1}$ and $\mu_1 = 0$, there are always two MBSs given by

$$\gamma_1 = \frac{1}{\sqrt{2}}\left(d_1 \mp d_1^\dagger\right) ; \tag{4.9}$$

$$\gamma_2 = \frac{\left(d_3 \pm d_3^\dagger\right) - \alpha\left(d_2 \pm d_2^\dagger\right) + \beta\left(d_1 \pm d_1^\dagger\right)}{\sqrt{2}\sqrt{1+\alpha^2+\beta^2}} ; \tag{4.10}$$

where $\alpha = \mu_3/2t'_{2,3}$ and $\beta = \mu_2\mu_3/4t'_{1,2}t'_{2,3}$. In the case where μ_2 or μ_3 are zero the MBSs are spatially separated [151]. Interestingly, the manipulation of the onsite-energies allows us to change the localization of the MBSs, which would be relevant for their detection in transport [150].

4.2 Driven system: Floquet Majorana bound states

In the following, we apply external driving fields to modify periodically the onsite energies of the QDs and look for FMBSs as solutions of the non-equilibrium problem. The interest in periodically driven quantum systems lies on the fact that their stroboscopic dynamics are governed by a time-independent effective Hamiltonian, whose properties can be engineered according to the particular proposes. In this chapter, we use the so called van Vleck expansion for this effective Hamiltonian, whose first-order terms can be found in Appendix A.

As in chapter 3, to analyze a high-frequency driving, working in the interaction picture turns out to be very useful. Imagine that we modify periodically the onsite energies of the QDs by means of external gates such that the time-periodic perturbation to the static Hamiltonian is

$$V(t) = \sum_i A_i \cos\left(\omega t + \varphi_i\right) d_i^\dagger d_i \ . \tag{4.11}$$

The transformation to the interaction picture is then given by the operator $U(t) = \exp\left\{-i\int_0^t V(t')dt'\right\}$ and only the non-diagonal elements change depending on whether they commute or not with the time-periodic term:

$$\begin{aligned} \left[d_i^\dagger d_{i+1}, V(t)\right] &= d_i^\dagger d_{i+1}\left(A_{i+1}\cos\left(\omega t+\varphi_{i+1}\right) - A_i\cos\left(\omega t+\varphi_i\right)\right) \ ; \\ \left[d_i d_{i+1}, V(t)\right] &= d_i d_{i+1}\left(A_{i+1}\cos\left(\omega t+\varphi_{i+1}\right) + A_i\cos\left(\omega t+\varphi_i\right)\right) \ . \end{aligned} \tag{4.12}$$

Therefore, the renormalization of the hopping amplitude and the superconducting pairing depends on the geometry and the symmetry of the driving.

4.2.1 Double QD

Since this is an example of Floquet engineering, we are interested in a situation where the Majorana physics is related to the higher-order terms of the high-frequency expansion and not simply to the zeroth-order term or time-averaged Hamiltonian. Imagine that we drive just one gate such that $A_0 \equiv A_1$ and $A_2 = 0$. The Fourier components of the time-periodic Hamiltonian are then

$$h_m = \begin{pmatrix} \mu_1\delta_{m,0} & 0 & t_m & -\Delta_m \\ 0 & -\mu_1\delta_{m,0} & \Delta_{-m} & -t_{-m} \\ t_{-m} & \Delta_m & \mu_2\delta_{m,0} & 0 \\ -\Delta_{-m} & -t_m & 0 & -\mu_2\delta_{m,0} \end{pmatrix} , \tag{4.13}$$

where $t_m = t'_{1,2}J_m(A_0/\omega)$, $\Delta_m = \Delta'_{1,2}J_m(A_0/\omega)$ and $J_m(x)$ is the mth-order Bessel function of first kind. Even if we set the onsite energies to zero, $\mu_{1,2} = 0$, in the high-frequency regime it is only possible to obtain spatially separated FMBSs if $\Delta'_{1,2} = \pm t'_{1,2}$ since these two parameters are renormalized in the same way. However, the higher-order corrections allow to generate new sweet spots for FMBSs. While the first-order correction is zero, the effect of the second one is a slight

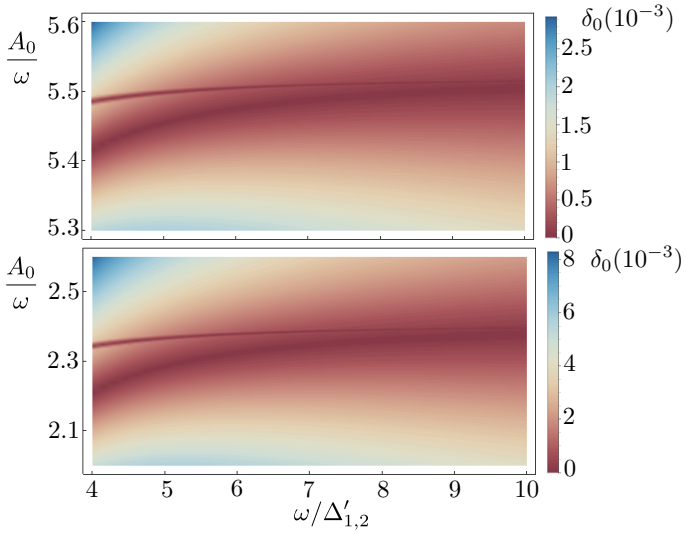

FIGURE 4.2. Quasienergy gap δ_0 for a superconducting double QD as a function of the amplitude and the frequency of the driving. The dark regions correspond to a closed gap, i.e., zero quasienergy. The plot shows that the 4-fold degeneracy at high frequency at the zero of the Bessel function $J_0(A_0/\omega)$ splits into two different sweet spots with FMBSs as the frequency decreases. The bottom panel shows the region around the first zero and the top panel around the second zero. Other parameters: $\mu_1 = \mu_2 = 0$, $t'_{1,2} = 0.8\Delta'_{1,2}$.

modification of $t'_{1,2}$ and $\Delta'_{1,2}$ to some effective values given by

$$t_{\text{eff}} = t'_{1,2} J_0\left(\frac{A_0}{\omega}\right) - \frac{4\left(t'_{1,2}\right)^2}{\omega^2} f\left(\frac{A_0}{\omega}\right) ; \tag{4.14}$$

$$\Delta_{\text{eff}} = \Delta'_{1,2} J_0\left(\frac{A_0}{\omega}\right) - \frac{4\left(\Delta'_{1,2}\right)^2}{\omega^2} f\left(\frac{A_0}{\omega}\right) ; \tag{4.15}$$

where $f\left(\frac{A_0}{\omega}\right)$ is a complicated function of Bessel functions. Considering only two sidebands ($J_{\pm n}\left(\frac{A_0}{\omega}\right) = 0$ for $n > 2$) its analytical expression is

$$f(x) = J_1^2(x)(J_0(x) + J_2(x)) . \tag{4.16}$$

As the ratio of the amplitude and the frequency of the driving field increases more terms contribute to function $f(x)$.

In this way, it is possible to choose the driving amplitude such that $\Delta_{\text{eff}} = \pm t_{\text{eff}}$ even when $\Delta'_{1,2} \neq t'_{1,2}$. In Fig. 4.2 we depict the quasienergy gap δ_0 as a function of the frequency and the amplitude once the on-site energies μ_1 and μ_2 are set to zero. As the static hopping amplitude and the superconducting pairing are different, i.e., $\Delta'_{1,2} \neq t'_{1,2}$, the quasienergies at high-frequency are all zero only at the zeros of the function $J_0(A_0/\omega)$ (approximately $A_0/\omega = 2.40, 5.52, 8.65...$). As the second-order correction becomes important, i.e., as the frequency decreases, two different

driving amplitudes allow for the condition required for the existence of FMBSs: the ones for which $\Delta_{\text{eff}} = \pm t_{\text{eff}}$. This is why at lower frequencies there are two quasienergy gap closings around each zero of the Bessel function, i.e., two different sweet spots (the bottom panel of Fig. 4.2 shows the gap around the first zero, ~ 2.40 and the top panel around the second one ~ 5.52). In the following we generalize this method for generation of FMBSs to a larger system, i.e., to an array of three QDs.

4.2.2 Triple QD

To obtain an analogous situation in a triple QD, such that all the non-diagonal terms of the Hamiltonian are renormalized in the same way at high-frequency, we drive the left and right QDs with gate voltages such that $A_0 \equiv A_1 = A_3$ and $A_2 = 0$. Let us choose for simplicity $t \equiv t'_{1,2} = t'_{2,3}$ and $\Delta \equiv \Delta'_{1,2} = \Delta'_{2,3}$. We analyze the presence of FMBSs as a function of the different parameters of the present setup, in particular of the phase difference between the driving fields $\varphi \equiv \varphi_3 - \varphi_1$.

If they are in phase, $\varphi = 0$, the Fourier components of the time-dependent Hamiltonian are

$$h_m = \begin{pmatrix} \mu_1\delta_{n,0} & 0 & t_m & -\Delta_m & 0 & 0 \\ 0 & -\mu_1\delta_{n,0} & \Delta_{-m} & -t_{-m} & 0 & 0 \\ t_{-m} & \Delta_m & \mu_2\delta_{n,0} & 0 & t_{-m} & -\Delta_m \\ -\Delta_{-m} & -t_m & 0 & -\mu_2\delta_{n,0} & \Delta_{-m} & -t_m \\ 0 & 0 & t_m & \Delta_m & \mu_3\delta_{n,0} & 0 \\ 0 & 0 & -\Delta_{-m} & -t_{-m} & 0 & -\mu_3\delta_{n,0} \end{pmatrix}, \tag{4.17}$$

where $t_m = tJ_m(A_0/\omega)$ and $\Delta_m = \Delta J_m(A_0/\omega)$. Due to the driving symmetry, if we only keep the zeroth-order term of the expansion for the effective Hamiltonian, h_0, all the non-diagonal terms vanish at the zeros of $J_0(A_0/\omega)$ such that there is effectively no hopping or superconducting pairing and the quasienergies are $\pm\mu_i$ for $i = 1,2,3$.

In the following, we show how the higher-order corrections to this high-frequency approximation generate FMBSs around these zeros. We will focus on the case $\mu_1 = \mu_2 = 0$, $\mu_3 \neq 0$ and $\Delta'_i \neq \pm t'_i$ because these conditions do not allow for FMBSs in the static case. In Fig. 4.3, we plot the gap of the quasienergy spectrum δ_0 as a function of the amplitude and the frequency of the driving. In the high-frequency regime the there is a four-fold degeneracy at $\epsilon = 0$ only at the zeros of the function $J_0(A_0/\omega)$ (approximately $A_0/\omega = 2.40, 5.52, 8.65...$). and there are no MBSs at all. At lower frequencies, two different driving amplitudes allow for the condition required for the existence of FMBSs, i.e., two different sweet spots. This is again due to the second-order correction to the effective Hamiltonian. The main effect of this term is a correction of the hopping amplitude and the superconducting pairing as

$$t_{\text{eff}} = tJ_0\left(\frac{A_0}{\omega}\right) - \frac{4t\left(2t^2-\Delta^2\right)}{\omega^2} f\left(\frac{A_0}{\omega}\right); \tag{4.18}$$

$$\Delta_{\text{eff}} = \Delta J_0\left(\frac{A_0}{\omega}\right) - \frac{4\Delta\left(2\Delta^2-t^2\right)}{\omega^2} f\left(\frac{A_0}{\omega}\right). \tag{4.19}$$

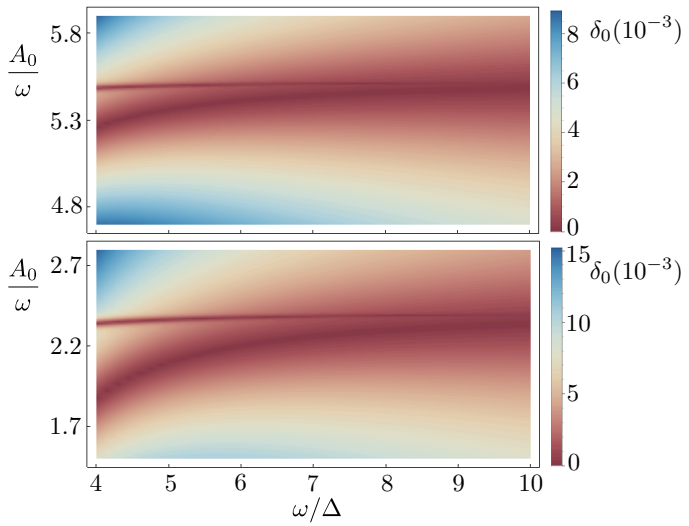

FIGURE 4.3. Quasienergy gap δ_0 for a superconducting triple QD as a function of the amplitude and the frequency of the driving. The dark regions corresponds to closed gap, i.e., zero quasienergy. The plot shows that the 4-fold degeneracy at high frequency at the zero of the Bessel function $J_0(A_0/\omega)$ splits into two different sweet spots with FMBSs as the frequency decreases. The bottom panel shows the region around the first zero and the top panel around the second zero. Other parameters: $\mu_1 = \mu_2 = 0$, $\mu_3 = 1.5\Delta$, $t = 0.8\Delta$, $\varphi = 0$.

One difference with the double QD system is that in this case a small effective hopping amplitude between QDs 1 and 3, $\tau_{1,3}$, appears due to virtual processes. The expression for this hopping is

$$\tau_{1,3} = \frac{\mu_3\left(\Delta^2 - t^2\right)}{\omega^2} \sum_{m=1}^{\infty} \frac{J_m\left(\frac{A_0}{\omega}\right)^2}{m^2} \,. \tag{4.20}$$

Moreover, the chemical potentials μ_2 and μ_3 are shifted, such that

$$\mu_{2,\text{eff}} = 2\frac{\mu_3(\Delta^2 - t^2)}{\omega^2} \sum_{m=1}^{\infty} \frac{J_m(A_0/\omega)^2}{m^2} \,; \tag{4.21}$$

$$\mu_{3,\text{eff}} = \mu_3 - 2\frac{\mu_3(\Delta^2 + t^2)}{\omega^2} \sum_{m=1}^{\infty} \frac{J_m(A_0/\omega)^2}{m^2} \,. \tag{4.22}$$

The shift in the chemical potentials only changes the localization of the bound states and the effect of the long-range hopping $\tau_{1,3}$ is small. In order to probe this, let us plot in Fig. 4.4 the quasienergy spectrum around zero and the functions $\Delta_{\text{eff}} \pm t_{\text{eff}}$ as a function of the driving amplitude. The sweet spots are very close to the zeros of these functions, indicating that the effect of $\tau_{1,3}$ is small. Finally, we calculate the localization of the FMBSs. Let us choose the FMBSs that appear when

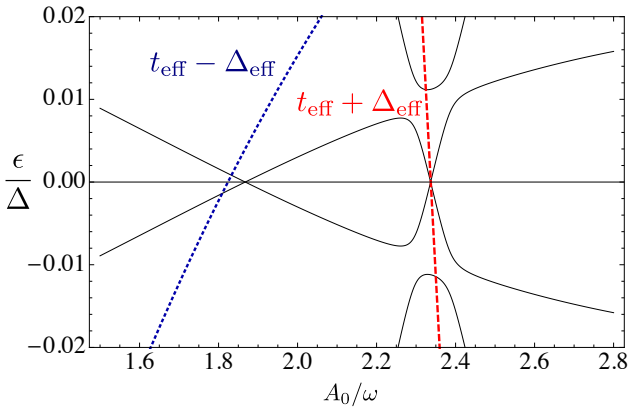

FIGURE 4.4. Lower part of the quasienergy spectrum for a superconducting triple QD as a function of the amplitude of the driving. The dotted (blue) line corresponds to $t_{\rm eff} - \Delta_{\rm eff}$ and the dashed (red) line to $t_{\rm eff} + \Delta_{\rm eff}$. We show that the FMBSs appear close to the conditions $\Delta_{\rm eff} = \pm t_{\rm eff}$. Other parameters: $\mu_1 = \mu_2 = 0$, $\mu_3 = 1.5\Delta$, $t = 0.8\Delta$, $\omega = 4\Delta$, $\varphi = 0$.

$t_{\rm eff} = \Delta_{\rm eff}$ (left zero in the plot of Fig. 4.4). Their analytical expression to second-order reads

$$\gamma_1 = \frac{1}{\sqrt{2}}\left(d_1 - d_1^\dagger\right); \tag{4.23}$$

$$\gamma_2 = a_1\left(d_1 - d_1^\dagger\right) + a_2\left(d_2 - d_2^\dagger\right) + a_3\left(d_3 - d_3^\dagger\right); \tag{4.24}$$

with normalization $\sum_{i=1}^{3} 2a_i^2 = 1$. In the bar diagram in Fig. 4.5 the value of the constants a_i for different values of the chemical potential μ_3 is shown. Interestingly, Fig. 4.5 shows that for certain values of the chemical potential μ_3 the two FMBSs are spatially separated and that it is possible to tune the position of γ_2.

Interestingly, the phase difference between the local driving gate voltages within each QD plays an important role. The existence of sweet spots for FMBSs depends on this relative phase. For instance, for opposite phases, $\varphi = \pi$, the zeroth-order term of the expansion does not change with respect to the previous case but the second-order one does change. The new effective parameters are

$$t_{\rm eff} = tJ_0\left(\frac{A_0}{\omega}\right) - \frac{2t\left(t^2+\Delta^2\right)}{\omega^2} f\left(\frac{A_0}{\omega}\right); \tag{4.25}$$

$$\Delta_{\rm eff} = \Delta J_0\left(\frac{A_0}{\omega}\right) - \frac{2\Delta\left(t^2+\Delta^2\right)}{\omega^2} f\left(\frac{A_0}{\omega}\right). \tag{4.26}$$

Therefore the functions $\Delta_{\rm eff} \pm t_{\rm eff}$ are zero for the same value of A_0 in contrast with the previous case ($\varphi = 0$). In Fig. 4.6 we show the gap of the quasienergies δ_0 as a function of the phase difference and the amplitude of the driving. The measurement of this φ-dependence would be an important signature of the existence of FMBSs.

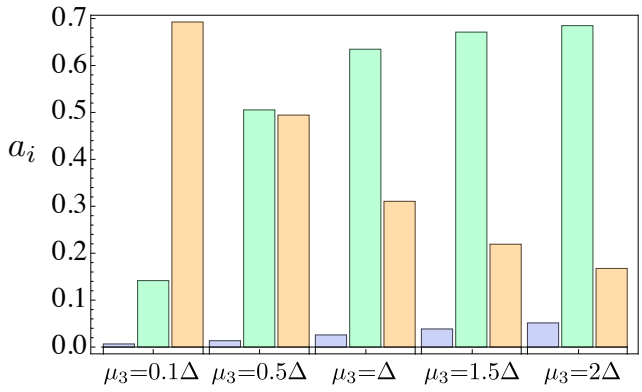

FIGURE 4.5. Spatial location of the pair of FMBSs that appears when $t_{\text{eff}} = \Delta_{\text{eff}}$. The blue, green and orange bars are respectively a_1, a_2 and a_3 (see Eqs. 4.23 and 4.24). Other parameters: $\mu_1 = \mu_2 = 0$, $t = 0.8\Delta$, $\omega = 4\Delta$, $\varphi_3 - \varphi_1 = 0$.

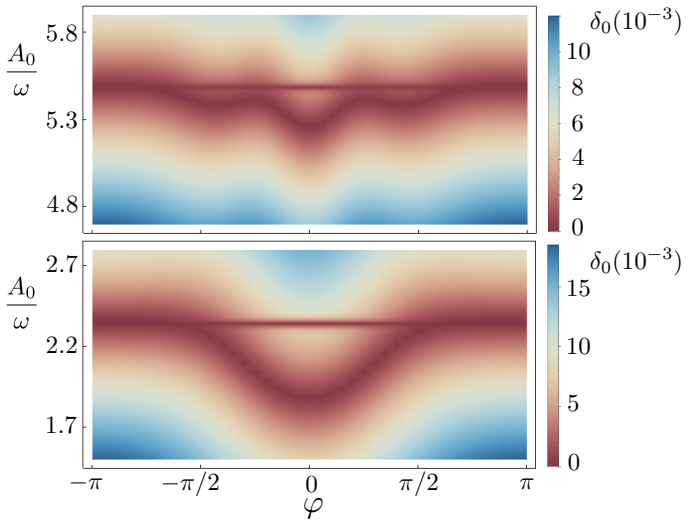

FIGURE 4.6. Quasienergy gap for a superconducting triple QD as a function of the amplitude and the relative phase φ. The dark regions correspond to closed gap, i.e., zero quasienergy. The plot shows that one of the sweet spots varies with the phase, while the other does not. The bottom panel shows the region around the first zero of the function $J_0(A_0/\omega)$ and the top panel around the second zero. Other parameters: $\mu_1 = \mu_2 = 0$, $\mu_3 = 1.5\Delta$, $t = 0.8\Delta$, $\omega = 4\Delta$.

4.3 Conclusions

To summarize, we have discussed the existence of FMBSs in two different configurations of QDs driven by periodic gate voltages and coupled through superconducting leads. The simplicity of these systems and their tunability in comparison with other proposed setups which provide MBSs deserve to consider them as suitable solid state devices to host MBSs. We have shown the

existence of FMBSs by means of the expansion of an effective Floquet Hamiltonian in a power series. By modifying the frequency of the driving field applied to a double QD it is possible to control the existence of a series of sweet spots. Moreover, we analyze a driven triple QD and we predict the existence of sweet spots as a function of the relative phase of the local drivings. This method for FMBSs generation can be extended to chains of QDs with more than three sites. One would expect that as the number of QDs increases, the localization of the FMBSs changes and Eqs. (4.23) and (4.24) would be generalized. Experimentally, the recent achievements in the fabrication and control of triple [58, 156, 157] and even quadruple semiconductor QDs [158], also for driven configurations [57], open the avenue for the experimental realization of hybrid configurations with superconductor contacts where FMBSs can be experimentally investigated.

The existence of these exotic dynamical quasiparticles can be detected by connecting two metallic leads and measuring transport [150, 151, 159, 160]. The signatures of FMBSs will be present in the differential conductance measurement by the satisfaction of the Floquet sum rule [137].

CHAPTER 5

FULL-COUNTING STATISTICS OF TIME-DEPENDENT CONDUCTORS

As explained in chapter 2 an interesting way to extract information from a quantum system is to allow the exchange of particles with some reservoirs and measure the transported charge for different conditions. In particular, the statistics of the current through the central quantum system might be a good indicator of its nature. In this chapter we develop a scheme for the computation of the statistics of transport setups described by Markovian master equations with an arbitrary time dependence [**P.8**].

In section 5.1 we introduce the formalism of full-counting statistics (FCS) and explain the basis for our computation scheme. As a test bench for the evaluation of its numerical stability, we consider time-independent problems for which the FCS can be computed by other means in section 5.2. As applications, we study in section 5.3 cumulants of higher order for two time-dependent transport problems of recent interest, namely steady-state coherent transfer by adiabatic passage (CTAP) and Landau-Zener-Stückelberg-Majorana (LZSM) interference in an open double quantum dot (QD).

5.1 Full-counting statistics

5.1.1 Current fluctuations

In a mesoscopic device the transport is a stochastic process, since it consists in single-electron tunneling events, and therefore it fluctuates. Current fluctuations can be characterized by the low-frequency limit of the current-correlation functions. A special focus lies on the second order one, called shot noise, which corresponds to the variance of the transported charge [161]. Its ratio with the current determines the Fano factor, a dimensionless measure for the noise level that hints at the nature of the transport mechanism, using the Poisson process as reference [162].

Going beyond the variance, one may consider the FCS of the transported electrons [162–166] or the related waiting-time distribution of consecutive transport events [167].

While typically undesirable in technical applications, current fluctuations can be useful for understanding quantum-mechanical transport processes [168]. For instance, an open transport channel with transmission close to unity leads to sub-Poissonian noise, while super-Poissonian noise may hint on electron bunching [162], the size of the charge carriers [169], or bistabilities [89, 166, 170]. External driving fields enable the control of the noise level via the driving amplitude and frequency [171]. Particular examples of such driven conductors with low current noise are pumps that transport a fixed charge per cycle [172–175]. Moreover, noise measurements may provide evidence for the correct operation of protocols that induce a steady-state version [176] of CTAP [38, 177, 178].

In the present work we introduce the concept of FCS to calculate the statistics of transported charges through a general conductor. As the existent effective methods were generally not applicable for conductors with an arbitrary time dependence, it is necessary to seek for alternatives. In a recent work [179] an efficient approach based on a density-operator-like object was developed for the computation of the shot noise of the transported charge. A numerical solution of the corresponding equations of motion provides the current and its variance with moderate numerical effort. With the present work, we extend this idea and derive a propagation method for computing current cumulants up to a given order. Another option is a number-resolved master equation in which the number of transported electrons is introduced as an additional degree of freedom [180, 181]. However, the distribution of this number may be rather broad and, thus, the computational effort may become tremendous.

As we show in Appendix B, in the regime of relatively small dot-lead coupling and Markovian leads, an established way to describe transport are master equations of Lindblad type [182–184]. In combination with a Floquet treatment for the central system, they can be applied to periodically driven transport problems. In the infinite-bias limit, these time-dependent master equations have a simple form. In this thesis, we consider transport problems that can be captured by a master equation of the form

$$\dot{\varrho} = -i[H(t), \varrho] + \sum_{\ell} \mathscr{D}(L_\ell(t))\varrho \equiv \mathscr{L}(t)\varrho, \tag{5.1}$$

where $H(t)$ accounts for the coherent quantum dynamics of a central conductor such as a QD array driven by time-dependent gate voltages. The conductor is coupled to two or more electron reservoirs, denoted by ℓ, that allow for incoherent electron tunneling from and to the reservoirs. These processes are described by the generally also time-dependent Lindblad dissipators $\mathscr{D}[L_\ell(t)]$ (see Eq. 2.17). Among these dissipative terms, it is important to identify the ones that connect Hilbert subspaces with different number of particles in the central system. They are usually called forward and backward current superoperators J_ℓ^+ and J_ℓ^-, respectively. For a specific example of these superoperators see below.

While the master equation (5.1) contains the full information about the central conductor, the leads degrees of freedom have been traced out in course of its derivation (Appendix B). As we are interested in the statistics of the transport, we need to generalize the master equation formalism by introducing a counting variable χ which keeps track of the electron number in the leads.

5.1.2 Counting variable

The electron transport can be considered as a stochastic process with the random variable N_ℓ, the net number of electrons transported to lead ℓ or, equivalently, the electron number in that lead (to achieve a compact notation, we henceforth suppress the lead index ℓ and the time argument). Its statistical properties can be captured by the moment generating function

$$Z(\chi) = \langle e^{i\chi N} \rangle = \sum_{k=0}^{\infty} \frac{(i\chi)^k}{k!} \mu_k, \tag{5.2}$$

with the moments $\mu_k = \langle N^k \rangle = (\partial/\partial i\chi)^k Z(\chi)|_{\chi=0}$, while their irreducible parts, the cumulants κ_k, are generated from $\log Z(\chi)$ [185]. For Markovian time-independent transport problems, the cumulants eventually grow linearly in time [165] which motives the definition of the *current cumulants* as the time derivatives $c_k = \dot{\kappa}_k$, which are our main quantities of interest. Their generating function (current cumulant generating function) reads

$$\phi(\chi) = \frac{d}{dt} \log Z(\chi) = \sum_{k=1}^{\infty} \frac{(i\chi)^k}{k!} c_k, \tag{5.3}$$

which implies $c_k = (\partial/\partial i\chi)^k \phi|_{\chi=0}$.

As stated above, it is possible to generalize the master equation formalism to keep track of the electron number in lead ℓ. To this end one multiplies the full density operator by a counting factor $e^{i\chi N}$ for the lead electrons to obtain the generalized density operator $R(\chi)$. It relates to the moment generating function (Eq. 5.2) via $\mathrm{tr} R(\chi) = Z(\chi)$ and obeys the generalized master equation [165]

$$\dot{R}(\chi) = [\mathscr{L}(t) + J(\chi)] R(\chi). \tag{5.4}$$

The additional term

$$J(\chi) = (e^{i\chi} - 1) J^+ + (e^{-i\chi} - 1) J^- \tag{5.5}$$

is composed of the forward and the backward current superoperators $J^\pm$ mentioned above.

5.1.3 Hierarchy of master equations

The generalized master equation (5.4) together with the generating functions (5.2) and (5.3) in principle already provides the current cumulants c_k. For master equation descriptions of time-independent transport, this calculation consists in a non-Hermitian eigenvalue problem with a subsequent computation of derivatives with respect to the counting variable [165]. For systems

with very few degrees of freedom, this may provide all cumulants analytically [165, 166]. However, for more complex or time-dependent systems, one has to numerically evaluate these expressions, which is hindered by two obstacles. First, the numerical computation of derivatives becomes increasingly difficult with the order. Second, the relation between cumulants and moments is known only implicitly via the Taylor series for $Z(\chi)$ and $\phi(\chi)$. Therefore we have to bring the generalized master equation to a form that is more suitable for extracting information about the current cumulants c_k.

We start by writing the current cumulant generating function in terms of the generalized density operator $R(\chi)$. From the definitions $\phi(\chi) = \frac{d}{dt}\log Z(\chi)$ and $Z(\chi) = \mathrm{tr} R(\chi)$ together with the generalized master equation (5.4) follows straightforwardly

$$\phi(\chi) = \frac{1}{Z(\chi)}\,\mathrm{tr}\, J(\chi)R(\chi) = \mathrm{tr}\, J(\chi)X(\chi)\ , \tag{5.6}$$

(because $\mathrm{tr}\,\mathscr{L}\ldots = 0$) with the auxiliary operator

$$X(\chi) = \frac{1}{Z(\chi)}R(\chi). \tag{5.7}$$

Moreover, we find the equation of motion

$$\dot{X}(\chi) = \mathscr{L}(t)X(\chi) + [J(\chi) - \phi(\chi)]X(\chi). \tag{5.8}$$

We continue by substituting the dependence on the continuous counting variable χ by the Taylor coefficients X_k and J_k which we define via the series $X(\chi) = \sum_{k=0}^{\infty}(i\chi)^k X_k/k!$ and $J(\chi) = \sum_{k=1}^{\infty}(i\chi)^k J_k/k!$. Note that $J(0) = 0$ such that $J_0 = 0$, while $J_k = J^+ + (-1)^k J^-$ for $k > 0$. Finally, we obtain from Eqs. (5.3), (5.6) and (5.8) the hierarchy of equations

$$c_k = \sum_{k'=0}^{k-1}\binom{k}{k'}\mathrm{tr}\, J_{k-k'}X_{k'}\ ; \tag{5.9}$$

$$\dot{X}_k = \mathscr{L}(t)X_k + \sum_{k'=0}^{k-1}\binom{k}{k'}(J_{k-k'} - c_{k-k'})X_{k'}. \tag{5.10}$$

It constitutes the central formal achievement of this work and forms the basis of the numerical results presented below.

Two features are worth being emphasized. First, in the limit $\chi \to 0$, $X(\chi)$ becomes the reduced density operator ($X_0 = \varrho$), i.e., for $k = 0$, Eq. (5.10) is identical to the master equation (5.1). Since $\mathrm{tr} X(\chi) = 1$ by definition this implies $\mathrm{tr} X_k = \delta_{k,0}$. Second, as an important consequence of $J_0 = 0$ and $c_0 = 0$, the summations on the r.h.s. of these equations terminate at $k' = k-1$, which implies that X_k and c_k depend only on terms of lower order. This enables the truncation at arbitrary order and, thus, the iterative computation of the current cumulants. The first step is to solve the master equation to obtain ϱ (or equivalently X_0). Then one can compute the current

$$I \equiv c_1 = \mathrm{tr}\left(J^+ - J^-\right)\varrho\ . \tag{5.11}$$

With this result one can solve the equation

$$\dot{X}_1 = \mathscr{L}(t)X_1 + (J^+ - J^- - I)\varrho, \tag{5.12}$$

use it to compute the second current cumulant, commonly called shot noise,

$$S \equiv c_2 = 2\,\mathrm{tr}\left\{J^+ - J^-\right\}X_1 + \mathrm{tr}\left\{J^+ + J^-\right\}\varrho\ , \tag{5.13}$$

etc. In general, it is numerically more stable to solve the system of equations

$$\dot{\varrho} = \mathscr{L}(t)\varrho\ , \tag{5.14}$$

$$\dot{X}_1 = \mathscr{L}(t)X_1 + (J^+ - J^- - \mathrm{tr}\left\{J^+ - J^-\right\}\varrho)\varrho\ , \tag{5.15}$$

$$\dot{X}_2 = \mathscr{L}(t)X_2 + \ldots\ , \tag{5.16}$$

$$\vdots$$

all at once.

The numerical effort of our scheme can be estimated as follows. Let us assume that (if necessary after a full or a partial [186] rotating-wave approximation) the Liouvillian $\mathscr{L}(t)$ can be written as a $d \times d$-matrix and that its smallest decay rate is $\gamma_{\min}$. Then to compute the first $k_{\max}$ cumulants, we have to propagate $k_{\max}d$ scalar equations for a time $\tau \approx 3/\gamma_{\min}$, where one is typically interested in the first $k_{\max} = 5$–10 cumulants.

To highlight the efficiency of our method, we compare this effort with that of the number-resolved master equation [180, 181], for which the density operator is extended by a variable $n = 0, \ldots, n_{\max}$ that accounts for the number of transported electrons. In the Markovian case, coherences between different n do not play a role, such that one essentially has to replace ϱ by the $n_{\max}+1$ density operators $\varrho^{(n)}$, where $\mathrm{tr}\,\varrho^{(n)}$ is the probability that n electrons have arrived at a certain lead. During the time τ, on average $I\tau$ electrons flow, so that one would have to employ a number-resolved master equation with $n_{\max} \approx 2I\tau = 6I/\gamma_{\min}$, i.e., one has to integrate $\sim 6Id/\gamma_{\min}$ scalar equations. This means that whenever $I \gg \gamma_{\min}$, our method outperforms this alternative significantly. This is for example the case when the system infrequently switches between two states with different conductance [89, 166, 170]. A further advantage of our method is that it provides direct access to the cumulants, such that the detour via the moments can be avoided.

As we said above, in most of the applications, it is worthwhile to define the Fano factor, $F_1 = S/I \equiv c_2/c_1$, which is a dimensionless measure of the noise strength and gives information about the transport mechanism [162]. The value $F_1 = 1$ corresponds to uncorrelated events, while larger values usually indicate bunching. For more profound statements, one has to consider also cumulants of higher order. In the following we consider the cumulant ratios

$$F_k = c_{k+1}/c_k; \quad k = 1, 2, 3\ldots\ . \tag{5.17}$$

Despite the general validity of our formalism, in all the applications in this thesis, we consider an array of n QDs with the first QD coupled to an electron source S, while the last one is coupled

to a drain D. As derived in Appendix B, if source and drain are strongly biased one can work in the infinite-bias limit and the master equation simplifies to

$$\dot{\varrho} = -i[H(t),\varrho] + \frac{\Gamma_S}{2}\mathscr{D}(d_1^\dagger)\varrho + \frac{\Gamma_D}{2}\mathscr{D}(d_n)\varrho, \tag{5.18}$$

with the Lindblad dissipator defined in Eq. (2.17) and the dot-lead tunneling rates $\Gamma_{S/D}$. Then, the forward current superoperator from the source to the system is $J_S^+\varrho \equiv \Gamma_S d_1^\dagger \varrho d_1$, while the backward current superoperator J_S^- vanishes because transport is unidirectional. Note that evaluating the current at the drain would give the same result.

5.1.4 Relation to the iterative scheme for time-independent transport

In the previous derivation, Eqs. (5.9) and (5.10) resemble the iterative scheme derived in Refs. [187, 188] for the cumulants of time-independent transport problems. Let us therefore establish a connection between both methods. If $\mathscr{L}$ is time-independent, the original master equation possesses a stationary solution ϱ_∞. For $k > 0$, since $\mathrm{tr}X_k = \delta_{k,0}$, Eq. (5.10) possesses also a stationary solution. Therefore, we have to solve

$$\mathscr{L}X_k = -\sum_{k'=0}^{k-1}\binom{k}{k'}(J_{k-k'} - c_{k-k'})X_{k'}, \tag{5.19}$$

under the condition $\mathrm{tr}X_k = \delta_{k,0}$. In conclusion, in the time-independent limit, our method is equivalent to the iteration scheme of Refs. [187, 188] and, thus, represents a generalization of these works.

5.1.5 Hierarchy of equations for the moments

While the virtue of our scheme is the direct access to the current cumulants c_k, it is worthwhile to compare it with the corresponding iteration for the moments μ_k derived in Refs. [189, 190]. It can be obtained from the Taylor expansions of $Z(\chi) = \mathrm{tr}R(\chi)$ and of the generalized master equation (5.4) which read

$$\mu_k = \mathrm{tr}R_k; \tag{5.20}$$

$$\dot{R}_k = \mathscr{L}(t)R_k + \sum_{k'=0}^{k-1}\binom{k}{k'}J_{k-k'}R_{k'}; \tag{5.21}$$

respectively. These equations look simpler than the corresponding expressions for the cumulants. However, the subsequent computation of the current cumulants is cumbersome. It can be achieved by the recurrence relation

$$c_k = \dot{\mu}_k - \sum_{k'=1}^{k-1}\binom{k-1}{k'-1}c_{k'}\dot{\mu}_{k-k'}, \tag{5.22}$$

which follows straightforwardly from Eqs. (5.2) and (5.3). Notice that in contrast to Refs. [189, 190], we do not consider number cumulants, but current cumulants. Therefore one first has to

compute the time derivatives of the moments,

$$\dot{\mu}_k = \operatorname{tr} \dot{R}_k = \sum_{k'=0}^{k-1} \binom{k}{k'} \operatorname{tr} J_{k-k'} R_{k'} \tag{5.23}$$

and then compute the cumulants using Eq. (5.22).

The computation of the c_k from Eqs. (5.20)–(5.23) may be numerically challenging, in particular when, e.g., for strong bunching the cumulants grow rapidly with their order. Then Eq. (5.22) includes small differences of large numbers, which typically are sensitive to rounding errors.

5.2 Time-independent models as test cases

Before addressing time-dependent transport problems, let us start with two time-independent systems which can be solved either analytically or with the iteration scheme in Eq. (5.19). This allows us to draw conclusions about the numerical stability of our method.

5.2.1 Single-electron transistor

One of the simplest quantum transport setups is the single-electron transistor (SET), which consists of a resonant level between two strongly biased leads. It can be occupied by at most one electron such that the Liouvillian and the forward current superoperators read

$$\mathscr{L} = \begin{pmatrix} -\Gamma_S & \Gamma_D \\ \Gamma_S & -\Gamma_D \end{pmatrix}; \qquad J^+ = \begin{pmatrix} 0 & 0 \\ \Gamma_S & 0 \end{pmatrix}; \tag{5.24}$$

respectively. For the symmetric case, $\Gamma_S = \Gamma_D \equiv \Gamma$, the current cumulants of the SET are known analytically as $c_k = 2^{-k}\Gamma$ [165], which makes this system an ideal test case. Consequently, all cumulant ratios are identical to the Fano factor, $F_k = 1/2$. For any $\Gamma_S \neq \Gamma_D$, the cumulants cannot be written in a closed form, but exhibit a generic behavior: While cumulants of low order reflect the nature of the transport process, high-order cumulants oscillate in a universal manner [191]. Therefore the symmetric case with its constant $F_k = 1/2$ is rather special and should be sensitive to numerical errors.

By numerically solving Eqs. (5.9) and (5.10), we have found that for the symmetric case the first $\gtrsim 30$ cumulant ratios agree with the analytical prediction with a precision $\lesssim 1\%$ (not shown). For slight asymmetries, we compare in Fig. 5.1 (a) our results with those obtained by the traditional iteration scheme Eq. (5.19). Both agree rather well also for orders at which the cumulants exhibit universal oscillations.

5.2.2 Triple QD in a ring configuration

As a further test case, we consider a ring of three QDs, where QD 1 and QD 3 are coupled to source and drain, respectively. Since in such a ring, the electrons may be transported by direct tunneling

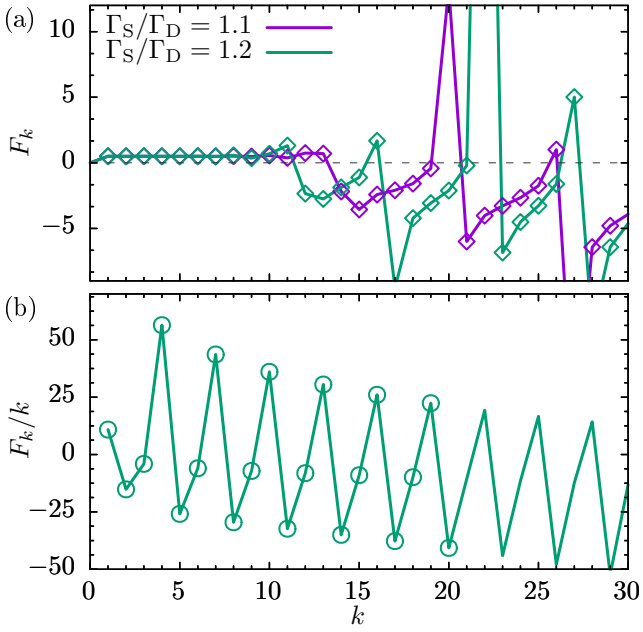

FIGURE 5.1. Cumulant ratios F_k for time-independent test cases. The symbols are obtained with our propagation method, while the lines interpolate the results of the iteration scheme based on Eq. (5.19). (a) Asymmetric SET for large bias and various dot-lead rates $\Gamma_{S/D}$. (b) Triple QD in ring configuration with $\Gamma_S = \Gamma_D = 0.1\tau$, where QD 2 is detuned by $\epsilon = 10\tau$. For graphical reasons, we plot F_k/k.

from the first to the last QD or via QD 2, the conductance is governed by interference [192, 193] and may suffer from decoherence [194]. Here we consider a gate voltage that shifts the onsite energy of QD 2 by ϵ such that the corresponding single-particle Hamiltonian reads

$$H = \begin{pmatrix} 0 & \tau & \tau \\ \tau & \epsilon & \tau \\ \tau & \tau & 0 \end{pmatrix}. \tag{5.25}$$

For strong detuning, $\epsilon \gg \tau$, the path via QD 2 has the effective tunnel matrix element $\tau^2/\epsilon \ll \tau$. Thus in the limit of strong Coulomb repulsion, the situation is that of a slow and a fast channel which block one another [195]. This typically leads to bunching visible in a super-Poissonian Fano factor [166]. The triple QD ring combines several difficulties such as different time scales, quantum interference, and cumulants that grow exponentially with their index [195]. The corresponding stiff differential equations represent challenging test cases for propagation methods.

In Fig. 5.1(b) we again compare the results of our method with those of the iteration of Eq. (5.19). As for the SET, we find that for the first 20 cumulants, the results of both methods are practically indistinguishable. In the present case, calculations for more than roughly 15 cumulants require a rather high numerical precision and, thus, are time consuming. Nevertheless,

we can conclude that for the experimentally relevant orders, our scheme is still efficient and numerically stable.

5.3 Application to time-dependent conductors

To demonstrate the practical use of our time-dependent iteration scheme, we apply it to various physical situations that have been studied recently, i.e., we generalize previous calculations of the current or the Fano factor to cumulants of higher order.

5.3.1 Steady-state coherent transfer by adiabatic passage

Let us consider a linear triple QD described by the single-particle Hamiltonian

$$H(t) = \begin{pmatrix} 0 & \Omega_{12}(t) & 0 \\ \Omega_{12}(t) & 0 & \Omega_{23}(t) \\ 0 & \Omega_{23}(t) & 0 \end{pmatrix}. \tag{5.26}$$

If the tunnel couplings Ω_{ij} are switched adiabatically slowly, the system may follow the adiabatic eigenstate $\propto (\Omega_{23}, 0, -\Omega_{12})^T$. In this way, it is possible to transfer an electron from QD 1 to QD 3 without populating the middle QD [177], an effect known as CTAP. This non-local version of an optical Lambda transition [196] has also been predicted for atoms in multi-stable traps [38, 178]. Experimental evidence of the direct tunneling from the first to the last QD is hindered by the backaction of a population measurement, which creates decoherence [197] and, thus, may induce the effect that one wishes to demonstrate. To circumvent this problem, it has been suggested [176] to contact the triple QD to an electron source and drain and to employ the sequence of double Gauss pulses

$$\Omega_{12/23}(t) = \sum_{n=0}^{\infty} \Omega_{\max} \exp\Big[-\frac{(t \mp \Delta t/2 - nT)^2}{2\sigma^2} \Big], \tag{5.27}$$

with width σ, delay Δt, and repetition time T, as is sketched in Fig. 5.2 (a). Notice the so-called counter intuitive order of the pulses in which the tunnel matrix element Ω_{23} is active before Ω_{12}. In the ideal case, this sequence will lead to the transport of one electron per double pulse and, thus, induce a current with a low Fano factor which may serve as experimental verification of CTAP.

We assume that Coulomb repulsion inhibits the occupation with more than one electron and compute the time evolution of the first cumulants. While the second current cumulant has been already considered in Ref. [176], here we focus on cumulants of higher order. Fig. 5.2 (b) shows that after a transient stage of roughly $10T$, the dynamics assumes its long time limit. The time evolution illustrates that generally the duration of the transient stage increases with the cumulant order.

The central issue of verifying CTAP via noise measurements is the correlation between the Fano factor and the population of the middle QD as a function of the driving period T. By contrast,

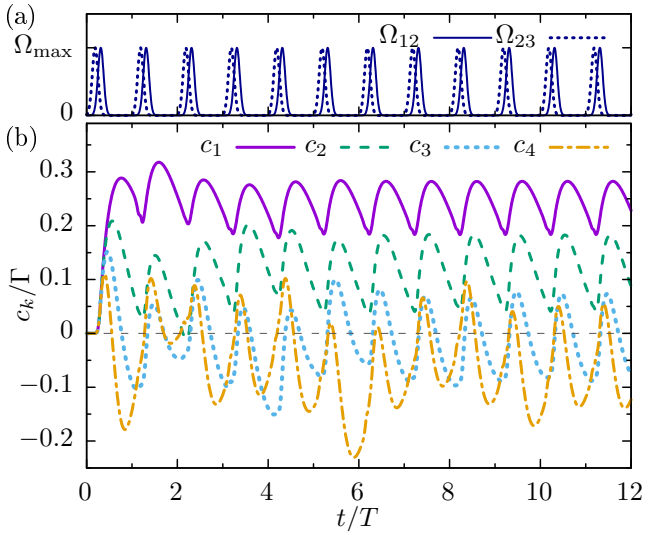

FIGURE 5.2. (a) Pulsed tunnel matrix elements which lead to an adiabatic passage of electrons from QD 1 to QD 3 in a linear triple QD (Eq. 5.27). Each pulse has a width $\sigma = T/16$. The delay within a double pulse is $\Delta t = T/8$, while the time between the pairs is $T = 40/\Omega_{\max}$. (b) Corresponding time evolution of the current cumulants c_k, $k = 1,\ldots,4$, for the dot-lead rates $\Gamma_S = \Gamma_D = 0.05\Omega_{\max}$.

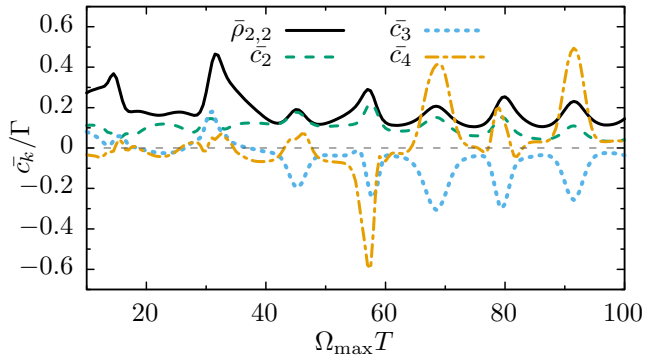

FIGURE 5.3. Time-averaged population of the central QD for steady-state CTAP as a function of the driving period T together with the cumulants $c_{2,3,4}$ averaged over one driving period. All other parameters are as in Fig. 5.2.

the current correlates only weakly with the population and cannot serve as indicator [176]. Going beyond this, we compute the steady-state values of the cumulants and plot in Fig. 5.3 the average value over one driving period $\bar{c}_k$. We find that the third cumulant also correlates with the occupation, while for the fourth cumulant only the absolute value behaves in this way. Interestingly enough, the profile of $\bar{c}_3$ and $\bar{c}_4$ cumulant is even sharper than that of the zero-frequency noise $\bar{c}_2$ considered in Ref. [176]. Thus, the measurement of further cumulants will strengthen the evidence for the correct operation of a steady-state CTAP protocol.

5.3.2 Landau-Zener interference

A paradigmatic example for time-dependent quantum mechanics is a two-level system with the single-particle Hamiltonian

$$H(t) = \frac{1}{2}\begin{pmatrix} \epsilon(t) & \tau \\ \tau & -\epsilon(t) \end{pmatrix}, \tag{5.28}$$

the hopping amplitude τ, and the time-dependent splitting

$$\epsilon(t) = \epsilon_0 + A\cos(\omega t). \tag{5.29}$$

For driving amplitudes $A \gtrsim \epsilon_0$, the eigenenergies of $H(t)$ as a function of time form avoided crossings. At these crossings, an electron may perform Landau-Zener transitions, such that repeated sweeps lead to the so-called LZSM interference. In a closed system, this is visible in a characteristic pattern of the population as a function of the detuning ϵ_0 and the amplitude A [198]. Having been measured originally for the population of superconducting qubits [80, 81], such patterns have been found also for the current in a biased open double QD [82, 83]. For deeper understanding, we extend previous results for the average current to a study of current cumulants.

Fig. 5.4 (a) shows the LZSM interference pattern for the time-averaged current, i.e., the first current cumulant $\bar{c}_1$. It exhibits the typical structure found in the high-frequency regime, namely Lorentzian resonance peaks which are modulated along the A-axis by the squares of Bessel functions [83]. For the second cumulant [see Fig. 5.4 (b)], the corresponding peaks split into double peaks whose local minima coincide with the current maxima. As a consequence, the corresponding Fano factor [see Fig. 5.4 (c)] assumes clearly sub-Poissonian values of $F_1 \approx 1/2$, while off the resonance, the Fano factor indicates Poissonian transport.

For a closer and more quantitative investigation, we depict in Fig. 5.5 the first 4 cumulants as a function of the detuning ϵ_0 for constant driving amplitude. On the one hand, this highlights the double peak structure of $\bar{c}_2$ and indicates that at the edge of the current peaks $\bar{c}_2 \approx \bar{c}_1$ which corresponds to the Poissonian value $F_1 \approx 1$. The third and the fourth cumulants possess a similar double peak structure, where the magnitude of the $\bar{c}_k$ diminishes with the order k. This affirms the low-noise properties of resonantly driven transport in coupled QDs [199].

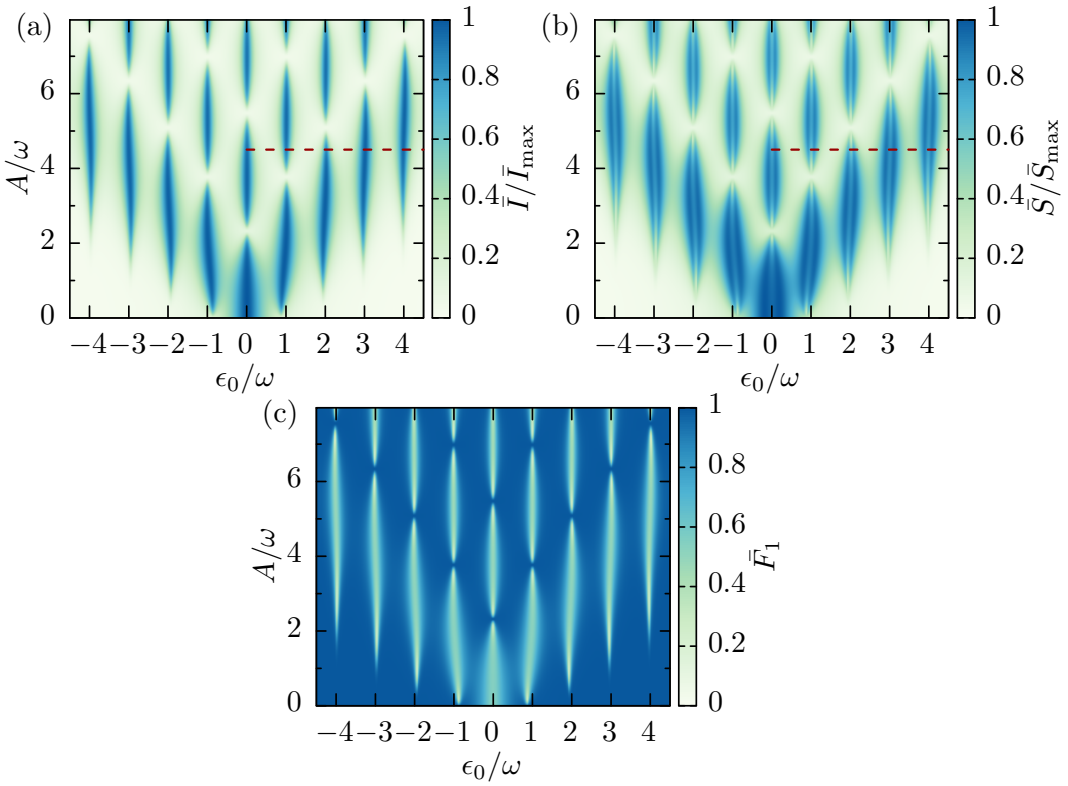

FIGURE 5.4. (a) Average current $\bar{I}$, (b) zero-frequency noise $\bar{S}$ and (c) Fano factor $\bar{S}/\bar{I}$ for a strongly biased driven double QD as a function of the detuning ϵ_0 and the driving amplitude A. The driving frequency and the dot-lead rates are $\omega = 2\tau$ and $\Gamma_S = \Gamma_D = 0.15\tau$, respectively. The dashed horizontal lines mark the amplitude considered in Fig. 5.5.

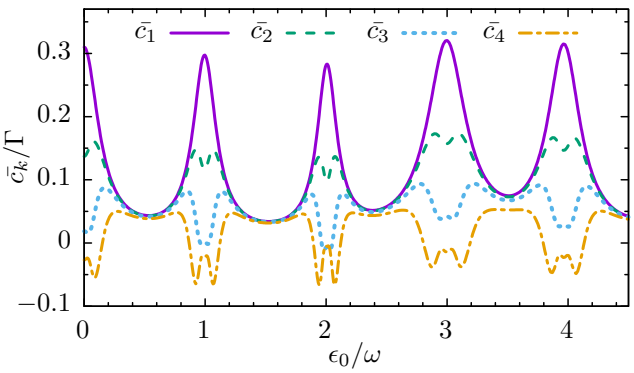

FIGURE 5.5. First four cumulants c_k for the LZSM interference patterns for the driving amplitude $A = 4.5\omega$ marked in Fig. 5.4 (a,b) by a horizontal line.

5.4 Conclusions

We have developed a method for the iterative computation of current cumulants for conductors described by a time-dependent Markovian master equation. For such transport problems the only generic way to obtain a solution is a numerical propagation while generally eigenvalue-based methods are not applicable. Our scheme is based on a hierarchy of density-operator-like objects truncated according to the desired number of cumulants (see Eq. 5.10). The cumulants follow in a direct manner by taking the trace (see Eq. 5.9). As compared to the propagation of a number-resolved density matrix, our scheme possesses two advantages. First, it generally gets along with a significantly smaller set of equations. Second, there is no need to compute the cumulants from the moments, numerically critical task that may involve computing small differences of much larger numbers.

As a test bench, we have employed two time-independent master equations which can be solved also with previously known eigenvalue-based methods. It turned out that our scheme provides reliable results for roughly the first 20 cumulants even for challenging test cases. For less demanding situations, computing more than 30 cumulants is feasible. Thus, we reach orders way beyond the present experimental needs.

We have applied our scheme to two time-dependent systems of recent interest. For steady-state CTAP, we have found that not only the second cumulant, but also higher ones correlate with the population of the middle QD. Therefore they may provide additional evidence for the correct operation of a CTAP protocol. A similar conclusion can be drawn for LZSM interference patterns of the current in open double QDs. The higher-order cumulants substantiate the conclusions drawn from studies of the Fano factor.

In this spirit, our approach enables the computation of the current noise for time-dependent transport beyond the second cumulant with a moderate effort. This may provide additional insight to the underlying mechanisms and a deeper understanding of the electron dynamics controlled by arbitrarily shaped driving.

While our aim was the development of a tool for conductors with an arbitrary time dependence, possible applications of our method extend beyond that scope. For example, it may be useful also for obtaining the transients of the FCS of time-independent conductors such as those studied in Refs. [191, 200, 201]. Moreover, it may be applied to non Markovian effects that can be captured by time-local master equations with time-dependent coefficients [202]. Finally, for periodic driving, our master equation hierarchy may serve as starting point for a Floquet treatment of the FCS (see chapter 6.2). This would extend the approach for the second cumulant derived from a precursor of the present method [203].

CHAPTER 6

TRANSPORT STATISTICS AND ITS INTERPLAY WITH TOPOLOGY

The final goal of this chapter is to analyze the interplay between topology and transport in time-dependent systems. As a model with nontrivial topology we employ a chain of dimers that exhibits a topological phase transition (TPT). We propose a transport blockade mechanism in quantum dot (QD) arrays and conducting molecules with the dimer geometry based on an interplay of Coulomb repulsion and the formation of topological edge states. Moreover, we propose the current cumulants measurement as a tool to identify the TPTs and analyze the effect of dissipation in the previous results.

In section 6.1 we explain the phenomenon of edge-state current blockade that occurs for transport through a dimerized conductor and we elaborate on the possible implementation with semiconductor QDs [**P.4**]. In section 6.2, we show that it is possible to induce this blockade via a driving protocol and we develop a formalism based on matrix-continued fractions to compute the full-counting statistics (FCS) of transport in a time-periodic system. It allows for the obtention of steady-state results avoiding numerical propagation [**P.7**]. Finally, our conclusions are detailed in section 6.3.

6.1 Edge-state blockade of transport in QD arrays

In this section we analyze the transport mechanisms through a system with exotic topological properties, the Su-Schrieffer-Heeger (SSH) model. For finite chains in the topologically nontrivial phase, a pair of exponentially decaying edge states emerges [136]. This chapter focusses on the impact of the edge states on the transport properties when the chain is in contact with an electron source and a drain. Derived from this analysis we propose an edge-state current blockade which relates to the transition from a topologically trivial to a nontrivial regime and we show that it is

most clearly visible in the shot noise.

6.1.1 Model and master equation

The ever smaller size of QDs implies small capacitances and accordingly large charging energies. Indeed in most recent realizations of coupled QDs, Coulomb repulsion represents the largest energy scale [48, 204] such that states with different electron number are energetically well separated. Then the QD array can be controlled by gate voltages and, despite a possible coupling to electron reservoirs, the dynamics is restricted to a few states with a specific electron number. This forms the basis for many realizations of spin or charge qubits.

We employ a model of spinless electrons on an array of length n described by the Hamiltonian $H_0 = H_{\mathrm{SSH}} + H_{\mathrm{int}}$. It contains nearest-neighbor hopping according to the SSH Hamiltonian [133]

$$H_{\mathrm{SSH}} = \sum_{j=1}^{n-1} \tau_j d_{j+1}^\dagger d_j + \mathrm{h.c.}, \tag{6.1}$$

with the alternating hopping amplitudes $\tau_j = \tau_0 + (-1)^j \delta\tau$ and the fermionic annihilation operators d_j. We keep τ_0 constant and use $\delta\tau$ as a control parameter. As explained in chapter 2, the SSH model has a TPT such that for $\delta\tau > 0$ two edge states emerge [see the energy spectrum in the inset of Fig. 6.2 (a)]. As we see below, they form a doublet that governs the transport properties. If the array consists of an odd number of sites, a monomer will remain forming an edge state. Thus, we witness a transition from a situation with an edge state at the right end of the chain ($\delta\tau < 0$) to one with an edge state at the left end ($\delta\tau > 0$) [103]. This transition, however, is not visible in the spectrum [see inset of Fig. 6.2 (b)].

Because of Coulomb repulsion between electrons, we assume an interaction Hamiltonian of the form $H_{\mathrm{int}} = \sum_{j>j'} U_{|j-j'|} N_j N_{j'}$, with the site occupations N_j and the interaction energies U_d, which decay with the distance $d = |j - j'|$ between the sites. Moreover, by working with spinless electrons, we have already ruled out double occupation of a single site. Physically, this is justified by the typically very strong on-site interaction U_0 in QDs.

To enable transport, we couple the ends of the array to biased leads acting as the electron source and drain with a voltage bias V (see Fig. 6.1). By tracing out the leads one can obtain a master equation for the reduced density operator of the central conductor. For low temperatures and in the limit $\tau_j \ll eV \ll U_d < U_0$, only single-electron states are energetically accessible and the electron transport becomes unidirectional. Moreover, the dot-lead tunneling rates become independent of the details of the array's level structure (infinite-bias limit). For a generic derivation of such master equation see Appendix B. Under these conditions the master equation assumes the convenient Lindblad form

$$\dot{\varrho} = \mathscr{L}\varrho \equiv -i[H_{\mathrm{SSH}}, \varrho] + \frac{\Gamma_S}{2}\mathscr{D}(d_1^\dagger)\varrho + \frac{\Gamma_D}{2}\mathscr{D}(d_n)\varrho, \tag{6.2}$$

with the Lindblad dissipator defined in Eq. (2.17) and the dot-lead tunneling rates $\Gamma_{S/D}$. The first term in $\mathscr{D}(x)$ corresponds to incoherent transitions induced by the operator $x = d_1^\dagger, d_n$, which

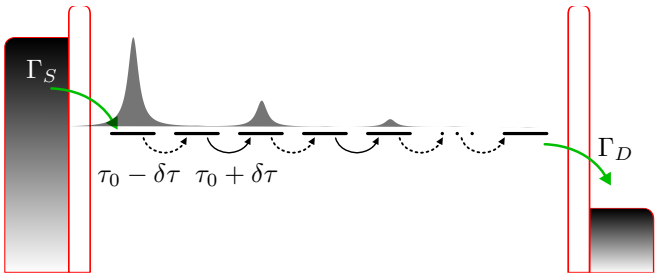

FIGURE 6.1. Sketch of a dimerized conductor with hopping amplitudes $\tau' = \tau_0 - \delta\tau$ and $\tau = \tau_0 + \delta\tau$, connected to an electron source (left) and a drain (right). At $\delta\tau = 0$, the conductor undergoes a TPT. The wave function depicts the stationary state in the topological regime. Electron trapping in the edge state at the source causes an edge-state current blockade.

in our case is the electron tunneling from the source to the array and from the array to the drain, respectively. Thus, the forward current superoperator is $J^+\varrho = \Gamma_S d_1^\dagger \varrho d_1$ (or equivalently $\Gamma_D d_n \varrho d_n^\dagger$). Note that neither the bias V nor the interaction constant U appear explicitly in Eq. (6.2). Let us therefore emphasize that our master equation holds only in the limit in which strong Coulomb repulsion inhibits the occupation with two or more electrons, i.e., it has to be evaluated in the subspace of zero or one electrons on the array. As a consequence, the dynamics is governed by the single-particle quantum mechanics induced by the SSH Hamiltonian, while the electron tunneling to and from the leads is affected by the interaction.

In the following, we show that the emergence of topological edge states is manifest in the shot noise properties as it is accompanied by a crossover from bunched electron transport to a Poissonian process. For both topological regions we capture the main physics in an analytically solvable model. The resulting analytical expressions for the Fano factor agree well with the numerical solution of a full quantum master equation.

6.1.2 Edge states and current fluctuations

As the Liouvillian in Eq. (6.2) is time-independent, the current follows directly from its kernel (zero-eigenvalue eigenvector) , i.e., $\mathscr{L}\varrho_\infty = 0$ and the expression $I = \mathrm{tr}\, J^+\varrho_\infty$. Interestingly, the result can be expressed analytically. For an even number of sites, we obtain

$$I_{\mathrm{even}} = \frac{\Gamma_D}{n + \frac{\Gamma_D}{\Gamma_S} + \frac{\Gamma_D^2}{4\tau^2}\left[n - 2 + \left(\frac{\tau}{\tau'}\right)^n\right]}, \tag{6.3}$$

while for odd n the current reads

$$I_{\mathrm{odd}} = \frac{\Gamma_D}{\frac{\Gamma_D}{\Gamma_S} + \frac{\Gamma_D^2(n-1)}{4\tau^2} + \left(\frac{\tau'}{\tau}\right)^2\left[n - 1 + \left(\frac{\tau}{\tau'}\right)^{n+1}\right]}. \tag{6.4}$$

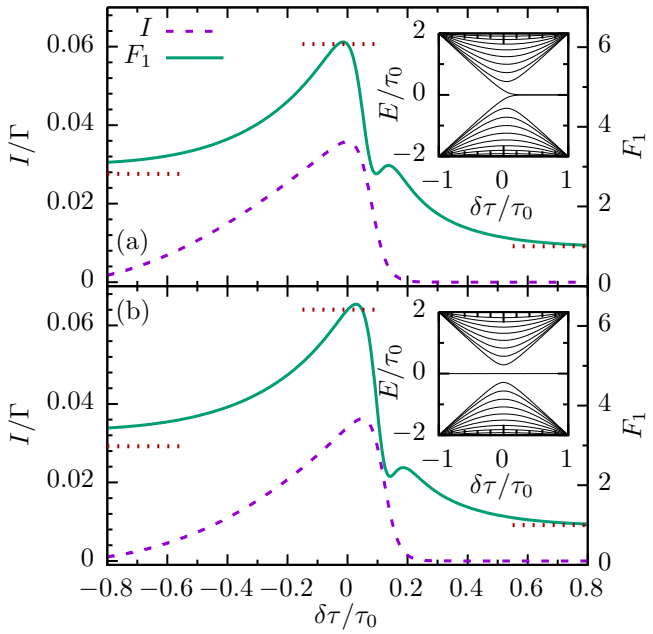

FIGURE 6.2. Current (dashed line) and Fano factor $F_1 = c_2/c_1$ (solid line) for an array of (a) $n = 20$ and (b) $n = 21$ sites as a function of the imbalance $\delta\tau/\tau_0$. The dotted horizontal lines mark the analytically obtained limits: $F_{\text{mono}}(n)$, $F_{\text{mono}}(n/2)$ and 1. Despite the different single-particle spectra (insets), the results for an even and odd number of sites are qualitatively the same. Dot-lead rates: $\Gamma \equiv \Gamma_D = \Gamma_S = 5\tau_0$.

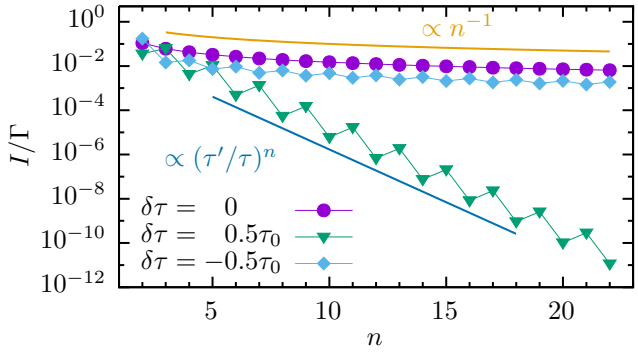

FIGURE 6.3. Stationary current as a function of the chain length for the values of $\delta\tau$ displayed. Dot-lead rates: $\Gamma \equiv \Gamma_D = \Gamma_S = 5\tau_0$.

Note that we have used the definitions $\tau' \equiv \tau_1 = \tau_0 - \delta\tau$ and $\tau \equiv \tau_2 = \tau_0 + \delta\tau$. Both expressions assume their maximum close to $\tau \approx \tau'$. For $\tau \gg \tau'$ the current decays $\propto (\tau'/\tau)^n$. In the opposite limit, $\tau \ll \tau'$, the decay is algebraic, $I \propto n^{-1}$ (see Fig. 6.3).

Computing the cumulants c_k for $k \geq 2$ requires not only the kernel of the Liouvillian, but also its pseudoinverse (see Eq. 5.19), which considerably complicates the analytical solution. In the

following, we find analytical solutions for a proper dimer chain, i.e., the case of an even number of sites, in some special limiting cases. The value of the current and the Fano factor across the TPT are shown in Fig. 6.2 (a). While in the monomer limit, $\delta\tau = 0$, the current assumes an appreciable value, it decays towards both the topologically trivial (left) and the nontrivial region (right). In the nontrivial region, the decay is faster despite the presence of interband states. The asymmetry is also found for the Fano factor which is super-Poissonian for $\delta\tau < 0$, while for $\delta\tau > 0$ it converges to the Poissonian value $F_1 = 1$. This indicates that the transport relates to topology. To reveal the physics behind this observation, we conjecture for each region a dominating mechanism and capture it by a rate equation that provides analytical simple expressions for the Fano factor.

i) For the monomer chain, i.e., at the transition point $\delta\tau = 0$ (for finite systems it is rather a crossover at $\delta\tau \approx \tau_0/n$ [136]), the eigenstates read

$$\phi_\ell = \sqrt{\frac{2}{n+1}}\,\sin\Big(\frac{\pi\ell j}{n+1}\Big), \tag{6.5}$$

where $\ell = 1,\ldots,n$, labels the solutions and j the site. We assume that each eigenstate forms a transport channel, where a strong Coulomb interaction leads to mutual exclusion of the channel occupation. A general model for transport via mutually exclusive channels ℓ that are weakly coupled to both leads with equal strength (γ_ℓ) is sketched in Fig. 6.4 (a). It corresponds to the rate equation

$$\frac{d}{dt}\begin{pmatrix} p_0 \\ p_1 \\ \vdots \\ p_n \end{pmatrix} = \begin{pmatrix} -\Gamma & \gamma_1 & \ldots & \gamma_n \\ \gamma_1 & -\gamma_1 & & 0 \\ \vdots & & \ddots & \vdots \\ \gamma_n & 0 & \ldots & -\gamma_n \end{pmatrix}\begin{pmatrix} p_0 \\ p_1 \\ \vdots \\ p_n \end{pmatrix}, \tag{6.6}$$

where normalization is ensured by $\Gamma = \sum_\ell \gamma_\ell$. The corresponding load and unload rates γ_ℓ are determined by the overlaps of the eigenstates ϕ_ℓ with the terminating sites, i.e., by $|\phi_\ell(1)|^2$ and $|\phi_\ell(n)|^2$. In a symmetric setup, $\Gamma_S = \Gamma_D \equiv \Gamma$, the rates at the source and at the drain are equal, which is reflected by the symmetry of the matrix in Eq. (6.6). They read

$$\gamma_\ell = \frac{2\Gamma}{n+1}\sin^2\Big(\frac{\pi\ell}{n+1}\Big). \tag{6.7}$$

States with $\ell \approx n/2$ are more strongly coupled to the leads than those with $\ell = 1$ or $\ell = n$ and, thus, most of the time, they support a regular current. However, whenever a weakly coupled state becomes populated, an electron will remain there for the rather long time γ_ℓ^{-1} and thereby interrupt the transport process. Accordingly, we expect bunching as is indicated by a large Fano factor. The stationary solution of Eq. (6.6) reads $(1,1,...,1)^T/(n+1)$ and thus $I = \Gamma/(n+1)$, which represents the weak coupling limit of Eq. (6.3). The second cumulant reads

$$c_2 = I + \frac{2\Gamma}{(n+1)^3}\Big[\frac{\Gamma}{\tilde{\Gamma}} - n(n+1)\Big], \tag{6.8}$$

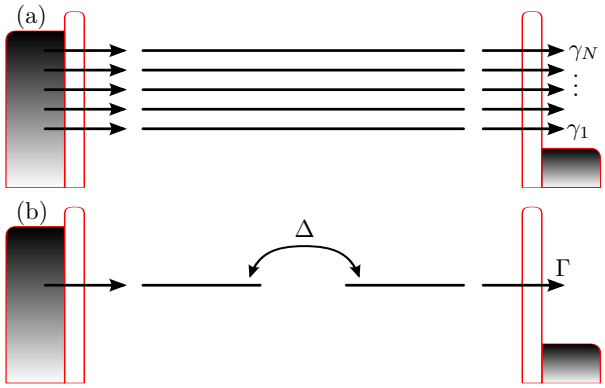

FIGURE 6.4. Sketch of the situations that we treat analytically with rate equations. (a) Mutually exclusive channels for the delocalized eigenstates of a monomer chain. The rates γ_ℓ reflect the overlap between the eigenstates and the first and the last site and obey $\sum_\ell \gamma_\ell = \Gamma$. (b) Two-state model for the topological edge states in the topological region. The inter-site hopping Δ is the exponentially small overlap between the edge states.

where $\tilde{\Gamma}^{-1} = \sum_\ell \gamma_\ell^{-1}$ is dominated by the weakly coupled states owing to their small γ_ℓ. Inserting the rates (Eq. 6.7) yields

$$\frac{c_2}{I} = \frac{n^2 - n + 3}{3(n+1)} \equiv F_{\text{mono}}(n) \tag{6.9}$$

and for the following cumulants

$$\frac{c_3}{I} = -\frac{n^2(n-7)}{30} + O(n); \tag{6.10}$$

$$\frac{c_4}{I} = \frac{n^4(2n-25)}{315} + O(n^3). \tag{6.11}$$

Note that the cumulant ratio grows with the length of the array as $c_{k+1}/c_k \propto n^2$.

ii) Deep in the trivial region $\delta\tau < 0$, the central system consists of weakly coupled dimers. Then we can consider each dimer as one site and, thus, expect the behavior of a monomer array with $n/2$ sites. Therefore, without an explicit calculation, we can conclude that the Fano factor is $F_1 = F_{\text{mono}}(n/2)$.

iii) In the topological region, $\delta\tau > 0$, the electrons mainly enter and leave the array via a zero energy topological edge state. Since all other states are energetically far off, they merely mediate long-range tunneling with an exponentially small effective matrix element Δ given by $\Delta \approx \tau_0 \exp(-n\delta\tau/\tau_0)$. This means that the situation can be captured by a two-level system model with tunneling amplitude Δ and connected to the source and the drain, as sketched in Fig. 6.4 (b). The corresponding master equation (in the basis

$\{|0\rangle\langle 0|, |L\rangle\langle L|, |R\rangle\langle R|, |L\rangle\langle R|, |R\rangle\langle L|\}$) is

$$\dot{\varrho} = \begin{pmatrix} -\Gamma_S & 0 & \Gamma_D & 0 & 0 \\ \Gamma_S & 0 & 0 & i\Delta/2 & -i\Delta/2 \\ 0 & 0 & -\Gamma_D & -i\Delta/2 & i\Delta/2 \\ 0 & i\Delta/2 & -i\Delta/2 & -\Gamma_D/2 & 0 \\ 0 & -i\Delta/2 & i\Delta/2 & 0 & -\Gamma_D/2 \end{pmatrix} \varrho. \tag{6.12}$$

In the symmetric case $\Gamma_D = \Gamma_S \equiv \Gamma$, the current and the Fano factor can be obtained analytically as

$$I = \frac{\Gamma\Delta^2}{\Gamma^2 + 3\Delta^2}; \tag{6.13}$$

$$F_1 = \frac{\Gamma^4 + 5\Delta^4 - 2\Gamma^2\Delta^2}{\left(\Gamma^2 + 3\Delta^2\right)^2}. \tag{6.14}$$

For a sufficiently long array, $\Delta \ll \Gamma$, the bottleneck of the transport is the tunneling between edge states. In this limit let us expand Eqs. (6.13) and (6.14) to second order in Δ to obtain

$$I = \frac{\Delta^2}{\Gamma}; \tag{6.15}$$

$$F_1 = 1 - 8\frac{\Delta^2}{\Gamma^2}. \tag{6.16}$$

To summarize, the transport consists of uncorrelated events [205], i.e., it is a Poissonian process with the characteristic Fano factor $F_1 = 1$. Moreover, we one can perform the iteration scheme for the next cumulants within the same accuracy which provides the expressions

$$\frac{c_3}{I} = 1 - \frac{24\Delta^2}{\Gamma^2}; \tag{6.17}$$

$$\frac{c_4}{I} = 1 - \frac{56\Delta^2}{\Gamma^2}. \tag{6.18}$$

Thus, to lowest order in Δ, all cumulants equal the current, which indicates that the transport process is essentially Poissonian.

The Fano factor of the full numerical calculation agrees rather well with the limits obtained analytically [see the horizontal lines in Fig. 6.2 (a)]. This provides evidence that the transport process in each region indeed follows the scenario sketched above.

Since the separation of the Fano factors in the different regions grows with the length of the array, one may aim at an experimental realization with as many sites as possible. This, however, will raise the experimental difficulties drastically. Moreover, beyond a certain system size, the limit of a strong Coulomb blockade may no longer be realistic. Thus the length dependence of the Fano factors deserves a closer inspection. The data shown in Fig. 6.5 (a) confirm our analytical results even down to rather small lengths. For an intermediate length $n \approx 10$, the Fano

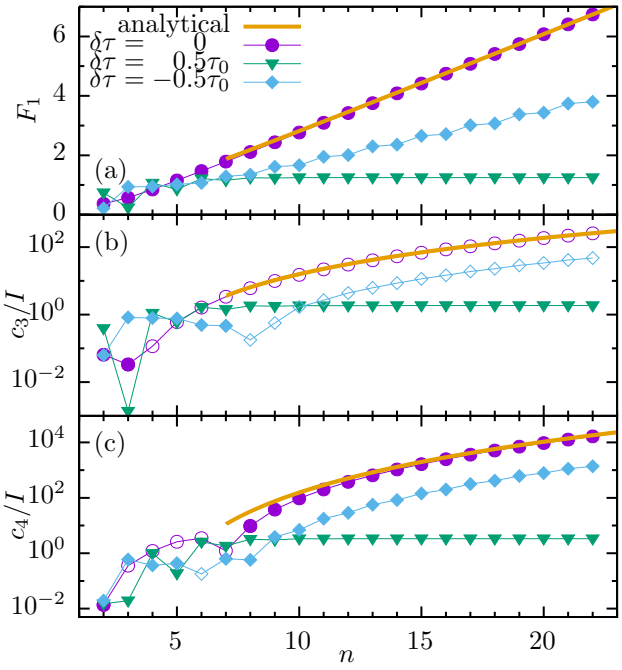

FIGURE 6.5. (a) Fano factor, (b) third cumulant and (c) fourth cumulant as a function of the chain length for various $\delta\tau$. Solid symbols mark positive values and stroked symbols correspond to negative values. Dot-lead rates: $\Gamma \equiv \Gamma_D = \Gamma_S = 5\tau_0$.

factors in the three regimes are already significantly different from each other. In particular, the differences are larger than the demonstrated resolution of mesoscopic noise measurements [206]. The data for cumulants of higher order presented in Figs. 6.5 (b) and (c) support our conjecture of Poissonian transport in the topological phase.

A further important observation is that the behavior of the shot noise for chains with an odd number of sites interpolates the behavior of dimer chains. In particular, we find that the current and the Fano factor as a function of $\delta\tau$ indeed are qualitatively the same as for even n [see Fig. 6.2 (b)]. For odd n, irrespective of the sign of $\delta\tau$, there always exists one edge state which has zero energy [see the spectrum shown in the inset of Fig. 6.2 (b)]. The emergence of the edge state at one specific end of the chain can be explained in terms of the bulk-edge correspondence as follows. Let us consider a not too short chain with even n and $\delta\tau > 0$, such that the tunnel splitting Δ between the edge states is much smaller than the lead coupling Γ. Then decoherence will turn a possible superposition of both edge states into a mixture such that the edge state at the source will not be influenced by its counterpart at the drain. Then removing the last site of the chain will not have a major effect on the edge-state formation at the source. In this sense, also finite chains with odd n still exhibit some footprint of the TPT that is found for infinite or semi-infinite dimer chains.

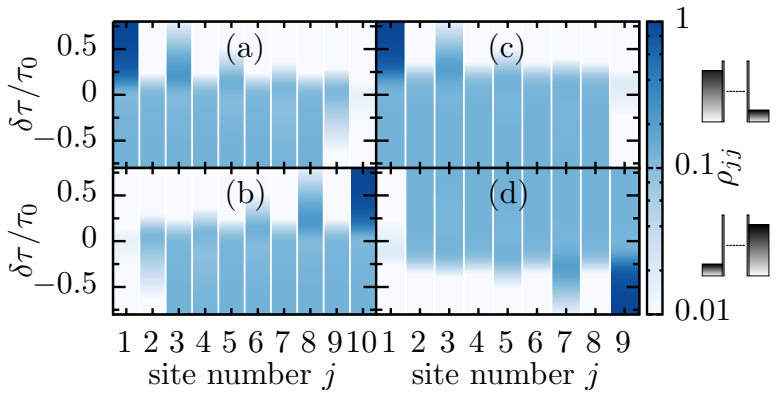

FIGURE 6.6. Population of the sites in the stationary state for the array lengths (a),(b) $n = 10$ and (c),(d) $n = 9$ and the dot-lead rates $\Gamma_D = \Gamma_S = 5\tau_0$. The data in the lower row are with the source and drain interchanged, as indicated by the sketches at the right margin. They reveal that a current blockade emerges when the edge state at the source is strongly populated (dark blue areas). Comparing the upper row with the lower row highlights the reflection symmetry for even n, while for odd n the spatial reflection corresponds to inverting the sign of $\delta\tau$.

6.1.3 Edge-state blockade

The common feature for even and for odd n is that only for $\delta\tau > 0$, does the chain possess an edge state at the electron source. The relevance of its location at the source is visible in the behavior under inverting the applied bias: For even n, the chain is symmetric, so that only the direction of the current changes. Therefore, the Fano factor in Fig. 6.2 (a) will remain the same. For odd n, by contrast, the inverted bias leads to a situation with an edge state at the drain but none at the source. Thus, bias inversion is equivalent to changing the sign of $\delta\tau$, which for odd n moves the edge state from one end of the chain to the other. Therefore, upon bias inversion, F_1 in Fig. 6.2 (b) becomes reflected at the y axis (not shown).

To underline the importance of the edge state and to develop a physical picture for the blockade, we consider the population of the sites in the stationary state of the open system (see Fig. 6.6). For an even number of sites (Figs. 6.6 (a) and (b), where the latter is computed with source and drain interchanged), in the topological phase ($\delta\tau > 0$) the edge state at the source is predominantly populated. This is consistent with the scenario drawn above in which the transport occurs via weak long-range tunneling. Consequently, an electron becomes trapped in the edge state localized at the source, while once it is at the opposite side of the array, it leaves quickly to the drain.

For an odd number of sites, the behavior is similar. Outside the crossover region $|\delta\tau| \gg \tau_0$, a single edge state always exists. For $\delta\tau > 0$, it is localized at site 1 and causes a current blockade [see Fig. 6.2 (b)]. By contrast, for $\delta\tau < 0$, despite the emergence of an edge state at site n, an appreciable current flows. To resolve this seeming contradiction, let us focus on an array with odd

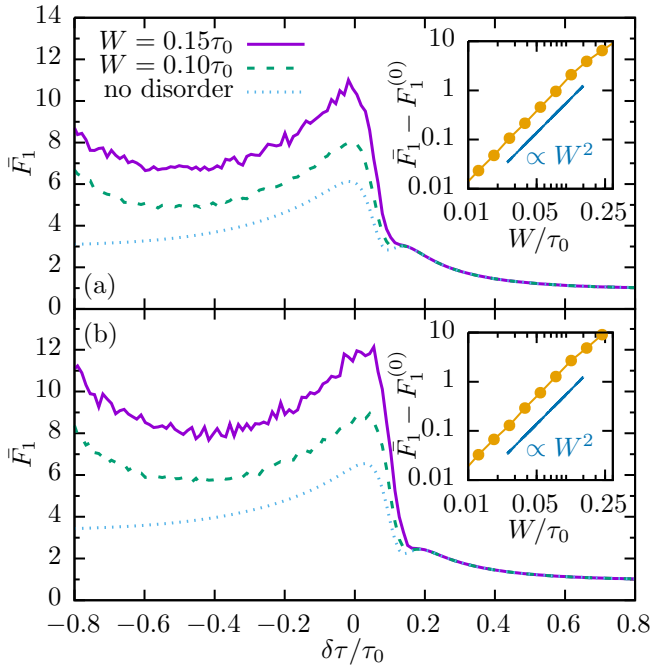

FIGURE 6.7. Fano factor in the presence of disorder with strength W for a chain of lengths (a) $n = 20$ and (b) $n = 21$ with the parameters used in Fig. 6.2. Insets: Deviation of the averaged Fano factor from its value in the absence of disorder for $\delta\tau = -0.5\tau_0$.

n and $\delta\tau < 0$ such that an edge state at the drain is formed. Nevertheless, a small overlap of the bulk states with the last site opens a way to circumvent the edge state. Moreover, in rare cases in which an electron reaches the edge state, it will proceed quickly to the drain, consequently, no relevant blockade occurs. For $\delta\tau > 0$, the edge state is located at the source and is mostly occupied [see Fig. 6.6 (c)]. Then, bypassing site 1 is in principle possible, but would require double occupation of the chain. This, however, is inhibited by Coulomb repulsion so that transport is interrupted until the electron in the edge state is released. This reveals that the blockade results from an interplay of edge-state formation at the source and strong Coulomb repulsion. The population for interchanged source and drain [Fig. 6.6 (d)] confirms that the edge-state formation at the source is also decisive for trapping an electron when n is odd.

6.1.4 Effect of disorder

The formation of edge states with exponentially small splitting is protected by sub-lattice symmetry present in our idealized array Hamiltonian H_{SSH}. In a realistic experiment, however, it may be quite difficult to tune the system sufficiently well. To investigate the influence of imperfections,

we consider disorder and add random on-site energies,

$$H_{\mathrm{SSH}} \to H_{\mathrm{SSH}} + W \sum_j \xi_j d_j^\dagger d_j, \tag{6.19}$$

where W is the disorder strength and ξ_j is taken from a normalized box distribution with $-1/2 \le \xi_j \le 1/2$.

Figure 6.7 shows the resulting Fano factor, now defined as $\bar{c}_2/\bar{I}$, i.e., the ratio of the averages. Comparing Figs. 6.7(a) and (b), the behavior for an even and an odd number of sites again turns out to be practically the same. For $\delta\tau \lesssim 0$, we find that the Fano factor grows with increasing disorder. The enhancement is roughly $\propto W^2$, as can be appreciated in the inset. Notice that for larger values of W and much longer arrays, Anderson localization [207] becomes relevant and may change this behavior. For $\delta\tau > 0$, by contrast, disorder has almost no influence on the Fano factor. This finding is consistent with the physical picture drawn above: The transport occurs via the two states localized at the ends of the array, while the other states are off-resonant and not populated. Since disorder even supports localization, the Poissonian behavior remains unaffected.

6.1.5 Possible experimental realization

The high tunability of the various types of semiconductor QDs makes them natural candidates for the implementation of blockade effects in mesoscopic transport. Recently, two parallel QD arrays, each with seven QDs, have been demonstrated [55]. Also an array of 9 QDs has been realized [56]. In such systems, the charging and the tunnel matrix elements are highly controllable by gate voltages. Thus it should be possible to tune them such that they meet the requirement of an interaction much larger than the tunneling, at least in not too long arrays.

Molecular wires represent a realistic alternative, in particular, since they are rather small and thus possess huge charging energies. Between experimental runs, they can be modified by atomic force microscopy techniques [208]. Since this may also affect wire-lead tunneling rates, the visibility of the blockade in the Fano factor is a virtue since this quantity, in contrast to the current, depends only weakly on the wire-lead coupling.

In both implementations, experimental evidence for edge-state blockade will be facilitated by the external tunability of the inter-dot tunneling. A possible way to achieve this is driving the conductor by an electric dipole field. Then for not too small frequencies, the driving essentially renormalizes the inter-dot tunnel coupling [33–35, 209] and, thus, allows the emulation of a dimer chain with highly tunable tunneling. In the present system, a recent work investigates how to change the topology of the chain of dimers by driving fields [46]. In the corresponding transport setting, i.e., in the presence of electron source and drain, one expects a corresponding current suppression [78, 79] which has been measured in double QDs [82, 83]. Moreover, the driving may have significant impact on the shot noise [171]. In the following section we apply the findings of chapter 5 about the computation of the FCS of time-dependent conductors to explore the possibility for edge-state blockade in driven QD arrays.

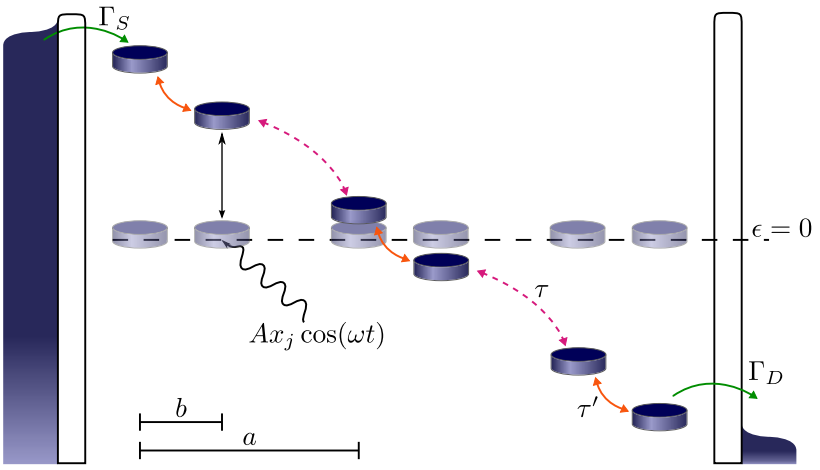

FIGURE 6.8. Sketch of a driven dimerized conductor with hopping amplitudes $\tau' = \tau_0 - \delta\tau$ and $\tau = \tau_0 + \delta\tau$, connected to an electron source (left) and a drain (right) with rate $\Gamma_{S,D}$. The applied external electric field generates an oscillation of the onsite energies with frequency ω which depends on the positions of the QDs, x_j, therefore the inter- and intra-dimer distances a and b, respectively, become relevant.

6.2 Floquet engineering of transport in QD arrays

In this section, we show the existence of edge-state blockade in periodically driven QD arrays such as those sketched in Fig. 6.8. It is based on the recent finding that the topological properties of periodically driven dimer chains can be controlled via the amplitude of an electric field [46, 210, 211]. A method to compute the shot noise, which according to the previous section is an indicator of the TPT, in this type of time-dependent conductors was presented in chapter 5. But it implies the numerical evaluation of a series of equations for sufficient time such that the stationary state is reached. For an efficient treatment, we extend here a previously developed matrix-continued fraction method [212] to the computation of shot noise.

First, we introduce our model and a master equation description, as well as the matrix-continued fraction method for the computation of the current and the zero-frequency noise of time-dependent transport problems. Then, the main features of the current and shot noise are presented, while the last part is devoted to the impact of dissipation.

6.2.1 Model and master equation

We consider an array of QDs coupled to a time-dependent electric dipole field such that the onsite energies oscillate in time with a position-dependent amplitude, see Fig. 6.1. The static part is given by the SSH Hamiltonian in Eq. (6.1). We will focus on a dimer chain with an even number of sites, n, and the site j located at position x_j. The electric field couples via the dipole operators

of the chain such that the Hamiltonian reads

$$H(t) = H_{\mathrm{SSH}} + A\sum_{j=1}^{n} x_j d_j^\dagger d_j \cos(\omega t). \tag{6.20}$$

For convenience, we choose the origin in the middle of the chain such that

$$x_j = \begin{cases} -L/2 + (j-1)a/2 & \text{j } odd \\ -L/2 + (j-2)a/2 + b & \text{j } even \end{cases}, \tag{6.21}$$

with the distances between two neighboring sites b and $a-b$, alternatively, which implies a unit cell of length a and a chain length $L = (n-2)a/2 + b$. The driving is determined by its frequency ω and amplitude A.

The topological properties of the SSH model stem from a sub-lattice (or chiral) symmetry C with $CH_{\mathrm{SSH}}C = -H_{\mathrm{SSH}}$. The time-dependent part of the Hamiltonian (6.20) is invariant under transformation with C. However, the sinusoidal driving allows us to obtain a minus sign via shifting the time by half a driving period, $t \to t + T/2$, where $T = 2\pi/\omega$ is the period of the driving. Formally, this can be expressed as

$$CH(t)C = -H(t + T/2). \tag{6.22}$$

We refer to this symmetry relation as "generalized chirality", owing to its resemblance to the generalized parity present in symmetric bistable potentials driven by a dipole force [33]. A consequence of the generalized chirality is that the time evolution operator of the chain, $U(t,t')$, obeys the relation

$$U(t_0 + T, t_0 + T/2) = CU^{-1}(t_0 + T/2, t_0)C. \tag{6.23}$$

Thus, the one-period time evolution operator can be split into two symmetry-related parts, a fact that has been identified as a condition for nontrivial topological properties of a periodically driven system [213].

Analogously to the previous section, transport is enabled by coupling the first and the last site to an electron source and drain, respectively. In the limit in which the applied voltage (bias) is much larger than the hopping amplitudes τ_j, but still considerably smaller than the Coulomb repulsion of the electrons on the array, the Lindblad master equation reads

$$\dot{\varrho} = \mathscr{L}\varrho = -i[H(t), \varrho] + \frac{\Gamma_S}{2}\mathscr{D}(d_1^\dagger)\varrho + \frac{\Gamma_D}{2}\mathscr{D}(d_n)\varrho, \tag{6.24}$$

with the Lindblad dissipator in Eq. (2.17) and the dot-lead tunneling rates $\Gamma_{S,D}$.

A natural way to compute the shot noise is the numerical integration of the system of Eqs. (5.14) and (5.15). For convenience, we write this in block matrix form as

$$\begin{pmatrix} \dot{\varrho} \\ \dot{X}_1 \end{pmatrix} = \begin{pmatrix} \mathscr{L}(t) & 0 \\ J^+ - I(t) & \mathscr{L}(t) \end{pmatrix} \begin{pmatrix} \varrho \\ X_1 \end{pmatrix} \equiv M(t)\mathbf{b} \tag{6.25}$$

with the shorthand notation $\mathbf{b} = (\varrho, X_1)^T$ and the current $I(t) = \mathrm{tr}\, J^+ \varrho$.

While being very flexible, such numerical propagation schemes often lack efficiency. Therefore we aim at implementing a matrix-continued fraction method [214] which in the context of mesoscopic transport has been employed recently for the computation of time-averaged currents [212]. Here we extend this scheme to the computation of the zero-frequency noise.

To derive a matrix-continued fraction scheme, we have to bring Eq. (6.25) into the form of a tridiagonal recurrence relation [214]. In the present case, this is hindered by the fact that $M(t)$ depends on the time-dependent current $I(t)$ which may contain higher-order harmonics. Here however, we find that reliable results for the noise can still be obtained when $I(t)$ is replaced by its time average during a period. We test this assumption in Sec. 6.2.3. Since now the remaining time dependence in $M(t)$ stems exclusively from the Liouvillian of the sinusoidal driving in the Hamiltonian (6.20), the Fourier decomposition of the terms in Eq. (6.25) reads

$$M(t) = M_0 + M_+ e^{i\omega t} + M_- e^{-i\omega t}, \tag{6.26}$$

$$\mathbf{b}(t) = \sum_{n=-\infty}^{\infty} e^{in\omega t} \mathbf{b}_n. \tag{6.27}$$

By inserting this decomposition into Eq. (6.25) we obtain the tridiagonal recurrence relation

$$M_+ \mathbf{b}_{n-1} + (M_0 - in\omega)\mathbf{b}_n + M_- \mathbf{b}_{n+1} = 0\,. \tag{6.28}$$

Our interest lies in the time-average of $\mathbf{b}(t)$, i.e., in the Fourier component $\mathbf{b}_0$. To this end, we define the transfer matrices S_k and R_k via the ansatz

$$\mathbf{b}_n = \begin{cases} R_n \mathbf{b}_{n+1} & \text{for n<0,} \\ S_n \mathbf{b}_{n-1} & \text{for n>0.} \end{cases} \tag{6.29}$$

Consistency with Eq. (6.28) is ensured by the recurrence relations

$$S_n = -[M_0 - in\omega + M_- S_{n+1}]^{-1} M_+, \tag{6.30}$$

$$R_n = -[M_0 - in\omega + M_+ R_{n-1}]^{-1} M_-, \tag{6.31}$$

together with

$$(M_0 + M_+ R_{-1} + M_- S_1)\mathbf{b}_0 = 0. \tag{6.32}$$

For practical purposes, we have to truncate the Fourier components of $\mathbf{b}(t)$ assuming $\mathbf{b}_n = 0$ for $|n| > n_0$ which holds for $S_{n_0+1} = R_{-(n_0+1)} = 0$. With the latter condition we compute R_{-1} and S_1 by iterating Eqs. (6.30) and (6.31) which finally provides an explicit expression for Eq. (6.32). In a last step we solve this homogeneous equation under the trace conditions $\mathrm{tr}\,\varrho_0 = 1$ and $\mathrm{tr}\, X_{1,0} = 0$.

6.2.2 Transport in the high-frequency regime

The main energy scale of the static Hamiltonian H_{SSH} is the bandwidth τ_0. If it is much smaller than the energy quanta of the driving field, ω, one may employ a high-frequency approximation to derive an effective time-independent Hamiltonian that captures the stroboscopic long-time-dynamics of the driven system. This typically results in an effective Hamiltonian with parameters renormalized by Bessel functions, as occurred in chapter 3. In this way, the driving offers a possibility for tuning system parameters. A classic example is the coherent destruction of tunneling (CDT) in bistable potentials [33, 34] and superlattices [209, 215] by the purely coherent influence of a driving field.

In a dimer chain driven by an external electric field, the intra- and inter-dimer spacings (a and b) become relevant because they determine the dipole moments and, thus, appear in the renormalization of the inter-dimer hopping τ and the intra-dimer hopping τ' which in our case read

$$\tau'_{\mathrm{eff}} = J_0\left(\frac{Ab}{\omega}\right)(\tau_0 - \delta\tau), \tag{6.33}$$

$$\tau_{\mathrm{eff}} = J_0\left(\frac{A(a-b)}{\omega}\right)(\tau_0 + \delta\tau), \tag{6.34}$$

where J_0 is the zeroth-order Bessel function of the first kind. For details of the calculation, see Ref. [46]. With these effective hopping amplitudes, one can draw conclusions about the topological properties of the chain by a comparison with results for the time-independent SSH model [107, 136]. The main finding is a trivial topology for $\tau'_{\mathrm{eff}} > \tau_{\mathrm{eff}}$, while for $\tau'_{\mathrm{eff}} < \tau_{\mathrm{eff}}$ it becomes nontrivial with a winding number $W = 1$ [46, 210]. Similar influence of radiation on topology occurs also in higher dimensions [43, 47, 216]. The data in Fig. 6.9 confirm this expectation and reveal a particular dependence on topology:

i) The hopping amplitudes (6.33) and (6.34) possess an interesting duality. By the replacement $(\delta\tau, b) \to (-\delta\tau, a-b)$, they are interchanged. Then the topological properties are interchanged as well, while the bulk spectra remain the same. This motivated a comparison of data for two parameter sets with such relation (left and right column of Fig. 6.9, respectively). The complementarity of the two cases is evident from the quasienergy spectra shown in Figs. 6.9 (a) and (b). Both choices lead to the same bulk properties, while the topological (with zero-energy states) and the trivial (without zero-energy states) regions are interchanged.

ii) If the driving amplitude A is such that one of the Bessel functions in Eqs. (6.33) and (6.34) vanishes, the way from the electron source to the drain is practically interrupted, which significantly reduces the current. Figures 6.9 (c) and (d) show a remarkable dependence of the current suppression on the topology. In the trivial region, the current is extensively reduced only when the effective inter-dimer hopping vanishes, i.e., for $\tau_{\mathrm{eff}} \ll \tau_0$ [$A \approx 9\omega$

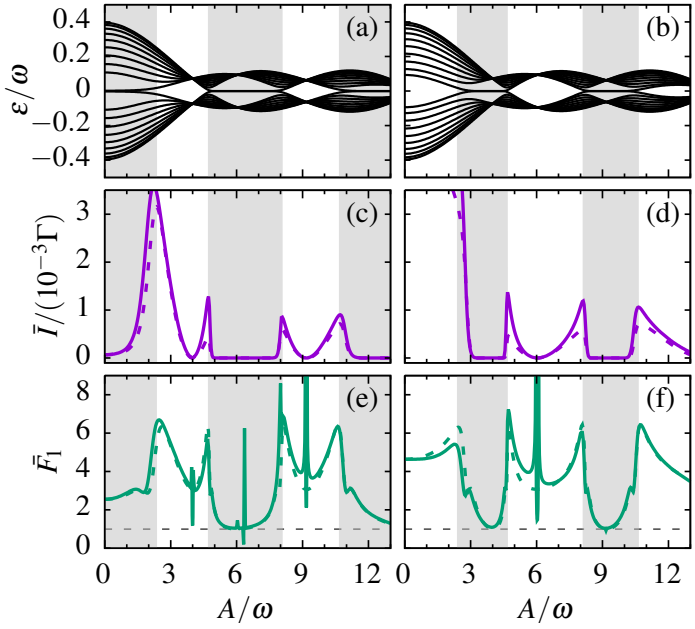

FIGURE 6.9. (a,b) Quasienergy spectrum as a function of the driving amplitude A for (a) $\delta\tau = 0.2\tau_0$, $b = 0.4a$ and (b) $\delta\tau = -0.2\tau_0$, $b = 0.6a$ for a chain with $n = 20$ sites. The parameters are chosen such that the bulk spectra in the thermodynamic limit are identical, while the topological properties depend on the sign of $\delta\tau$. Accordingly, we find edge states at zero quasienergies in the regions marked by a grey background. (c,d) Time-averaged current. The dashed lines correspond to the high-frequency approximation result. (e,f) Time-averaged Fano factor. Other parameters: $\omega = 5\tau_0$, $\Gamma \equiv \Gamma_S = \Gamma_D = 5\tau_0$.

in Fig. 6.9 (c) and $A \approx 6\omega$ in Fig. 6.9 (d)]. Close to the suppression, the current grows quadratically, such as for a driven double QD [79]. By contrast, the current almost vanishes in the whole topological region, i.e., whenever the weaker condition $\tau'_{\text{eff}} < \tau_{\text{eff}}$ is fulfilled. Therefore, we can conclude that the physical origin of this current suppression is not a completely vanishing effective hopping amplitude, but must be related to topology and the corresponding edge states formed at the source and at the drain. As these edge states are exponentially weakly connected and they are energetically well separated from the bulk states, they may trap electrons and thereby interrupt the transport process such that one observes edge-state blockade. As compared to its counterpart in time-independent chains (see section 6.1), this blockade is characterized by a broad region with vanishing current, while the CDT-like suppression of current in the trivial region has a parabolic shape.

iii) Figures 6.9 (e) and 6.9 (f) depict the shot noise for the driven case characterized by the time-averaged Fano factor $\bar{F}_1 = \bar{c}_2/\bar{I}$. It reveals a smeared crossover between Poissonian noise and super-Poissonian values up to $\bar{F}_1 \approx 8$. Therefore it would be possible to identify edge-state blockade by its characteristic shot noise properties.

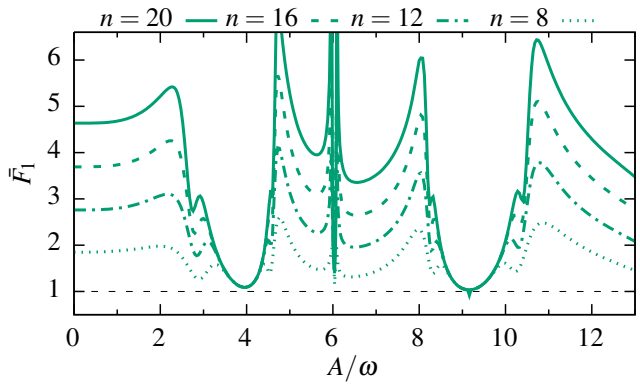

FIGURE 6.10. Time-averaged Fano factor as a function of the driving amplitude A for $\delta\tau = -0.2\tau_0$, $b = 0.6a$ for chains of various lengths. Other parameters: $\omega = 5\tau_0$, $\Gamma \equiv \Gamma_S = \Gamma_D = 5\tau_0$.

The difficulty of performing an experiment on a chain with many sites raises the question about the necessary length to observe the edge-state blockade. Thus we have calculated the Fano factor corresponding to the parameters in Fig. 6.9 (f) for chains of different length. An advantage of using the external field to manipulate the topological phase is that the ideal Poissonian Fano factor $F_1 \approx 1$ is always reached for a certain point in the blockade region, as shown in Fig. 6.10. This finding is in contrast to the static case, where $F_1 \approx 1$ was found only in the limit of very long chains. However, Fig. 6.10 also shows that for a short chain the Fano factor in the CDT point also approaches unity, which does not allow distinguishing the CDT effect from the edge-state blockade.

While in contrast to the static case, here the shape of the current suppression may be sufficient to identify edge-state blockade, it will turn out that the Fano factor exhibits clearer fingerprints of the topological phase diagram. In Fig. 6.11 (a) we show the topological phase diagram in terms of the winding number as a function of the amplitude of the driving and the ratio between intra- and inter-dimer distances. The corresponding plot for the current, shown in Fig. 6.11 (b), exhibits a richer structure stemming from the additional current suppressions in the trivial regions. Therefore the behavior of the current alone does not reflect the topological phase. The Fano factor, shown in Fig. 6.11 (c), in contrast, provides clearer evidence, because $\bar{F}_1 \approx 1$ is found exclusively for nontrivial topology (black regions). We also find some additional structure in the trivial region as narrow lines at CDT-like zeros of the current. There, the Fano factor assumes even larger values which correspond to the sharp peaks in Figs. 6.9 (e) and (f). Thus, shot noise measurements represent an alternative to the direct observation of the winding number as performed in Ref. [135].

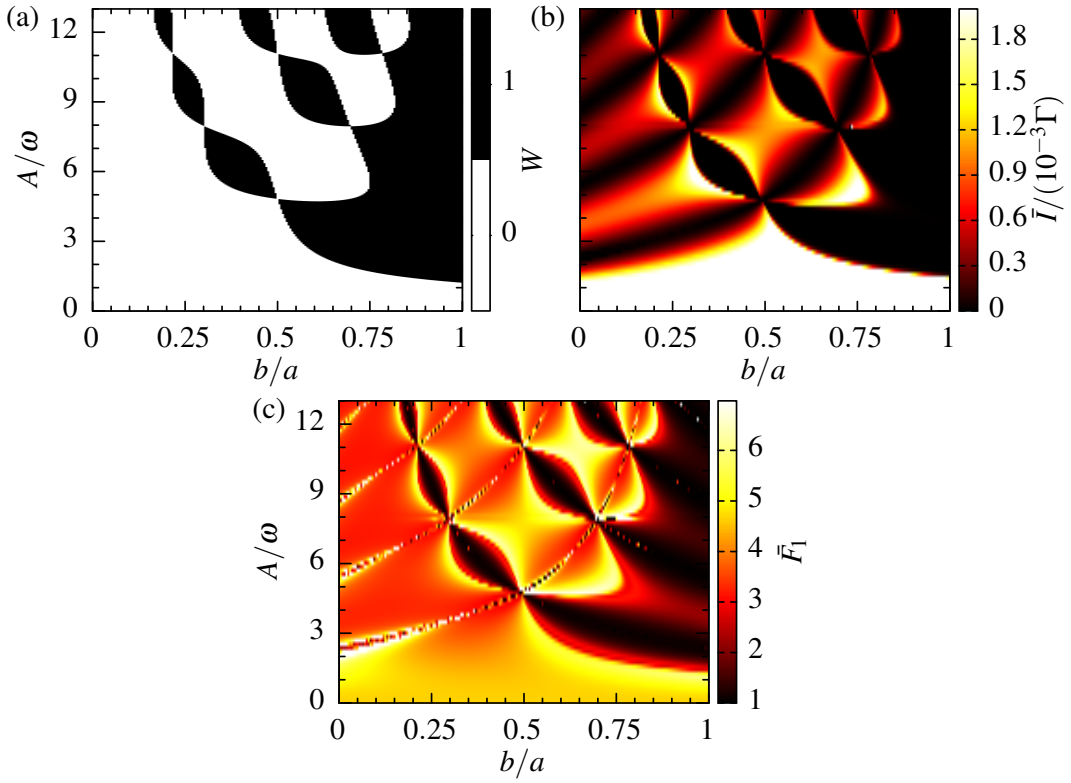

FIGURE 6.11. (a) Winding number as a function of the intra-dimer distance b and the driving amplitude A. Dark regions ($W = 1$) refer to a nontrivial topology, cf. the grey background in Fig. 6.9. All other parameters are as in the right column of Fig. 6.9. (b) Corresponding time-averaged current and (c) Fano factor.

6.2.3 Validity of the method

The matrix-continued fraction method for the computation of the average current significantly reduces the computational effort as compared to the numerical propagation of the equations of motion (6.25), at least for large and intermediate driving frequencies and for parameters that lead to current blockade. To derive the former method, however, we had to assume that in Eq. (6.25), the time-dependent current $I(t)$ can be replaced by its time average. Here we test this assumption and show in Figs. 6.12 (a) and (b) the time dependence of $I(t)$ in the steady-state limit. For typical driving parameters, we find that it possesses an appreciable time-dependent component even though it is always smaller than the time average. In Fig. 6.12 (c) we compare the results for the Fano factor computed with matrix-continued fractions and by numerical propagation. We find that, despite the neglected time dependence, both results agree rather well. This justifies the approximation made.

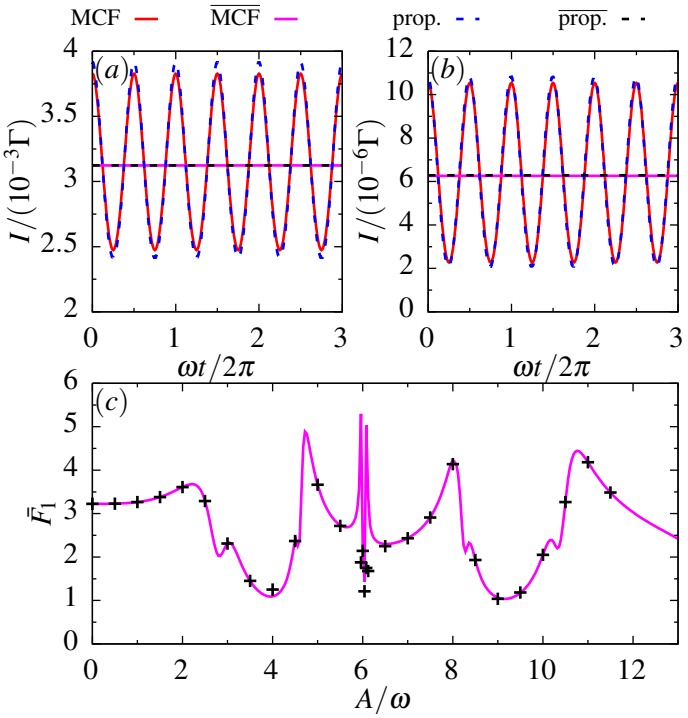

FIGURE 6.12. Time dependence of the current expectation value in the steady state for a chain with length $n = 14$, (a) $\delta\tau = 0.2\tau_0$, $b = 0.4a$ and (b) $\delta\tau = -0.2\tau_0$, $b = 0.6a$ obtained by means of propagation (prop.) and matrix-continued fractions (MCF). The respective average values are marked by horizontal lines. (c) Fano factor computed with matrix-continued fractions (solid line) compared to the result obtained by numerical propagation (dots) as a function of the amplitude of the driving for $\delta\tau = -0.2\tau_0$ and $b = 0.6a$. Other parameters: $\omega = 5\tau_0$, $\Gamma \equiv \Gamma_S = \Gamma_D = 5\tau_0$.

6.2.4 Quantum dissipation

In section 6.1, we have shown that for the static SSH model, the fingerprints of the topological properties in the Fano factor are fairly insensitive to weak static disorder. In the nontrivial region the edge-state formation is even supported by disorder and, thus, the Fano factor remains at the Poisson level. In the trivial region we witnessed a slightly increased Fano factor.

Here we investigate the impact of a dynamic disorder stemming from the interaction of each site with a respective heat bath via the population operators $d_j^\dagger d_j$. For weak coupling, we use a simple description with a Lindblad operator [184] with equal coupling strengths and modify the Liouvillian according to

$$\mathscr{L} \to \mathscr{L} + \gamma \sum_j \mathscr{D}(d_j^\dagger d_j). \tag{6.35}$$

Figs. 6.13 (a) and (b) depict how the current changes upon increasing the dissipation strength for two selected driving amplitudes. We focus on the two complementary parameter sets used in Fig. 6.9 and select two particular driving amplitudes, one corresponding to trivial topology

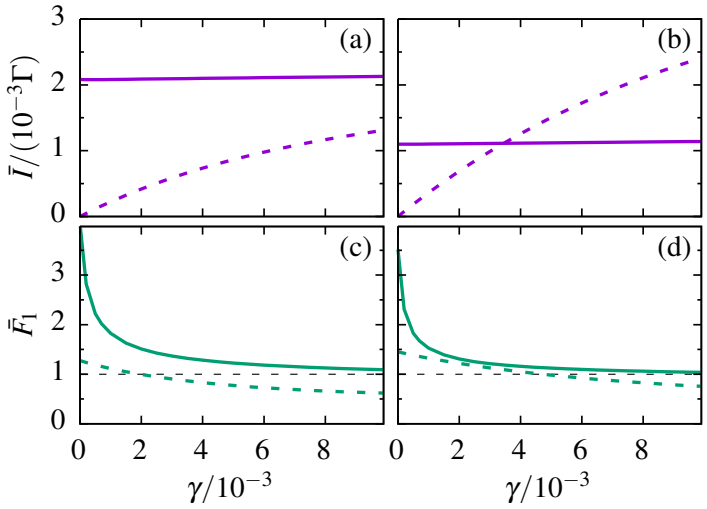

FIGURE 6.13. Influence of quantum dissipation via (a,b) time-averaged currents and (c,d) corresponding Fano factors as a function of the dissipation rate γ for the amplitudes $A = 3.5\omega$ and $A = 7\omega$. The left and right column corresponds to the respective column of Fig. 6.9, i.e., (a,c) $\delta\tau = 0.2\tau_0$ and $b = 0.4a$, while (b) and (d) correspond to the complementary case $\delta\tau = -0.2\tau_0$ and $b = 0.6a$. Solid lines mark topologically trivial cases, while dashed lines correspond to nontrivial topology. Other parameters: $\omega = 5\tau_0$, $\Gamma \equiv \Gamma_S = \Gamma_D = 5\tau_0$.

(solid lines), the other to nontrivial topology (dashed lines). For trivial topology, the current is rather insensitive to weak dissipation. The main reason for this is that in the trivial region, the transport occurs via the delocalized eigenstates of the chain while coherences between these states play a minor role. Accordingly, decoherence is not a relevant issue. For nontrivial topology, in contrast, the current grows with an increasing dissipation strength γ. A physical picture for this behavior is the direct transport between edge states. Since the splitting of the edge state doublet is exponentially small, the current is rather weak. Then dissipative transitions turn out to be rather beneficial for the electron transport.

In contrast to the current, shot noise is affected by dissipation in the same way in both phases, as can be appreciated in Figs. 6.13 (c) and (d). For both trivial and nontrivial topology, dissipation reduces the Fano factor which soon assumes values close to the Poissonian $F_1 = 1$. This means that measuring the topological phase diagram via the Fano factor (see Fig. 6.11) will require samples with very good coherence properties such that $\gamma \lesssim 10^{-3}\tau_0$, a value that seems feasible with present QD technology [83].

6.2.5 Experimental realization

For an experimental realization of our proposal, one may employ lateral QDs. At least for double QDs with a periodically driven gating of a few GHz and amplitudes $A \lesssim 10\omega$, intra-dot excitations turned out to play a minor role [83]. While the nearest neighbor interaction of such systems is

typically much larger than the inter-dot tunneling [83, 204], the magnitude of the long-range Coulomb repulsion is still to be determined. A promising alternative are conducting polymers which are tunable by atomic force microscopy techniques [208] and, owing to their small size, possess a huge charging energy such that the one-electron regime should be easier to reach.

6.3 Conclusions

We have investigated a current blockade mechanism for strongly biased contacted dimer chains. It results from an interplay of Coulomb repulsion and edge-state formation which relates to a TPT. The edge state at the source can trap an electron, while Coulomb repulsion inhibits a further electron to enter the chain. The resulting electron transport consists of rare tunnel events between the edge states and exhibits a characteristic Poissonian behavior. By contrast, in the topologically trivial region, we find transport through delocalized states and electron bunching. Since the edge state at the source turned out to be responsible, the effect can be observed also in chains with an odd number of sites in which a different but related transition occurs, namely, the displacement of the edge state from one end to the other. Clear experimental evidence for the transition between the different regions can be provided by shot noise measurements. While we have demonstrated that the mechanisms on both sides of the transition are fairly insensitive to static disorder, a more realistic description of an implementation with molecular wires should consider also spin effects, vibrational degrees of freedom, and decoherence.

Then we analyzed the influence of periodic driving on the current through this transport setup. In the present case the topological properties can be controlled in a very flexible manner via driving frequency and amplitude. In topologically nontrivial parameter regions, edge states emerge and significantly influence the Fano factor of the current. In turn, the Fano factor may be used to measure the Floquet topological phase diagram. As an interesting feature of driving-induced edge-state blockade, not only the behavior of the Fano factor, but also the shape of the current suppressions depends on topology. For the computation of the shot noise, we have developed a matrix-continued fraction method which is applicable whenever the time dependence of the current expectation value is weak, as is the case in our model. In summary, we have shown not only that Floquet engineering allows one to tune the topological properties of a SSH chain, but also that shot noise measurements may serve for detecting Floquet TPTs. Such measurements may be an essential ingredient for testing and gauging setups with applications in quantum information processing (QIP).

CHAPTER 7

DISSIPATIVE LONG-RANGE ENTANGLEMENT GENERATION

The physical realization of a large-scale quantum information processing (QIP) architecture constitutes a fascinating problem at the interface between fundamental science and engineering [4, 217]. Further advances towards this goal hinge upon two major challenges: (i) control over the environmental decoherence, and (ii) long-range coupling between the logical qubits. The latter not only relaxes some serious architectural challenges [59] but also allows for applications in quantum communication, distributed quantum computing, and some of the highest tolerances in error-correcting codes that are based on long-distance entanglement links [4, 218, 219].

In this work, we propose a scheme for deterministic preparation of *steady-state* entanglement between *remote* qubits, defined by electron spins confined in spatially separated electrically defined semiconductor quantum dots (QDs) [**P.6**]. Our approach addresses the two challenges (i) and (ii) as described above within one unified framework: (i) Our setup utilizes the approach of engineering by dissipation, presented in chapter 2.3, therefore it comes with potentially significant advantages over previous proposals [220–222] which aim at a coherent coupling between remote spins. (ii) Our scheme directly builds upon recent experimental developments towards the realization of a solid-state electronic quantum bus, where flying electrons take over the role of photons in more conventional atomic, molecular, and optical based approaches [95] in order to mediate long-range coupling between remote qubits. In particular, we consider quantum Hall (QH) edge channels [222–228] and surface acoustic waves (SAWs) [229–235] as exemplary candidate systems for the coherent transport of electron spins over long distances. Intuitively, the dissipative entanglement creation arises from a quantum interference effect in the common coupling of the localized spins $\mathbf{S}_i$ ($i = 1,2$) to an adjacent electronic quantum channel, in which flying electrons continuously pass by the two localized spins. With any which-way information

absent, first-order spin-flip processes between the localized spins and the flying ancilla spins occurring in the course of electron transport can happen either in the first *or* in the second node, which may lead to the formation of entanglement between the nodes, if two or more such processes with a unique common entangled steady state dominate the dynamics [96, 98].

In what follows, we show how our general idea can be applied to two different exemplary physical setups, with the ultimate goal of approximately implementing the paradigmatic entanglement-generating dynamics given in Eqs. (2.19) and (2.20), using a fermionic environment. First, we investigate QH edge states as this setup facilitates direct analogies to existing quantum optical schemes with photons [227]. Thereafter, we explore a setup based on electrically induced SAWs where the stroboscopic control over the effective interaction times between localized and flying electron spins [232, 233] results in larger amounts of entanglement. To treat each specific physical setup we employ two different input-output approaches tailored to the specific setups.

7.1 Localized and flying spins

In all setups specified below, to amplify the coupling between localized and flying electrons in a controlled way, we introduce auxiliary (ancilla) QDs that are tunnel-coupled to the QDs hosting the qubit electrons with spin $\mathbf{S}_i$ ($i = 1,2$). By appropriate gating one can ensure that the system QDs always stay occupied with a single electron each which opens up the possibility for storage of spin-spin entanglement between different (remote) QDs. An electron occupying the ancilla QD j interacts locally with the system spin $\mathbf{S}_i$ via the Heisenberg exchange interaction [31]

$$H_{\mathrm{IN}}^{i,j} = J_{i,j}\mathbf{S}_i \cdot \mathbf{a}_j, \tag{7.1}$$

where $\mathbf{a}_j = \frac{1}{2}\sum_{\sigma,\sigma'} d_{j\sigma}^{\dagger}\boldsymbol{\sigma}_{\sigma,\sigma'}d_{j\sigma'}$ refers to the spin-1/2 ancilla operator. Here $d_{j\sigma}^{\dagger}$ creates an electron with spin $\sigma = \uparrow,\downarrow$ in the ancilla QD j and $\boldsymbol{\sigma}$ is the vector of Pauli matrices. This interaction Hamiltonian can be separated as $H_{\mathrm{IN}}^{i,j} = H_{\mathrm{ff}}^{i,j} + H_{\mathrm{zz}}^{i,j}$ in terms of the perpendicular (*flip-flop*) and paralel (z-z) components

$$H_{\mathrm{ff}}^{i,j} = \frac{J_{i,j}}{2}\left(S_i^+ a_j^- + S_i^- a_j^+\right), \quad H_{\mathrm{zz}}^{i,j} = J_{i,j}S_i^z a_j^z, \tag{7.2}$$

with the raising and lowering spin operators $S_i^{\pm} = S_i^x \pm iS_i^y$ and $a_i^{\pm} = a_i^x \pm ia_i^y$. The exchange coupling $J_{i,j}$ can be as large as several tens of μeV and controlled *in situ* by gating of the tunneling barrier between two nearby QDs [30, 31].

The system is subject to an external magnetic field $\mathbf{B}$, taken along $\hat{z}$. In a suitable rotating frame the global homogeneous magnetic field drops out from the dynamics, and we are left with (small) inhomogeneous gradient fields, described by the Zeeman Hamiltonian

$$H_{\mathrm{Z}} = \sum_i \delta_i S_i^z. \tag{7.3}$$

Here, the magnetic gradients ($\delta_i \lesssim 2\mu$eV) can be engineered via on-probe micro- [236] or nano-magnets [237] and/or nuclear Overhauser fields [31].

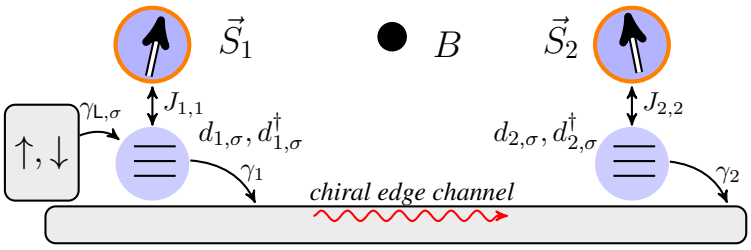

FIGURE 7.1. Cascaded quantum system with two nodes, consisting of one system and one ancilla QD each, with the ancilla QDs interconnected by a QH chiral edge channel. The first ancilla QD is tunnel-coupled to a reservoir that pumps electrons into the system.

In the following we describe two different ways to transport electrons from the first ancilla QD to the second such that they interact successively with the two localized spins.

7.2 Transport via QH edge states

A two-dimensional electron gas (2DEG) in a large magnetic field supports QH edge channels which have proven to provide an ideal test bed for electronic-optics-like experiments, since they allow for ballistic, one-dimensional, and chiral electron transport [227] (velocity $v \approx 10^4$m/s). Since backscattering is drastically reduced due to chirality, in the QH regime the mean-free path of electrons is increased up to $\sim (0.1-1)$mm [223–225]. Let us consider two nodes separated by a distance L, consisting of just one system and one ancilla QD each, with the ancilla QDs interconnected by such a chiral edge channel as sketched in Fig. 7.1. As we consider only the nearest resonant subband because the tunneling rates decrease exponentially with the distance from the QDs [225], this is a cascaded quantum system and one can apply the input-output formalism to describe its dynamical evolution as in Appendix E. For simplicity, we assume equal tunneling rates ($\gamma \equiv \gamma_1 = \gamma_2$). Moreover, we consider the case of an empty channel $\bar{N} = 0$, we need to account explicitly for spins and we add the contribution from the reservoir that pumps electrons (with spin σ) into the first ancilla QD (at rate $\gamma_{\mathrm{L},\sigma}$). Finally, if the spin-resolved levels of the two ancilla QDs are aligned, the system Hamiltonian term vanishes in the rotating frame. We then arrive at the Markovian master equation for the reduced density matrix of system and ancilla QDs,

$$\dot{\varrho} = -i\left[H_{\mathrm{Z}} + H_{\mathrm{IN}}, \varrho\right] + \mathscr{L}_{\mathrm{tr}}\varrho, \tag{7.4}$$

where H_{Z} accounts for Zeeman energies (Eq. 7.3), H_{IN} describes *local* spin-spin interactions between system and auxiliary QDs

$$H_{\mathrm{IN}} = \sum_{\langle i,j \rangle} H_{\mathrm{IN}}^{i,j}, \tag{7.5}$$

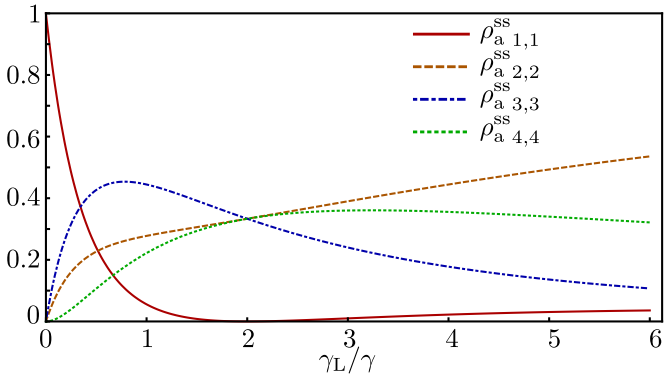

FIGURE 7.2. Value of the diagonal elements of the ancilla quasisteady state in Eq. (7.7) as a function of the ratio γ_L/γ.

and $\mathscr{L}_{tr}\varrho = \sum_\sigma \mathscr{L}_{tr,\sigma}\varrho$ describes electron transport. The latter reads explicitly

$$\mathscr{L}_{tr,\sigma}\varrho = \frac{\gamma_{L,\sigma}}{2}\mathscr{D}\left(d_{1\sigma}^\dagger\right)\varrho + \frac{\gamma}{2}\mathscr{D}(d_{1\sigma}+d_{2\sigma})\varrho + \frac{\gamma}{2}\left[d_{1\sigma}^\dagger d_{2\sigma} - d_{2\sigma}^\dagger d_{1\sigma},\varrho\right]. \tag{7.6}$$

Here, the first term describes spin-selective pumping of the first ancilla QD, which could be achieved either via ferromagnetic leads or spin-filtering techniques [238]. In our dissipative setup, electron pumping (resulting in an effective electron source) is required in order to obtain a genuine nonequilibrium situation with continuous electron driving. The last two terms give the *nonlocal* incoherent and coherent contributions of the channel-mediated coupling between the ancilla QDs, respectively. The theoretical treatment underlying Eq. (7.6) assumes weak coupling to the reservoir and a flat reservoir spectral density (Born-Markov approximation), an idealized dispersion-free channel, and the spin-resolved ancilla QD levels to be aligned within $\lesssim\gamma$ [225].

For fast dissipation ($\gamma,\gamma_L \gg J$), the auxiliary QDs settle into a quasisteady state, ρ_a^{ss}, on a time scale much shorter than the relevant system-QDs dynamics. In this case, the interaction H_{IN} can be treated perturbatively and one can adiabatically eliminate the ancilla coordinates yielding a coarse-grained equation of motion for the system spins ($\mathbf{S}_1,\mathbf{S}_2$). We now compute and analyze this quasisteady state since it will play a central role for the derivation of the system QDs master equation. If a single spin component is introduced, $\gamma_{L,\downarrow}=0$ and $\gamma_L \equiv \gamma_{L,\uparrow}$, the quasisteady state associated with Eq. (7.6) ($\mathscr{L}_{tr}\rho_a^{ss}=0$) reads

$$\rho_a^{ss} = \frac{1}{(\gamma_L+\gamma)(\gamma_L+2\gamma)^2}\begin{pmatrix} \gamma(2\gamma-\gamma_L)^2 & 0 & 0 & 0 \\ 0 & \gamma_L(4\gamma^2+\gamma_L^2) & -2\gamma\gamma_L(\gamma_L+2\gamma) & 0 \\ 0 & -2\gamma\gamma_L(\gamma_L+2\gamma) & 8\gamma_L\gamma^2 & 0 \\ 0 & 0 & 0 & 4\gamma\gamma_L^2 \end{pmatrix}, \tag{7.7}$$

in the basis $\{|0,0\rangle,|\uparrow,0\rangle,|0,\uparrow\rangle,|\uparrow,\uparrow\rangle\}$. The average populations of the ancilla QDs depend on the reservoir and channel rates as shown in Fig. 7.2.

As this state is not pure, we use the entanglement of formation, E_F, defined in Appendix D, to quantify its amount of entanglement. For all $\gamma, \gamma_L \neq 0$, the quasisteady state is entangled (due to the Markovian coupling to the common channel) and reaches an E_F of ~ 0.55 at $\gamma_L = 2\gamma$, at which point the steady state is a mixture of the two-electron state $|\uparrow,\uparrow\rangle$ and the maximally entangled state $|\uparrow,0\rangle - |0,\uparrow\rangle$ that is a "dark state" for the collective coupling via the operator $(d_{1,\uparrow} + d_{2,\uparrow})$ in Eq. (7.6). However, this entanglement comes in a form of limited usefulness as it involves a superposition of a single fermion in the first or in the second ancilla and due to fermionic superselection rules a single such state (while entangled [239, 240]) cannot be distinguished from a separable state by local operations. Our scheme shows that this entanglement can still provide the quantum correlations necessary to produce a usable spin-qubit entanglement for the system spins, which are weakly coupled to this ancilla system.

Comment on the time delay

In accordance with the cascaded nature of the system, ϱ in Eq. (7.6) takes into account a time delay between systems 1 and 2. If transport happens almost instantaneously even on the time-scale of the channel-ancilla coupling ($L/v \ll 1/\gamma$), the delay can be neglected and the quasisteady state in Eq. (7.7) can be understood as an equal-times state. As $\gamma \sim 10\mu$eV, this condition limits the length of the edge channels to $L < 1\mu$m. For larger separations ($L/v \gg 1/\gamma$) we see that the first QD is driven into its steady state before the electrons that interact with it have time to reach the second QD. Hence we conclude that at any given time, QD 1 and QD 2 are not entangled; instead, QD 1 is getting entangled with the bath (the electron modes in the channel connecting the two QDs). This notwithstanding, as the cascaded equation tells us, this system-bath entanglement is faithfully transported to QDs so that time-delayed measurements at the two QDs show strong quantum correlations. If other quantum systems (such as the system spins in our setup) interact weakly with these two correlated ancillas they are exposed to a nonlocal master equation that can be effectively taken as an equal-time equation if L/v is short compared to the time scale of the qubit dynamics, shown later to be of the order of J^2/γ. For realistic parameter values, $J \sim \mu$eV, we thus obtain a standard equal-time entangled steady state for channel lengths of up to a few tens of micrometers.

Adiabatic elimination of the ancilla coordinates

The subsequent full calculation to adiabatically eliminate the ancilla coordinates and obtain an effective master equation for the system spins follows the general framework developed in Ref. [241] and presented in Appendix F of this thesis. The first-order contributions $\sim J$ result in effective, local magnetic fields for the system spins $\mathbf{S}_i$, which are oriented along the quantization axis z. As discussed in more detail below, via a suitable choice of the local magnetic gradients δ_i in Eq. (7.3) these first-order terms can cancel out. To second order, nonlocal charge correlations

inherent to the ancilla system are transferred to the system spins resulting in an effective master equation with one dominant nonlocal term.

Our auxiliary QDs undergo fast dynamics given by the Liouvillian $\mathscr{L}_{\rm tr}$, while the perturbative part contains the Heisenberg interaction and the Zeeman Hamiltonian. By comparison with the generic perturbation term utilized in Appendix F,

$$\mathscr{V}\varrho = -i\sum_{m=1}^{N}\left[A_m \otimes S_m, \varrho\right] - i\sum_{m=1}^{N} b_m\left[S_m, \varrho\right] \ , \tag{7.8}$$

the system operators S_m are S_i^{α}, with $i = 1,2$ and $\alpha = x,y,z$, the generic ancilla operators A_m are $\sum_{<j>} J_{i,j} a_j^{\alpha}$, where $j = 1,...4$ and site j is locally in contact to site i, and b_m are the local magnetic gradients δ_i. According to Appendix F the first-order contribution is given by the mean value of the magnetic field created by the ancilla electrons in the quasisteady state $\rho_{\rm a}^{\rm ss}$, i.e., $\left\langle a_i^z \right\rangle_{\rm ss} = {\rm tr}_{\rm a}\left\{a_i^z \rho_{\rm a}^{\rm ss}\right\}$ (${\rm tr}_{\rm a}[\ldots]$ denotes the trace over the auxiliary degrees of freedom), plus the system Hamiltonian,

$$\mathscr{L}^{(1)} = -i\left[\sum_i \delta_i S_i^z + \sum_{\langle i,j\rangle}\left\langle a_j^z\right\rangle_{\rm ss} J_{i,j} S_i^z, \rho\right] \ , \tag{7.9}$$

where $\rho = {\rm tr}_{\rm a}[\varrho]$. The local constant fields δ_i can then be chosen such that they cancel out Eq. (7.9) and will be on the order of the exchange coupling.

Then we calculate the second-order contribution, $\mathscr{L}^{(2)}$, of the coupling to two ancilla QDs connected via a unidirectional channel ($J_i \equiv J_{i,i}$). It has a term due to the parallel component of the Heisenberg interaction ($z-z$),

$$\mathscr{L}_{\rm zz}\rho = \sum_{i=1}^{2} J_i^2 \mathscr{C}\left(a_i^z, a_i^z\right)\mathscr{D}\left(S_i^z\right)\rho + J_1 J_2\left(\mathscr{C}\left(a_2^z, a_1^z\right) + \mathscr{C}\left(a_1^z, a_2^z\right)\right)\left(\left[S_1^z\rho, S_2^z\right] + \left[S_2^z, \rho S_1^z\right]\right), \tag{7.10}$$

and another one due to the perpendicular component ($flip-flop$),

$$\mathscr{L}_{\rm ff}\rho = \sum_{i=1}^{2} \mathscr{C}\left(a_i^+, a_i^-\right)\frac{J_i^2}{4}\mathscr{D}(S_i^+)\rho + \mathscr{C}\left(a_2^+, a_1^-\right)\frac{J_1 J_2}{4}\left\{\left[S_1^+\rho, S_2^-\right] + \left[S_2^+, \rho S_1^-\right]\right\}. \tag{7.11}$$

Here the correlation functions are defined as

$$\mathscr{C}\left(A_m, A_l\right) = {\rm tr}_{\rm a}\left\{\delta A_m \mathscr{L}_{\rm tr}^{-1}\delta A_l \rho_{\rm a}^{\rm ss}\right\} \ , \tag{7.12}$$

where $\delta A_m = A_m - \langle A_m\rangle_{\rm ss}$ and $\mathscr{L}_{\rm tr}^{-1}$ is denotes the pseudoinverse of that Liouvillian (since a Liouvillian operator is singular, it does not have a proper inverse). In Fig. 7.3, we represent schematically the second-order processes related to the operators $a_i^{\pm}$. Note that the unidirectionality of the channel implies $\mathscr{C}\left(a_1^+, a_2^-\right) = 0$.

For practical reasons, it is more adequate to express Eqs. (7.10) and (7.11) by means of nonlocal terms. By simply diagonalizing the quadratic form we end up with

$$\mathscr{L}_{\rm zz}\rho = \Gamma_+^{\rm zz}\mathscr{D}\left(\cos\frac{\theta_{\rm zz}}{2}S_1^z + \sin\frac{\theta_{\rm zz}}{2}S_2^z\right)\rho + \Gamma_-^{\rm zz}\mathscr{D}\left(\sin\frac{\theta_{\rm zz}}{2}S_1^z - \cos\frac{\theta_{\rm zz}}{2}S_2^z\right)\rho \ , \tag{7.13}$$

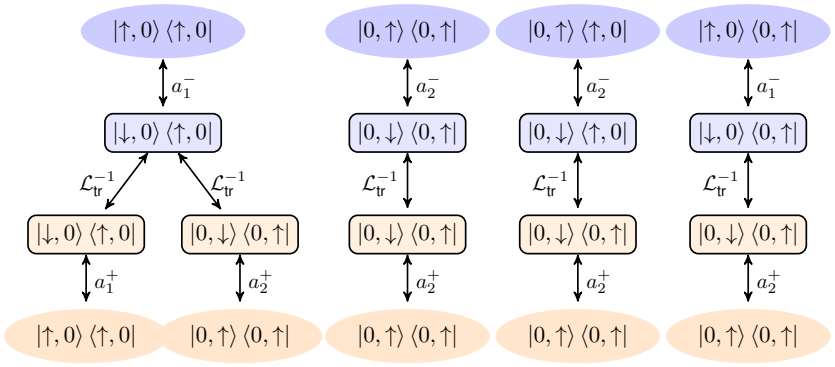

FIGURE 7.3. Schematic representation of the second-order correlation functions; compare Eq. (7.12). The different components of $\rho_{\rm a}^{\rm ss}$ are coupled to the elements in rectangles via ancilla spin-flip operators $a_{1,2}^-$. Then, the pseudoinverse of the transport Liouvillian $\mathscr{L}_0 \equiv \mathscr{L}_{\rm tr}$ couples them to the matrix elements shown in the bottom rectangles. Finally, a second application of the ancilla spin-flip operators couples the initial component to the components shown in the bottom ellipses. For simplicity, this example refers to the limiting case $\gamma_{\rm L} \ll \gamma$. In this regime one can restrict the discussion to the single-electron regime, where at most a single electron is found in the ancilla system (comprising the two ancilla QDs) and the population of the state with one electron in each of the two auxiliary QD is negligibly small. Moreover, double occupation of a single ancilla QD is disregarded due to strong Coulomb interaction effects. Note that this schematic representation refers to just two system QDs coupled to just two ancilla QDs interconnected by a single channel.

and

$$\mathscr{L}_{\rm ff}\rho = \Gamma_+^{\rm ff}\mathscr{D}\left(\cos\frac{\theta_{\rm ff}}{2}S_1^+ + \sin\frac{\theta_{\rm ff}}{2}S_2^+\right)\rho + \Gamma_-^{\rm ff}\mathscr{D}\left(\sin\frac{\theta_{\rm ff}}{2}S_1^+ - \cos\frac{\theta_{\rm ff}}{2}S_2^+\right)\rho - \Delta\left[S_2^-S_1^+ - S_1^-S_2^+,\rho\right] . \quad (7.14)$$

The rates in Eqs. (7.13) and (7.14) are all given in terms of the correlation functions as

$$\Gamma_\pm^{\rm zz} = \sum_{i=1}^{2}\frac{\mathscr{C}\left(a_i^z\right)J_i^2}{2} \pm \frac{\sqrt{\left[\mathscr{C}\left(a_1^z\right)J_1^2 - \mathscr{C}\left(a_2^z\right)J_2^2\right]^2 + \left[\mathscr{C}\left(a_1^z,a_2^z\right) + \mathscr{C}\left(a_2^z,a_1^z\right)\right]^2 J_1^2J_2^2}}{2}; \quad (7.15)$$

$$\Gamma_\pm^{\rm ff} = \sum_{i=1}^{2}\frac{\mathscr{C}\left(a_i^+,a_i^-\right)J_i^2}{8} \pm \frac{\sqrt{\left[\mathscr{C}\left(a_1^+,a_1^-\right)J_1^2 - \mathscr{C}\left(a_2^+,a_2^-\right)J_2^2\right]^2 + \mathscr{C}\left(a_2^+,a_1^-\right)^2 J_1^2J_2^2}}{8}; \quad (7.16)$$

where we have defined $\mathscr{C}(A_m) \equiv \mathscr{C}(A_m,A_m)$ for simplicity. The angles that define the nonlocal operators into the Lindblad dissipators are

$$\theta_{\rm zz} = \arctan\frac{\left(\mathscr{C}\left(a_1^z,a_2^z\right) + \mathscr{C}\left(a_2^z,a_1^z\right)\right)J_1J_2}{\mathscr{C}\left(a_1^z\right)J_1^2 - \mathscr{C}\left(a_2^z\right)J_2^2}; \quad (7.17)$$

$$\theta_{\rm ff} = \arctan\frac{\mathscr{C}\left(a_2^+,a_1^-\right)J_1J_2}{\mathscr{C}\left(a_1^+,a_1^-\right)J_1^2 - \mathscr{C}\left(a_2^+,a_2^-\right)J_2^2} . \quad (7.18)$$

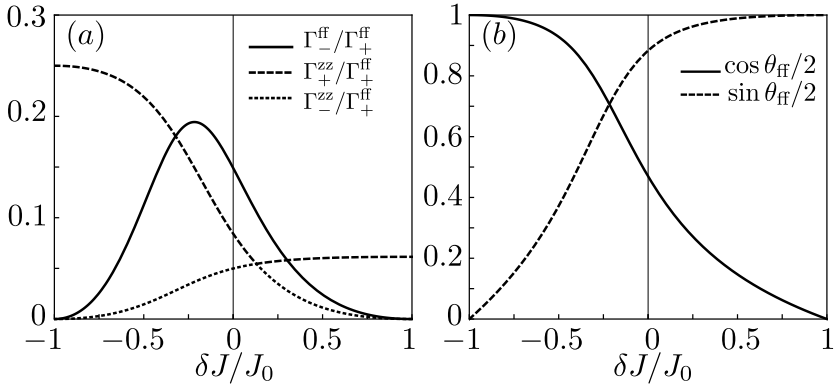

FIGURE 7.4. (a) Rates of the effective master equation for the system spins. Since the rate $\Gamma_+^{\rm ff}$ dominates, we show in (b) the structure of the corresponding nonlocal operator $\cos\frac{\theta_{\rm ff}}{2}S_1^+ + \sin\frac{\theta_{\rm ff}}{2}S_2^+$ as a function of δJ, with $J_{1(2)} = J_0 \mp \delta J$.

Finally, the Hamiltonian term in Eq. (7.14) is an effective coherent spin interaction between the spatially separated spins mediated by the reservoir with strength

$$\Delta = \frac{\mathscr{C}\left(a_2^+, a_1^-\right) J_1 J_2}{8}\,. \tag{7.19}$$

Dominating processes

Following the intuition of spin-flip processes between the localized spins and the ancilla electrons, we expect that a nonlocal term may dominate over all other processes. In Fig. 7.4 (a) the different rates contributing to Eqs. (7.13) and (7.14) are shown as a function of the coupling strength difference δJ, with $J_{1(2)} = J_0 \mp \delta J$. Clearly, the rate $\Gamma_+^{\rm ff}$ is found to dominate. However, other processes may not be neglected completely. Note that we have chosen the case of equal rates $\gamma_{\rm L} = \gamma$ for simplicity because it is close to the optimum working point (not shown). For this particular case, the ancilla quasisteady state reads

$$\rho_{\rm a}^{\rm ss} = \frac{1}{18}\begin{pmatrix} 1 & 0 & 0 & 0 \\ 0 & 5 & -6 & 0 \\ 0 & -6 & 8 & 0 \\ 0 & 0 & 0 & 4 \end{pmatrix}, \tag{7.20}$$

the average fields are $\langle a_1^z \rangle_{\rm ss} = 1/4$ and $\langle a_2^z \rangle_{\rm ss} = 1/3$ and the correlation functions are

$$\mathscr{C}\left(a_1^+, a_1^-\right) = \frac{1}{2\gamma}; \quad \mathscr{C}\left(a_2^+, a_2^-\right) = \frac{76}{63\gamma}; \quad \mathscr{C}\left(a_2^+, a_1^-\right) = \frac{22}{21\gamma}; \quad \mathscr{C}\left(a_1^+, a_2^-\right) = 0; \tag{7.21}$$

$$\mathscr{C}\left(a_1^z, a_1^z\right) = \frac{1}{32\gamma}; \quad \mathscr{C}\left(a_2^z, a_2^z\right) = \frac{1}{54\gamma}; \quad \mathscr{C}\left(a_1^z, a_2^z\right) = -\frac{1}{72\gamma}; \quad \mathscr{C}\left(a_2^z, a_1^z\right) = \frac{1}{72\gamma}. \tag{7.22}$$

In Fig. 7.4 (b) we show the structure of the dominating term,

$$\Gamma_+^{\rm ff}\mathscr{D}\left(\cos\frac{\theta_{\rm ff}}{2}S_1^+ + \sin\frac{\theta_{\rm ff}}{2}S_2^+\right)\rho, \tag{7.23}$$

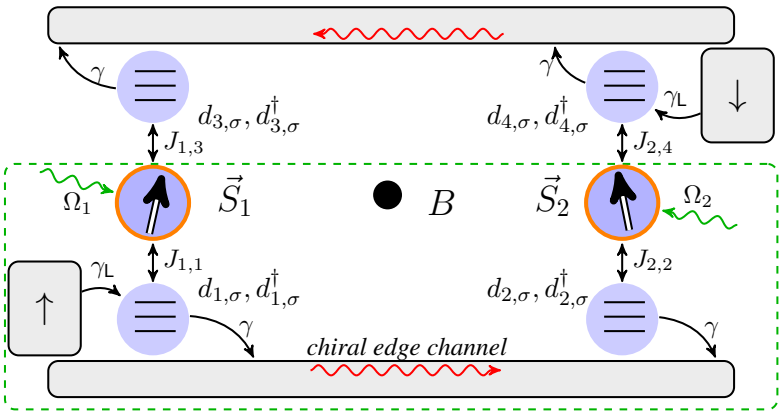

FIGURE 7.5. Scheme of the QH-based setups. Two spatially separated qubits ($\mathbf{S}_1, \mathbf{S}_2$) are coupled to auxiliary QDs, which are interconnected by a unidirectional QH edge channel. The upstream ancilla QD(s) are pumped selectively from a Fermi reservoir with a rate γ_L. While the first (purely dissipative) scheme requires two separate QH edge channels, for the second scheme a single channel suffices (dashed box) together with local driving fields of strength Ω_i.

as a function of the coupling strength difference δJ. This nonlocal Lindblad term features two steady states: $|\Psi_{ss,1}\rangle = \cos\frac{\theta_{ff}}{2}|\uparrow\downarrow\rangle - \sin\frac{\theta_{ff}}{2}|\downarrow\uparrow\rangle$ and a simple product state $|\Psi_{ss,2}\rangle = |\uparrow\uparrow\rangle$. To destabilize the second (unentangled) stationary solution, we can either (i) add an extra channel or (ii) apply a coherent driving to the localized spins in order to (approximately) recover the dynamics stated in Eqs. (2.19) and (2.20), respectively. In both scenarios, sketched in Fig. 7.5 and detailed below, the steady state will be unique, which makes the scheme robust against initialization errors.

7.2.1 Two channels and no driving

To mimic Eq. (2.19), we consider a purely dissipative setting with two separate edge channels with electrons traveling in the opposite direction (from 4 to 3 in Fig. 7.5) that are pumped spin-selectively by spin-up (spin-down) electrons only, respectively, and with the following symmetry in the exchange couplings: $J_1 \equiv J_{1,1} = J_{2,4}$, $J_2 \equiv J_{2,2} = J_{1,3}$, interacting through different ancilla QDs with the qubits. Here, two separate channels are introduced in order to effectively obtain not only one, but two independent, nonlocal Lindblad operators. The latter is needed to (approximately) emulate the paradigm master equation (2.19) with two independent Lindblad operators, which (under the conditions specified in chapter 2.3) ensures a unique steady state. The spin of the injected electron determines the type of nonlocal Lindblad operator in the effective master equation for the system spins: Injecting a spin-up electron into the ancilla system will result in a collective flip $\mathscr{D}[\mu S_1^+ + \nu S_2^+]\rho$, because the ancilla electron can only flip to spin-down (which comes with a spin-raising flip to the system spins), whereas injecting a spin-down electron into

the ancilla system will lead to a collective flip of the form $\mathscr{D}[\nu S_1^- + \mu S_2^-]\rho$, because the ancilla electron can only flip to spin-up (which comes with a spin-lowering flip to the system spins). In this setting, the quantized levels in the ancilla QDs help to suppress undesired, parasitic local processes where electrons are transferred from the lower to the upper edge channel, or reversed, by virtually occupying the system QD.

Summing up the first-order contributions from the two channels, the Zeeman energies (7.3) necessary to cancel the first-order term are (see Eq. 7.9)

$$\delta_{1(2)} = \mp \left(J_1 \langle a_1^z \rangle_{ss} - J_2 \langle a_2^z \rangle_{ss} \right) \tag{7.24}$$

(the index in parentheses refers to the lower sign), which in the case of equal rates become $\delta_{1(2)} = \pm(J_0 + 7\delta J)/12$. For the second-order term of the adiabatic elimination we need to calculate the correlation functions $\mathscr{C}\left(a_i^+, a_j^-\right)$ and $\mathscr{C}\left(a_i^z, a_j^z\right)$; $i,j = 1,...4$. In particular these include cross-correlations between the two channels. As the ancilla QD 4 (3) is symmetric to 1 (2), the correlations into the same channel do not need to be computed again. Since the ancilla quasisteady state does not contain any cross-channel correlations, nonlocal, cross-channel correlators vanish (when one traces out the ancilla degrees of freedom). Then the new channel contributes mainly with the dissipator

$$\Gamma_+^{\mathrm{ff}} \mathscr{D}\left(\cos\frac{\theta_{\mathrm{ff}}}{2} S_2^- + \sin\frac{\theta_{\mathrm{ff}}}{2} S_1^- \right) \rho \tag{7.25}$$

[note the symmetry $S_1^{+(-)} \leftrightarrow S_2^{-(+)}$ when comparing to Eq. (7.23)] and the ensuing effective master equation for the two qubits only reads

$$\dot{\rho} = \Gamma_+^{\mathrm{ff}} \mathscr{D}\left(\cos\frac{\theta_{\mathrm{ff}}}{2} S_1^+ + \sin\frac{\theta_{\mathrm{ff}}}{2} S_2^+ \right) \rho + \Gamma_+^{\mathrm{ff}} \mathscr{D}\left(\cos\frac{\theta_{\mathrm{ff}}}{2} S_2^- + \sin\frac{\theta_{\mathrm{ff}}}{2} S_1^- \right) \rho + \mathscr{L}_{\text{n-id}}^{(1)} \rho \ , \tag{7.26}$$

where we have included all the non-dominating (nonideal) terms in

$$\begin{aligned} \mathscr{L}_{\text{n-id}}^{(1)} \rho \quad = \quad & -2\Delta \left[S_2^- S_1^+ - S_1^- S_2^+, \rho \right] + \sum_{\sigma=\pm} \Gamma_\sigma^{\mathrm{zz}} \left\{ \mathscr{D}\left(\mathbf{v}_{\mathrm{zz}}^\sigma \cdot \left(S_1^z, S_2^z \right) \right) + \mathscr{D}\left(\mathbf{v}_{\mathrm{zz}}^\sigma \cdot \left(S_2^z, S_1^z \right) \right) \right\} \rho \\ & + \Gamma_-^{\mathrm{ff}} \mathscr{D}\left(\sin\frac{\theta_{\mathrm{ff}}}{2} S_1^+ - \cos\frac{\theta_{\mathrm{ff}}}{2} S_2^+ \right) \rho + \Gamma_-^{\mathrm{ff}} \mathscr{D}\left(\sin\frac{\theta_{\mathrm{ff}}}{2} S_2^- - \cos\frac{\theta_{\mathrm{ff}}}{2} S_1^- \right) \rho \ , \end{aligned} \tag{7.27}$$

with $\mathbf{v}_{\mathrm{zz}}^+ = \left(\cos\frac{\theta_{\mathrm{zz}}}{2}, \sin\frac{\theta_{\mathrm{zz}}}{2} \right)$ and $\mathbf{v}_{\mathrm{zz}}^- = \left(\sin\frac{\theta_{\mathrm{zz}}}{2}, -\cos\frac{\theta_{\mathrm{zz}}}{2} \right)$.

The master equation given in Eq. (7.26) indeed features *nonlocal* transport-mediated Lindblad terms of the same squeezing-type form as given in Eq. (2.19), with $\mu \equiv \cos\frac{\theta_{\mathrm{ff}}}{2}$ and $\nu \equiv \sin\frac{\theta_{\mathrm{ff}}}{2}$.

7.2.2 One channel and driving

Next, we follow the same strategy to (approximately) recover Eq. (2.20). To do so, we consider a potentially simpler setup, where a single channel suffices, but an additional (weak) resonant drive needs to be introduced (dashed box of Fig. 7.5). The Hamiltonian

$$H_{\mathrm{d}} = \sum_{i=1,2} 2\Omega_i S_i^x \tag{7.28}$$

describes electron-spin-resonance driving of the spins in the rotating frame. Again for $\gamma, \gamma_{\rm L} \gg J$, this system is described by

$$\dot{\rho} = -i\left[H_{\rm d}, \rho\right] - \Delta\left[S_2^- S_1^+ - S_1^- S_2^+, \rho\right] + \Gamma_+^{\rm ff}\mathscr{D}(\mathbf{v}_{\rm ff}^+ \cdot (S_1^+, S_2^+))\rho + \mathscr{L}_{\rm n\text{-}id}^{(2)}\rho, \tag{7.29}$$

with the nonideal Liouvillian

$$\mathscr{L}_{\rm n\text{-}id}^{(2)}\rho = \sum_{\sigma=\pm} \Gamma_\sigma^{zz}\mathscr{D}(\mathbf{v}_{zz}^\sigma \cdot \left(S_1^z, S_2^z\right))\rho + \Gamma_-^{\rm ff}\mathscr{D}(\mathbf{v}_{\rm ff}^- \cdot \left(S_1^+, S_2^+\right))\rho \ . \tag{7.30}$$

Here, the Zeeman energies have been chosen as

$$\delta_i = -J_i \langle a_i^z \rangle_{ss}, \tag{7.31}$$

i.e., $\delta_1 = -(J_0 - \delta J)/4$ and $\delta_2 = -(J_0 + \delta J)/3$.

As evident from Eqs. (7.26) and (7.29) the *continuous* interaction of the two spin qubits with the entangled steady state of the ancilla electrons gives rise to more than just the desired Lindblad terms (see the rates comparison in Fig. 7.4). To address this limitation, we discuss below an alternative *stroboscopic* (that is, not continuous) setup which allows for better control of the system-ancilla interactions and therefore yields more ideal effective dynamics.

7.3 Transport via SAW moving QDs

To this end we replace the edge channels by mobile QDs based on SAWs. Here, we consider two ancilla QDs which are interconnected by a long depleted one-dimensional channel in a 2DEG; compare Fig. 7.6. Recently, it has been demonstrated experimentally that in such a setup SAWs can transfer reliably and on-demand single electrons from one QD to the other for distances of several micrometers [232, 233], with the potential to extend this to hundreds of micrometers [235]. Our protocol then consists of a continuous train of mobile QDs that interact successively with the two system spins $\mathbf{S}_i$ for a (electrostatically) controlled time τ_i, very much like in a conveyor belt. Therefore, for a single ancilla electron the protocol comprises five steps: (i) load the first ancilla QD with electron spin σ, (ii) interact with system spin $\mathbf{S}_1$ via Heisenberg coupling (7.1) for a time τ_1, (iii) transfer the electron to the second ancilla QD (generically, $\mathbf{S}_1$ and the mobile electron are entangled by now), (iv) interact with system spin $\mathbf{S}_2$ via Heisenberg coupling (7.1) for a time τ_2, and (v) eject the electron from the second ancilla QD. The corresponding concatenated evolution for the two localized spins $\mathbf{S}_i$ ($i = 1,2$) can be described by [242]

$$\rho^{(n)} = {\rm tr}_{\rm a}[e^{\mathscr{L}_{2,n}\tau_2} e^{\mathscr{L}_{1,n}\tau_1}(\rho^{(n-1)} \otimes |\sigma_{n-1}\rangle\langle\sigma_{n-1}|)], \tag{7.32}$$

where $\rho^{(n)}$ defines the state after the $n-$th cycle of the protocol. Here, the trace is taken over the ancilla degrees of freedom and the Liouvillian $\mathscr{L}_{i,n}$ encodes both the interaction of the auxiliary electron with the main qubit $i = 1,2$ (Eq. 7.1 with spin-dependent exchange coupling) and Zeeman terms, Eq. (7.3). This model assumes perfect spin transfer which is approximately correct for

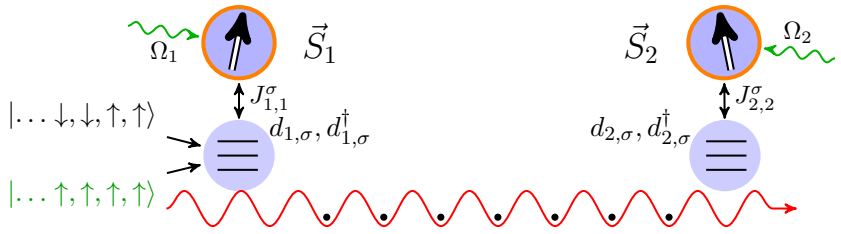

FIGURE 7.6. Scheme of the SAW-based setups. Two spatially separated qubits $(\mathbf{S}_1, \mathbf{S}_2)$ are coupled to auxiliary QDs, which are interconnected by a depleted one-dimensional channel. Via mobile QDs single electrons are continuously transferred between the two ancilla QDs, where they interact successively with the system spins $\mathbf{S}_i$ for a controlled interaction time τ_i.

distances much shorter than the characteristic dephasing length scale which we estimate as $\sim v_s T_2^* \gtrsim 100\mu$m for $v_s \approx 3\mu$m/ns and $T_2^* \approx 100$ns [233]. For $J\tau, \delta\tau \ll 1$, we can perform a short-time Taylor expansion $e^{\mathscr{L}_{i,n}\tau} = 1 + \tau\mathscr{L}_{i,n} + \frac{\tau^2}{2}\mathscr{L}^2_{i,n} + \ldots$ to approximate $\rho^{(n)}$ to second order (let us employ for simplicity equal times $\tau \equiv \tau_1 = \tau_2$),

$$\begin{aligned}
\rho^{(n)} &= \mathrm{tr}_a\left\{\varrho^{(n-1)} - i\tau\left[H_Z + H^{1,1}_{IN}, \varrho^{(n-1)}\right] - i\tau\left[H_Z + H^{2,2}_{IN}, \varrho^{(n-1)}\right]\right\} \\
&+ \mathrm{tr}_a\left\{\frac{\tau^2}{2}\mathscr{D}\left(H_Z + H^{1,1}_{IN}\right)\varrho^{(n-1)} + \frac{\tau^2}{2}\mathscr{D}\left(H_Z + H^{2,2}_{IN}\right)\varrho^{(n-1)}\right\} \\
&+ \tau^2\mathrm{tr}_a\left\{\left[H_Z + H^{2,2}_{IN}, \varrho^{(n-1)}\left(H_Z + H^{1,1}_{IN}\right)\right] + \left[\left(H_Z + H^{1,1}_{IN}\right)\varrho^{(n-1)}, H_Z + H^{2,2}_{IN}\right]\right\} + \mathscr{O}\left(\tau^3 J^3\right) .
\end{aligned} \tag{7.33}$$

If the injected spin is $|\sigma_{n-1}\rangle = |\uparrow\rangle$, that reads

$$\begin{aligned}
\rho^{(n)} &= \rho^{(n-1)} - 2i\tau\left[\delta_1 S^z_1 + \delta_2 S^z_2, \rho^{(n-1)}\right] - \frac{i}{2}\tau\left[J^{\uparrow}_1 S^z_1 + J^{\uparrow}_2 S^z_2, \rho^{(n-1)}\right] \\
&+ \frac{\tau^2}{2}\mathscr{D}\left[\left(2\delta_1 + \frac{J^{\uparrow}_1}{2}\right)S^z_1 + \left(2\delta_2 + \frac{J^{\uparrow}_2}{2}\right)S^z_2\right]\rho^{(n-1)} \\
&+ \frac{1}{8}\mathscr{D}\left[\tau J^{\uparrow}_1 S^+_1 + \tau J^{\uparrow}_2 S^+_2\right]\rho^{(n-1)} + \tau^2\frac{J^{\uparrow}_1 J^{\uparrow}_2}{8}\left[S^-_1 S^+_2 - S^-_2 S^+_1, \rho^{(n-1)}\right] + \mathscr{O}\left(\tau^3 J^3\right)
\end{aligned} \tag{7.34}$$

and if $|\sigma_n\rangle = |\downarrow\rangle$ the next step is given by

$$\begin{aligned}
\rho^{(n+1)} &\simeq \rho^{(n)} - 2i\tau\left[\delta_1 S^z_1 + \delta_2 S^z_2, \rho^{(n)}\right] + \frac{i}{2}\tau\left[J^{\downarrow}_1 S^z_1 + J^{\downarrow}_2 S^z_2, \rho^{(n)}\right] \\
&+ \frac{\tau^2}{2}\mathscr{D}\left[\left(2\delta_1 - \frac{J^{\downarrow}_1}{2}\right)S^z_1 + \left(2\delta_2 - \frac{J^{\downarrow}_2}{2}\right)S^z_2\right]\rho^{(n)} \\
&+ \frac{1}{8}\mathscr{D}\left[\tau J^{\downarrow}_1 S^-_1 + \tau J^{\downarrow}_2 S^-_2\right]\rho^{(n)} - \tau^2\frac{J^{\downarrow}_1 J^{\downarrow}_2}{8}\left[S^-_1 S^+_2 - S^-_2 S^+_1, \rho^{(n)}\right] + \mathscr{O}\left(\tau^3 J^3\right) .
\end{aligned} \tag{7.35}$$

Along the lines of our previous analysis, in what follows we present two SAW-based schemes: (i) a protocol with alternating spin directions and suitably synchronized exchange couplings and (ii) a spin-polarized protocol with a coherent driving. Both transport protocols will be shown to drive the localized spins to an entangled steady state, independently of the initial state.

7.3.1 Alternating spin sequences

To recover the purely dissipative dynamics (2.19), we assume alternating spin sequences (as could be realized by proper spin filtering on subnanosecond time scales [238]), together with appropriately synchronized interaction times τ_i or exchange couplings $J_i^\sigma \equiv J_{i,i}^\sigma$. This is necessary to achieve the desired asymmetry $\mu \neq \nu$. The concatenation of two steps with the injection of an opposite spin results in a first-order term that can be canceled by choosing the Zeeman energies as $\delta_i = -(J_i^\uparrow - J_i^\downarrow)/8$. Setting in addition $\tau J_1^\uparrow = \tau J_2^\downarrow \equiv \mu$ and $\tau J_1^\downarrow = \tau J_2^\uparrow \equiv \nu$, this is simply a gradient of magnetic field between the two localized spins: $\delta_{1(2)} = \mp \delta J/4$, with $J_{1(2)}^\uparrow = J_0 \mp \delta J$. Not only the first-order terms but also the dephasing second-order terms in Eqs. (7.34) and (7.35) cancel and it is readily seen that, up to $\mathcal{O}(\tau^3 J_i^{\sigma 3})$, the evolution of the density matrix simplifies to

$$\rho^{(n+1)} - \rho^{(n-1)} = \frac{1}{8}\mathscr{D}\left(\mu S_1^+ + \nu S_2^+\right)\rho^{(n-1)} + \frac{1}{8}\mathscr{D}\left(\mu S_2^- + \nu S_1^-\right)\rho^{(n-1)}. \tag{7.36}$$

Indeed, we recover *nonlocal* dissipators of the desired asymmetric (squeezing-type) form, as in Eq. (2.19). Alternating sequences of spin-up and spin-down electrons (with suitably synchronized couplings) then yield approximately the desired entangling dynamics.

7.3.2 Single spin-component and driving

Next, to emulate dynamics similar to Eq. (2.20), we assume mobile QDs with a single spin-filtered spin-component [238] and introduce an additional coherent external driving field. In this case, for asymmetric, but *time-independent* couplings ($\mu = J_1^\uparrow \tau$, $\nu = J_2^\uparrow \tau$), magnetic gradients $\delta_i = -J_i^\uparrow/4$ and weak driving $\Omega_{1,2} \ll J$, the evolution of the density matrix is approximately given by

$$\rho^{(n)} = \rho^{(n-1)} + \frac{\mu\nu}{8}\left[S_1^- S_2^+ - S_2^- S_1^+, \rho^{(n-1)}\right] + 1/8\mathscr{D}\left(\mu S_1^+ + \nu S_2^+\right)\rho^{(n-1)} - 2i\tau\left[H_\mathrm{d}, \rho^{(n-1)}\right]. \tag{7.37}$$

Thus, we can realize the dynamics of Eqs. (2.19) and (2.20) with arbitrary accuracy by reducing the dwell times τ_i.

Note that for a direct comparison of Eqs. (7.36) and (7.37) with a master equation, one needs to assume infinitesimal interaction times, but we have confirmed that the schemes work for finite interaction times.

7.4 Results and discussion

In the previous section, we have derived master-equation-based models for four different physical setups in total, two of them based on QH edge channels and the remaining two based on SAW-induced moving QDs. In this section, we specify the experimental requirements and discuss in detail the results of our analysis, as quantified via the amount of entanglement that the different setups are able to generate between two remote spin qubits under realistic conditions. First, we discuss the QH-based proposals, then the SAW-based proposals; we conclude the discussion with a comprehensive comparison of the different proposed setups.

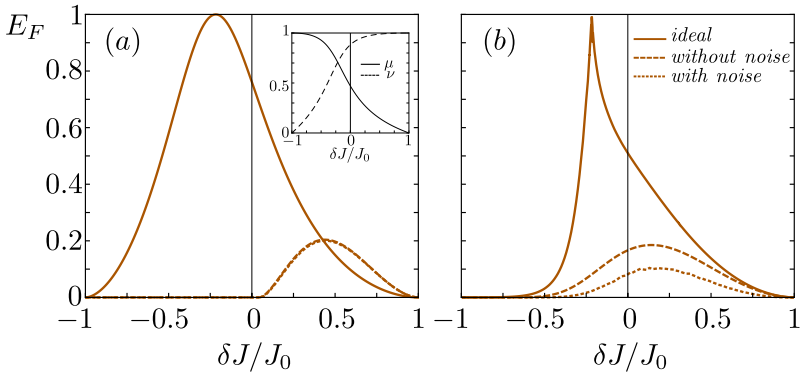

FIGURE 7.7. Steady-state entanglement quantified via the E_F for the two QH-based proposals as a function of δJ. (a) and (b) are based on Eqs. (7.26) and (7.29), respectively. The solid lines refer to the ideal result, where the peak is reached for $\mu = \nu$ (see inset). The dashed lines also take into account the undesired terms, described by $\mathscr{L}^{(i)}_{\text{n-id}}$, while the dotted lines in addition account for nuclear dephasing (see text). Numerical parameters: $\gamma_{\text{L}} = \gamma = 30\mu$eV, $J_0 = 3\mu$eV and $\delta_i \in (-2,2)\mu$eV. In (b), for each value of δJ, Ω_i has been optimized in the range $\Omega_i \in (0-50)$neV.

7.4.1 QH edge states

Both Eqs. (7.26) and (7.29) potentially recover the ideal entanglement-generating dynamics given in Eqs. (2.19) and (2.20), respectively, up to undesired terms absorbed into $\mathscr{L}^{(i)}_{\text{n-id}}$. We now turn to the central question of whether the entanglement inherent to the ideal dynamics can prevail in a realistic scenario. Due to the presence of the nonideal terms, even without further decoherence mechanisms, the steady states of Eqs. (7.26) and (7.29) are mixed. We confirm and quantify its entanglement using the entanglement of formation E_F (see Appendix D) [243]. As shown in Fig. 7.7, for a broad range of coupling parameters ($J_{1(2)} = J_0 \mp \delta J$) the generation of steady-state entanglement persists in the two schemes even in the presence of the undesired terms $\mathscr{L}^{(i)}_{\text{n-id}}$.

These results are based on the previous adiabatic elimination of ancilla QDs. To check the validity of our perturbative treatment, in Fig. 7.8 we compare the entanglement in the steady state resulting from the full master equation including ancilla QDs to the Eqs. (7.26) and (7.29), i.e., after adiabatic elimination. For the experimentally achievable parameters $\gamma = 30\mu$eV and $J_0 = 3\mu$eV the agreement is very good, showing that the approximation is valid for physically achievable conditions and it is possible to work with the simplified effective master equation for the system spins. Obviously, the approximation becomes less accurate for larger values of the coupling J_0 with respect to γ (not shown).

In order to obtain sizable steady-state entanglement (which arises from nonlocal second-order effects $\sim J^2$), the first-order contributions $\sim J$ have to be canceled via local magnetic fields as described above. For $\gamma_{\text{L}} = \gamma$, the Zeeman energies δ_i are typically of the order of (or smaller than) the Heisenberg coupling strengths J_i (i.e., typically a few μeV). Using for example nanomagnets,

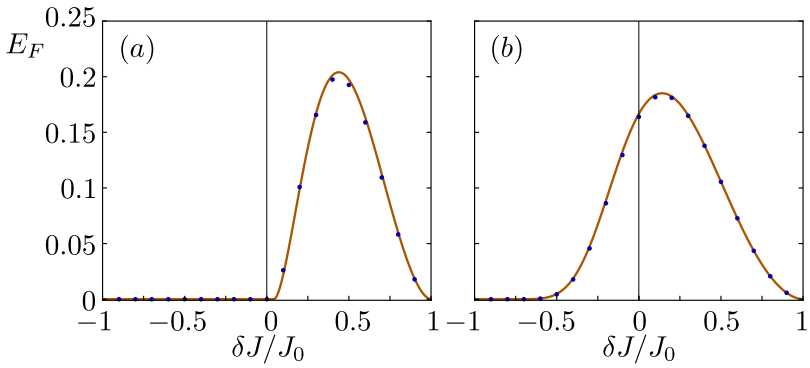

FIGURE 7.8. Steady-state entanglement between two remote qubits quantified via the E_F for the two QH-based proposals as a function of δJ. The solid lines in (a) and (b) refer to Eqs. (7.26) and (7.29), respectively, while the blue dots are calculated with the full master equation including ancilla QDs in order to check the validity of our perturbative treatment. Numerical parameters: $\gamma_L = \gamma = 30\mu$eV, $J_0 = 3\mu$eV and $\delta_i \in (-2,2)\,\mu$eV. In (b), for each value of δJ, Ω_i has been optimized in the range $\Omega_i \in (0-50)$neV.

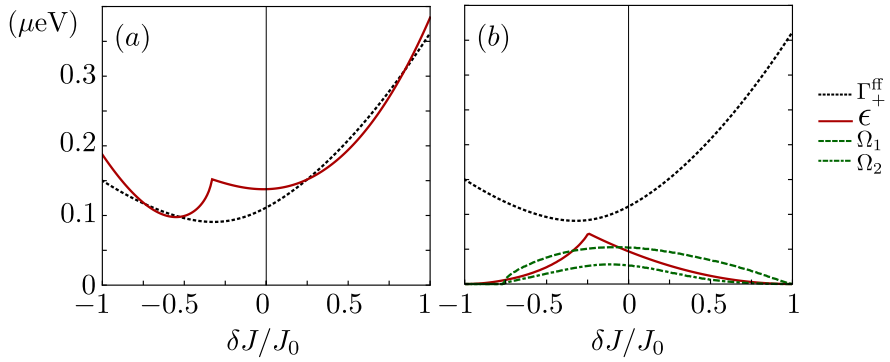

FIGURE 7.9. Spectral gap of the dissipative dynamics (continuous red line) and dominating rate $\Gamma_+^{\rm ff}$ (dotted black line) as a function of δJ. (a) and (b) are based on Eqs. (7.26) and (7.29), respectively. Numerical parameters: $\gamma_L = \gamma = 30\mu$eV, $J_0 = 3\mu$eV and $\delta_i \in (-2,2)\,\mu$eV. In (b), for each value of δJ, Ω_i (green lines) have been optimized in the range $\Omega_i \in (0-50)$neV.

gradients of this size can be readily achieved (e.g., in GaAs by local magnetic fields of a few 100mT) [236, 237].

Another important question is how long it approximately takes for the system to reach its steady state. This time scale is directly related to the spectral gap of the corresponding dissipative dynamics, which is shown in Fig. 7.9 for the two QH-based proposals. The spectral gap is found to be proportional to J_0^2/γ, which can be increased for small values of γ, provided that the conditions for adiabatic elimination ($J_0 \ll \gamma$) are still fulfilled. For the parameters $\gamma = 30\mu$eV

and $J_0 = 3\mu$eV (for which the adiabatic elimination of the fast degrees of freedom is perfectly valid), we then estimate $\epsilon \sim 0.15\mu$eV and $\epsilon \sim 0.03\mu$eV, respectively (for the values of δJ that maximize the entanglement). Accordingly, the steady state is reached on a very fast time scale of roughly $\sim (5-25)$ns. Any noise sources or imperfections that are slow compared to this very fast, zeroth-order time scale should not affect severely the qualitative and quantitative features of the steady state.

First, this is demonstrated explicitly for qubit dephasing due to nuclear spins in the (GaAs) host environment. As explained in more detail in Appendix G, the hyperfine interaction with the nuclei is modeled in terms of a random, slowly evolving effective magnetic field for the electron spins, yielding an extra Hamiltonian of the same form as Eq. (7.3), where the detuning parameters δ_i are sampled independently from a normal distribution with standard deviation $\sigma_{\rm nuc}$ [31]. The resulting time-ensemble-averaged electron dephasing time $T_2^* = \sqrt{2}/\sigma_{\rm nuc}$ has recently been extended up to $T_2^* \approx 3\mu$s [244]. As shown in Fig. 7.7, already for $T_2^* \approx 30$ns, the purely dissipative scheme is basically unaffected by nuclear noise.

Second, again because of the relatively large spectral gap ϵ, perfect cancellation of the first-order terms $\sim J$ is not strictly required, provided that the residual (uncanceled) magnetic fields Δ_i are small compared to the gap; as shown in Appendix G, typically our scheme can tolerate residual gradients Δ_i of up to $\sim 0.1\mu$eV without severely affecting the generation of steady-state entanglement.

Lastly, in our analysis we have neglected several detrimental effects that may be encountered in an actual experiment, an approximation that we now justify: First, at sufficiently low temperatures T<5K, dispersive effects and scattering out of the edge channel may be neglected for propagation distances $\lesssim 100\mu$m [225]. Nevertheless, in Appendix G we show that even a few percent of losses can be tolerated. Second, dephasing during propagation should be negligible for distances small compared to a characteristic coherence length scale L_ϕ, which we estimate as $L_\phi = v_d T_2^* \approx (10^2 - 10^3)\mu$m for a drift velocity $v_d \approx 10^4$m/s and (due to motional narrowing) extended dephasing time $T_2^* \approx (10-100)$ns [225, 231, 233, 234]. Then, in order to suppress errors due to nonresonant QD energies, these should be controlled with a precision $\lesssim 1\mu$eV [225]. Finally, based on QD experiments [238] where basically 100% bipolar spin-filter efficiency has been demonstrated, we have assumed perfect spin-selective driving. Still, with all these simplifications, the amount of steady-state entanglement that we obtain for a realistic scenario (with continuous ancilla-electron pumping) is modest ($E_F \approx 0.2$) as compared to the idealized cases discussed in Eqs. (2.19) and (2.20), respectively (even though it is still comparable to what has been predicted theoretically for two adjacent QDs [99] and achieved experimentally for two atomic ensembles [70]). As shown below, one can largely circumvent this limitation by considering well-controlled stroboscopic interaction times between system and ancilla QDs (as opposed to the arguably more simple continuous settings with largely fluctuating interaction times).

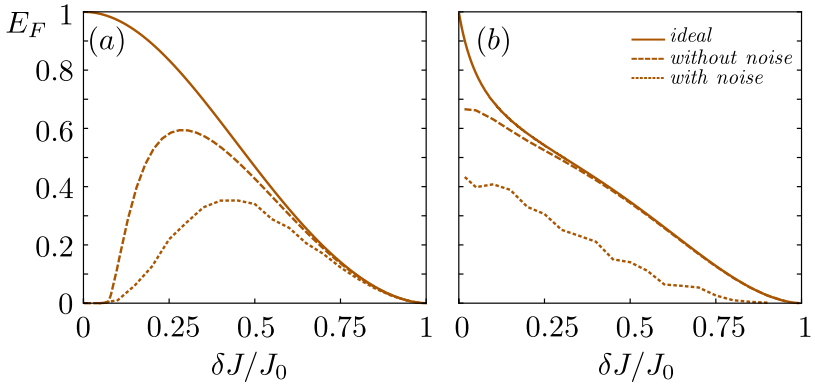

FIGURE 7.10. Steady-state entanglement quantified via the E_F for the two SAW-based proposals as a function of δJ, with $J^{\uparrow}_{1(2)} = J_0 \mp \delta J$. (a) and (b) are based on Eqs. (7.36) and (7.37), respectively. The solid lines refer to the ideal result, given by the lower order terms present in Eqs. (7.36) and (7.37), while the dashed lines correspond to the full evolution. The dotted lines also account for noise due to uncertainty in the dwell times and dephasing. Numerical parameters: $\sigma_\tau = 5\%$, $J_0\tau \approx 0.38$ and $T_2^*/\tau \approx 300$. In (b), for each value of δJ, Ω_i has been optimized in the range $\Omega_i\tau \in (0-1.5)\cdot 10^{-2}$.

7.4.2 SAW moving QDs

The dynamical equations given in Eqs. (7.36) and (7.37) suggest that the system qubits will be driven to an entangled steady state regardless of the initial state (as long as $\tau J \ll 1$). Our analytical results stated above have been confirmed by exact numerical simulations of Eq. (7.32), where the ancilla degrees of freedom have not been eliminated. As demonstrated in Fig. 7.10, the generation of entanglement persists even in the presence of nuclear noise and residual time jitter. We include this noise source by choosing the interaction times τ_i randomly from a Gaussian distribution centered around the average τ with a standard deviation of σ_τ (see Appendix G for a detailed analysis of noise sources). For sufficiently low time jitter and typical dephasing times $T_2^* = (30-300)$ns, we find $E_F \gtrsim 0.4$, which extends up to $E_F \gtrsim 0.7$ for $T_2^* \approx 1\mu$s. Typically, the steady state is reached after $\sim 10^3$ iterations, that is, within $\sim (0.1-1)\mu$s for $\tau \approx (0.1-1)$ns. We have also checked numerically that perfect cancellation of the first-order terms is not strictly required (for details see Appendix G); accordingly, residual gradients of up to $\sim 0.03\mu$eV can be tolerated without severely affecting our results.

The ideal, analytical result given in Eq. (7.36) assumes the injection of alternating spin components of the form $\uparrow,\downarrow,\uparrow,\ldots$. However, this condition can be relaxed to longer sequences of aligned ancilla spins, of the form $\uparrow,\uparrow,\ldots,\downarrow,\downarrow,\ldots,\uparrow,\uparrow,\ldots$. This has been confirmed numerically in Fig. 7.11. Accordingly, the switching times of the gates can be increased by about an order of magnitude without severely affecting the amount of steady-state entanglement.

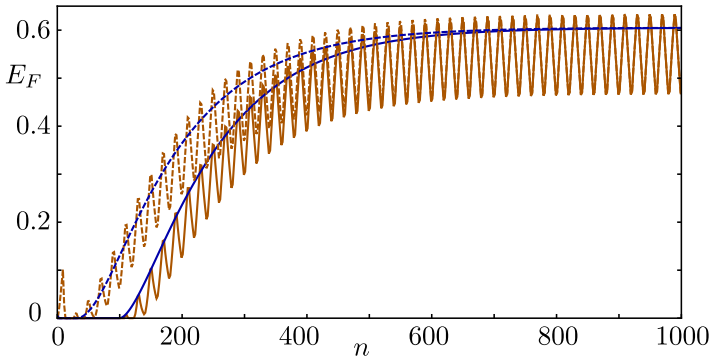

FIGURE 7.11. Steady-state entanglement quantified via the E_F for the SAW-based proposal corresponding to Eq. (7.36) as a function of time ($t = 2n\tau$) for two different initial states (continuous and dashed lines, respectively). Blue: Alternating spins. Orange: Alternating sequences of ten spins. Numerical parameters: $\delta J/J_0 = 0.28$ and $J_0\tau \approx 0.38$.

7.4.3 Comparison of the setups

The presented proposals based on QH edge states constitute continuous entangling generating setups in the sense that once the setup has been prepared there is no need to interact externally with the system before the entanglement measurement. Moreover, they have been shown to drive the system to the steady state on very fast time scales (in a matter of few ns). However, this (arguably simple) continuous setting comes with the disadvantage of undesired terms in the master equations (7.26) and (7.29). As a consequence, even in the cleanest setup, we cannot go beyond a steady-state entanglement of $E_F \approx 0.2$. As evidenced by our stroboscopic SAW-based scheme, this limitation can be overcome by suitably controlling the electron dwell times τ_i in the ancilla QDs. In this way, the effective dynamics given in Eqs. (7.36) and (7.37) can be ensured to approach the ideal ones (by controlling the dwell times τ_i). Therefore, in the limit $\tau_i \to 0$ and without noise sources, we would recover the pure entangled steady states of Eqs. (2.19) and (2.20) and could approach *perfect* entanglement ($E_F = 1$). Here, we estimate an upper limit of $E_F \approx 0.7$ when accounting for typical experimental parameters and imperfections. This better performance comes with the experimental challenge to transport many electrons via (for example) the SAW-created potentials reliably and with accurate (electrical) control of the electronic dwell times. Moreover, the proposal with alternating spin sequences comes with further requirements as the proper spin-filtering synchronized with the exchange couplings. However, based on recent progress demonstrated for single-electron transport experiments with SAW moving QDs [232, 233, 235] and the robustness against errors (as we demonstrate here) a future, successful experimental realization of our scheme should be feasible.

Given the additional experimental challenges for an accurate control of the ancilla electron dwell times τ_i with synchronized (electrical) control of the Heisenberg coupling constants, one

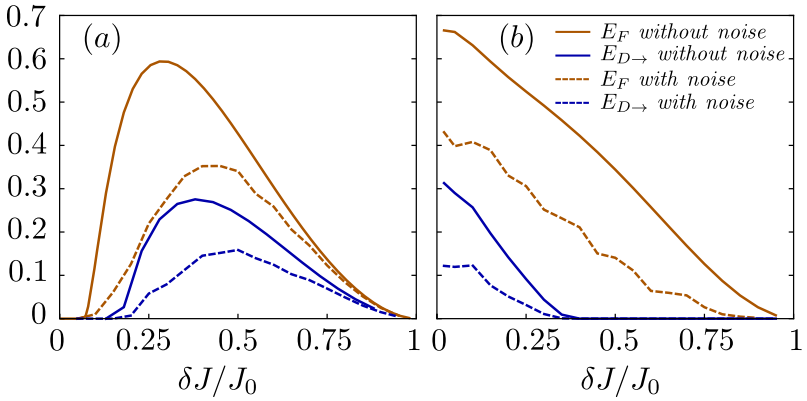

FIGURE 7.12. Upper and lower bounds of distillable entanglement in the steady state quantified via the E_F (orange) and $E_{D\rightarrow}$ (blue) for the two SAW-based proposals as a function of δJ, with $J^{\uparrow}_{1(2)} = J_0 \mp \delta J$. (a) and (b) show results based on Eqs. (7.36) and (7.37), respectively. The solid lines correspond to the full evolution, while the dashed lines account for noise due to uncertainty in the dwell times and nuclear dephasing. Numerical parameters: $\sigma_\tau = 5\%$, $J_0\tau \approx 0.38$ and $T_2^*/\tau \approx 300$. In (b), for each value of δJ, Ω_i has been optimized in the range $\Omega_i\tau \in (0-1.5)\cdot 10^{-2}$.

may wonder whether the increase in obtainable steady-state entanglement (in the stroboscopic SAW-based schemes) is worth the effort. This, of course, depends on the ultimate purpose of entanglement generation. When viewing entanglement production mainly as an experimental benchmark to demonstrate the capability to entangle, any entanglement measure (such as our canonical choice, the entanglement of formation E_{F}) would do; any state with nonzero E_F can be shown (in principle) to be entangled either by measuring a suitable entanglement witness or by sufficiently precise state tomography. However, E_F will not tell us, in general, how useful the state is for subsequent QIP tasks. Since most applications of entanglement require almost pure states, one of the most relevant uses of mixed-state entanglement is as an input to entanglement distillation protocols [245, 246]. Usefulness for such a task is measured by distillable entanglement [247] $E_D(\rho)$, which quantifies how many pure Bell states can be obtained from many copies of ρ by local operations and classical communication (per copy and in the limit of many copies). While $E_D(\rho) > 0$ for all entangled states of two qubits, in general only upper and lower bounds are known. We use $E_{D\rightarrow}$, the entanglement that can be distilled using only one-way communication and which is given by [248] $E_{D\rightarrow}(\rho) = \max\{0, S(\rho_1) - S(\rho), S(\rho_2) - S(\rho)\}$, where S is the von Neumann entropy and ρ_i the reduced state at site $i = 1,2$. Using this lower bound we find that the steady states in the *continuous* QH-based protocols are too noisy to contain meaningful one-way distillable entanglement ($E_{D\rightarrow}(\rho_s) < 0.01$), while the *stroboscopic* SAW-based schemes produce $E_{D\rightarrow}$ around $0.1 - 0.2$, cf. Fig. 7.12, showing that from a supply of $5n - 10n$ such pairs we can distill n high-fidelity Bell states which would, in turn, allow for, e.g., quantum teleportation or remote gate implementation. Similar considerations should

apply for stroboscopic QH-based settings with accurate control over the electron dwell times, as experimentally demonstrated for example in Ref. [227] .

7.5 Conclusions

To conclude, we have presented a general scheme for the deterministic generation of entanglement between spins confined in spatially separated gate-defined QDs. We have detailed our ideas for two specific electron-based setups feasible with current state-of-the-art technology, for which the coherence length of the corresponding quantum channels should allow us to generate sizable entanglement ($E_F \approx 0.2-0.7$) over distances of up to 100μm. While such noisy, modestly entangled two-qubit states can be used, e.g., for quantum teleportation, their main use lies in the fact that they can be distilled into highly entangled states by means of local operations on several copies [245, 249]. We have seen, in particular, that the stroboscopic schemes generate a sizable amount of distillable entanglement. Running our steady-state scheme on several spin qubits in parallel could provide deterministic inputs to such a distillation procedure.

We have focused on GaAs-based systems, as these have been investigated most thoroughly in experiments, with the ambient nuclei posing one of the dominant sources of undesired noise. Two complementary strategies to address the role of nuclear spins in future studies would be (i) either to investigate nuclear-spin-free systems with $T_2^*>100\mu$s [250, 251] or (ii) to associate the Heisenberg coupling (7.1) with the hyperfine interaction between ancilla electron spins and collective nuclear spin operators, with (possibly large) collective spin operators $\mathbf{I}_i$ ($i=1,2$) replacing the spin-1/2 system electron spins $\mathbf{S_i}$ considered in this work. By carefully choosing the spin-projection of the injected ancilla spins as well as the interaction times between electron and nuclear spins via the dwell times of the ancilla electrons in the QDs, one should be able to engineer a dissipative master equation of the form given in Eq. (2.19), again with the replacement $\mathbf{S}_i \rightarrow \mathbf{I}_i$. Since nuclear spin ensembles typically comprise 10^4-10^6 nuclei, this scheme could possibly generate large amounts of entanglement over mesoscopically large distances, provided that narrowed nuclear spin states with a width much smaller than the average polarization are prepared initially [98].

Conclusions and outlook

Although the full control of quantum technologies remains a future goal, a good progress is ongoing. This thesis covers various examples of techniques that one can envision to apply to the field. We have classified them in two types: driving periodically and engineering by dissipation. In this way, periodically driven (or Floquet) closed systems have been the subject of study in chapters 3 and 4, while they have been used as a resource for experimental tunability to achieve an interesting current blockade effect in chapter 6. To go beyond the current, we have developed in chapter 5 a method to compute the full-counting statistics (FCS) in general conductors. Finally, the work in chapter 7 utilizes dissipative engineering as a resource for entanglement.

More concretely, in chapter 3 we have provided a topological classification for a model with topological superconductivity subject to different monochromatic driving protocols. The main result to emphasize is that, by using Floquet theory, one can understand the topological phase diagram beyond the high-frequency regime. Another interesting result is the finding of long-range effective interactions under specific driving conditions, which might give rise to massive edge modes as predicted in Ref. [252]. Although the Majorana bound states that one can find in short arrays of quantum dots (QDs) are not topologically protected as in a topological superconductor, in chapter 4 we focused on arrays of 2 or 3 driven QDs and analyzed situations where the driving fields are essential to tune these kind of boundary modes.

In chapter 5 we have developed a method to compute efficiently the FCS of charge transport through time-dependent conductors and we have applied it to a few problems of recent interest to generalize results for the current or the shot noise to higher-order cumulants. A possible extension could be the generalization of this method to non-zero frequency noise or non-Markovian problems.

In chapter 6.1 we have described an interesting phenomena named edge-state blockade that occurs in a transport setup with a dimerized central conductor due to the existence of topological edge states. As this effect is mainly visible in the value of the current noise, we propose noise measurements to detect nontrivial topological phases. The main limitation of the model studied so far is that it considers only the one-electron subspace, therefore it would be valuable to take more electrons into account. The other experimental limitation is the difficulty to tune the conductor across the phase transition, which has been settled in chapter 6.2 with the demonstration that this edge-state blockade can also be induced by an oscillating field.

Finally, in chapter 7 we have engineered the proper environment for two spin-qubits defined in spatially separated semiconductor QDs such that dissipation drives them to an entangled steady state. The formation of such long-range correlations would be an important step towards a semiconductor-based quantum information processing architecture. One can think of the use of a similar setup to create entanglement between separated nuclear ensembles, which might provide longer coherence times for the quantum operations and possibly greater amount of entanglement.

Conclusiones y perspectiva

Aunque un control total sobre las tecnologías cuánticas es aún un objetivo del futuro, un buen progreso está en curso. Esta tesis cubre varios ejemplos de técnicas que uno puede imaginarse aplicar a este campo. Las hemos clasificado en dos tipos: actuación con campos periódicos y manipulación vía disipación. Así, la manipulación de sistemas cerrados con campos periódicos es sujeto de estudio en los capítulos 3 y 4, mientras que se usa como un recurso para la implementación experimental de un interesante fenómeno de bloqueo de corriente en el capítulo 6. Para ir más allá de la corriente, en el capítulo 5 hemos desarrollado un método para calcular la estadística de transporte de carga en conductores generales. Finalmente, el trabajo del capítulo 7 emplea el método de ingeniería vía disipación como un recurso para obtener entrelazamiento.

Más concretamente, en el capítulo 3 hemos conseguido clasificar topológicamente un modelo con superconductividad topológica sujeto a diferentes protocolos de manipulación periódica. El principal resultado es que, usando teoría de Floquet, somos capaces de entender este diagrama de fases topológicas más allá del límite de alta frecuencia. Otro resultado interesante es que, bajo condiciones determinadas, encontramos interacciones efectivas de largo alcance, lo que podría dar lugar a estados de borde masivos como los descubiertos en la Ref. [252]. Aunque los estados de borde de tipo Majorana que uno puede encontrar en cadenas cortas de puntos cuánticos no tendrían protección topológica como en un superconductor topológico, en el capítulo 4 nos centramos en cadenas de 2 y 3 puntos cuánticos forzados con campos periódicos y analizamos situaciones en las que éstos son esenciales para generar estados de bordes de tipo Majorana.

En el capítulo 5 hemos presentado un método para calcular de manera eficiente la estadística de transporte de electrones a través de un conductor con dependencia temporal y lo hemos aplicado a algunos problemas de interés reciente, donde hemos generalizado resultados para la corriente ó la varianza a cumulantes de orden más alto. Una posible extensión de este trabajo podría ser la generalización de tal método al ruido de frecuencia finita ó a problemas no Markovianos.

En el capítulo 6.1 hemos descrito un fenómeno llamado bloqueo por estados de borde, el cual ocurre en un dispositivo de transporte con un conductor dimerizado debido a la existencia de estados de borde topológicos. Como este efecto es principalmente visible en el ruido de la corriente, proponemos medidas del ruido para la detección de fases topológicas no triviales. La principal limitación del modelo estudiado es que considera sólo el subespacio de un electrón, por lo que sería interesante tener en cuenta más electrones en el cálculo. La otra limitación experimental es la dificultad para tunear el conductor para inducir la transición de fase. Ésta ha sido resuelta en el capítulo 6.2 con la demostración de que el bloqueo por estados de borde se puede inducir con un campo oscilante.

Finalmente, en el capítulo 7 hemos encontrado el entorno para dos qubits, definidos en espines situados en puntos cuánticos semiconductores separados espacialmente, tal que la disipación los conduce a un estado estacionario entrelazado. La formación de estas correlaciones cuánticas a largo alcance constituiría un paso importante hacia una arquitectura para el procesamiento

de información cuántica basada en semiconductores. Uno puede pensar en el uso de un dispositivo similar para generar entrelazamiento a distancia entre conjuntos de espines nucleares, lo que proporcionaría tiempos de coherencia mayores para las operaciones cuánticas a realizar y posiblemente mayor cantidad de entrelazamiento.

APPENDIX A

HIGH-FREQUENCY EXPANSIONS

As we envisioned in the introduction, periodic driving provides with a tool to *engineer* interesting systems since the behavior of a time-periodic problem, $H(t+T) = H(t)$, at times given by an integer number of periods $t = mT$ (stroboscopic dynamics) corresponds to the behavior of a static problem with an effective Hamiltonian H_{eff}. This approach to solve a time-periodic problem provides a better understanding of the results than a numerical resolution, i.e., than simply diagonalizing the numerically constructed one-period time-evolution operator, because it allows to obtain an analytical expression for the effective dynamics. Not only the stroboscopic dynamics (effective Hamiltonian) but also the intra-period dynamics can be determined analytically. However, we restrict ourselves here to the obtention of the effective Hamiltonian since we are mainly interested in the spectrum of quasienergies in this thesis.

If the frequency of the driving $\omega = 2\pi/T$ is very large compared to the typical system energies, it is intuitive to think that the system feels an average of the time-dependent Hamiltonian since it is not able to follow the details. Therefore, for every high-frequency expansion

$$H_{\text{eff}} = \sum_{p=0}^{\infty} \frac{1}{\omega^p} H_{\text{eff}}^{(p)} \tag{A.1}$$

that one constructs to determine the effective Hamiltonian, the zeroth order term must be (see Ref. [253] for an analysis of some exceptions)

$$H_{\text{eff}}^{(0)} = \frac{1}{T} \int_0^T H(t) dt \ . \tag{A.2}$$

The obtention of the subsequent terms is more involved and requires the decomposition of the time-periodic Hamiltonian $H(t)$ into Fourier components

$$H(t) = \sum_{p=-\infty}^{\infty} e^{ip\omega t} H_p \ . \tag{A.3}$$

Moreover, they will depend on the specific choice of the kick operators, in particular the expansion for $H_F^{t_0}$ is slightly different to the expansion for H_F (see Eqs. 2.13 and 2.12, respectively).

The stroboscopic time-evolution operator reads formally

$$U(t_0+T,t_0) = \mathscr{T} e^{-i\int_{t_0}^{t_0+T} H(t')dt'} . \tag{A.4}$$

Using a Taylor expansion to second order, this expression becomes

$$U(t_0+T,t_0) = 1 - i\int_{t_0}^{t_0+T} H(t')dt' - \int_{t_0}^{t_0+T} dt \int_{t_0}^{t} dt' H(t)H(t') . \tag{A.5}$$

By introducing now the decomposition in Fourier components, it is easy to see that the first orders terms of the effective Hamiltonian $H_F^{t_0}$ corresponding to the Floquet-Magnus expansion are

$$H_F^{t_0(0)} = H_0 ; \tag{A.6}$$

$$H_F^{t_0(1)} = \sum_{p\neq 0} \frac{1}{p}\left(H_p H_{-p} + e^{ip\omega t_0}\left[H_0, H_p\right]\right) . \tag{A.7}$$

This expansion to first order, then, has a t_0-dependence that should not be there since the quasienergies cannot depend on the choice of the initial time. This problem, due to a mismatch between the order of appearance and the order of contribution to the quasienergy spectrum, is solved in the other introduced expansion, called van Vleck expansion. In fact, the first order terms of the effective Hamiltonian H_F are [74]

$$H_F{}^{(0)} = H_0 ; \tag{A.8}$$

$$H_F{}^{(1)} = \sum_{p\neq 0} \frac{H_p H_{-p}}{p} ; \tag{A.9}$$

$$H_F{}^{(2)} = \sum_{p\neq 0}\left(\frac{[H_{-p},[H_0,H_p]]}{2p^2} + \sum_{p'\neq 0,p} \frac{[H_{-p'},[H_{p'-p},H_p]]}{3pp'}\right) . \tag{A.10}$$

What is more important for us is the question whether this series converges for a finite number of terms. Several authors have analyzed this problem from a mathematical point of view and a summary can be found in [75]. The conclusion is that this expansion for the effective Hamiltonian converges as long as

$$\int_0^T ||H(t)||dt < \pi , \tag{A.11}$$

where $||H(t)||$ is the euclidean norm of the Hamiltonian, defined as the squared root of the largest eigenvalue of the positive semidefinite operator $H(t)^2$. Note here that the convergence of the total expansion, including the kick operators, has a smaller radius of convergence [75]. As explained in Ref. [253], if the series does not converge one may have chaotic dynamics, in single-particle problems, or heating to infinite temperatures, for many-particle systems. But those cases are out of the scope of this thesis.

APPENDIX B

MASTER EQUATION MICROSCOPIC DERIVATION

In this appendix we provide with a microscopic derivation of the quantum master equation starting with the Hamiltonian dynamics of the total system and tracing out the degrees of freedom of the environment. Under certain assumptions, the dynamical equation is time-local and with constant coefficients, which implies that the most general evolution that preserves the properties of the density matrix is given by a Lindblad form master equation. We need then a further assumption to derive such Lindblad dissipators. The conditions considered in this appendix are not the only ones which provide with a Lindblad equation but they are the ones typically fulfilled in the physical systems considered along this thesis (see [184] for more solvable cases).

If the total system consists in a central system with Hamiltonian H_S, the leads (or baths) with Hamiltonian H_B and the interaction between them, described by the Hamiltonian H_I, the evolution of the density matrix that describes the state of the total system is given by the von Neumann equation in the interaction picture

$$\dot{\mathscr{W}}(t) = -i\,[H_I(t), \mathscr{W}(t)] \ . \tag{B.1}$$

By inserting the formal solution of this equation again into the right hand side and tracing over the bath we obtain

$$\dot{\varrho}(t) = \mathrm{tr}_{\mathrm{B}}\,\dot{\mathscr{W}}(t) = -\int_0^t dt'\,\mathrm{tr}_{\mathrm{B}}\left[H_I(t), \left[H_I(t'), \mathscr{W}(t')\right]\right] \ , \tag{B.2}$$

where we have defined the reduced density matrix of the central system as $\varrho = \mathrm{tr}_{\mathrm{B}}\,\mathscr{W}$ and we have chosen the interaction Hamiltonian such that $\mathrm{tr}_{\mathrm{B}}\,[H_I(t), \mathscr{W}(0)] = 0$ (see below).

In order to obtain a closed equation for the reduced density matrix, we perform a first approximation, called *Born approximation*, which assumes that the influence of the central

system on the reservoir is small. The excitations in the environment decay very fast (bath correlation time τ_{B} small) in such a way that the state of the total system may be approximately characterized by $\mathscr{W}(t) = \varrho(t) \otimes \rho_B$. If the coupling is stronger, one can also go to higher order [254]. To show that the condition $\mathrm{tr}_{\mathrm{B}}[H_I(t), \mathscr{W}(0)] = 0$ can be always satisfied, let us consider the general expression for the interaction Hamiltonian (already in the interaction picture)

$$H_I(t) = \sum_{\alpha} A_\alpha(t) \otimes B_\alpha(t) \ , \tag{B.3}$$

where A_α are system operators, while B_α are bath operators. A simple way to fulfill the given condition is redefining H_S such as $\mathrm{tr}_{\mathrm{B}}\{B_\alpha(t)\rho_B\} = 0$. To get more insight into the meaning of our next approximation, let us rewrite the closed equation by using the general expression for the interaction Hamiltonian Eq. (B.3). After a step of simple algebra it reads

$$\dot{\varrho}(t) = -\sum_{\alpha,\beta} \int_0^t dt' \left\{ C_{\alpha,\beta}(t,t') \left[A_\alpha(t), A_\beta(t') \varrho(t') \right] + C_{\beta,\alpha}(t',t) \left[\varrho(t') A_\beta(t'), A_\alpha(t) \right] \right\} \ , \tag{B.4}$$

with the correlation functions of the bath

$$C_{\alpha,\beta}(t,t') = \mathrm{tr}_{\mathrm{B}}\{B_\alpha(t) B_\beta(t') \rho_B\} \ . \tag{B.5}$$

As these correlation functions usually depend only on the difference of times, it is useful to redefine them as $C_{\alpha,\beta}(t-t') \equiv C_{\alpha,\beta}(t,t')$ and to substitute the variable t' by $t-t'$ in Eq. (B.4) obtaining

$$\dot{\varrho}(t) = -\sum_{\alpha,\beta} \int_0^t dt' \left\{ C_{\alpha,\beta}(t') \left[A_\alpha(t), A_\beta(t-t') \varrho(t-t') \right] + C_{\beta,\alpha}(-t') \left[\varrho(t-t') A_\beta(t-t'), A_\alpha(t) \right] \right\} \ . \tag{B.6}$$

Another general property of the correlation functions is that they are maximum at zero and decay relatively fast. Therefore the so called *Markov approximation*, which consists in substituting the reduced density matrix at previous times $\varrho(t-t')$ by the local one $\varrho(t)$, is going to be a good approximation as long as the correlations decay is fast enough compared to the time evolution of this reduced density matrix (relaxation time τ_{R} large). For the same reason, one can extend the upper integration limit to infinity, obtaining a time-local equation with constant coefficients, which reads

$$\dot{\varrho}(t) = -i \left[H_I, \varrho(t) \right] - \sum_{\alpha,\beta} \int_0^\infty dt' \left\{ C_{\alpha,\beta}(t') \left[A_\alpha, e^{-iH_S t'} A_\beta e^{iH_S t'} \varrho(t) \right] + C_{\beta,\alpha}(-t') \left[\varrho(t) e^{-iH_S t'} A_\beta e^{iH_S t'}, A_\alpha \right] \right\} \ , \tag{B.7}$$

already in the original Schrödinger picture, where it is more clear the time independence of the coefficients.

However, to obtain a Lindblad type master equation, a further approximation is required: *secular or rotating-wave approximation*. This approximation involves an averaging over the rapidly oscillating terms in the master equation. To see this time dependence, one works in the eigenbasis of the system Hamiltonian and choose hermitian coupling operators A_α, B_α (which

is always possible due to the hermitivity of the interaction Hamiltonian). Let us denote the eigenvalues of H_S by ϵ and the projection onto the eigenspace belonging to the eigenvalue ϵ by $\Pi(\epsilon)$. Then we can define the operators

$$A_\alpha(\omega) = \sum_{\epsilon-\epsilon'=\omega} \Pi(\epsilon) A_\alpha \Pi(\epsilon') \,, \tag{B.8}$$

where the sum is extended over all energies ϵ and ϵ' with a fixed energy difference of ω. After involved steps one can derive finally the Lindblad type master equation

$$\dot{\varrho}(t) = -i\left[H_S + H_{LS}, \varrho(t)\right] + \sum_\omega \sum_{\alpha,\beta} \frac{\gamma_{\alpha,\beta}(\omega)}{2} \left(2A_\beta(\omega)\varrho(t)A_\alpha^\dagger(\omega) - A_\alpha^\dagger(\omega)A_\beta(\omega)\varrho(t) - \varrho(t)A_\alpha^\dagger(\omega)A_\beta(\omega)\right) \,, \tag{B.9}$$

where H_{LS} is often called Lamb-shift Hamiltonian since it leads to a renormalization of the energy levels due to the coupling to the bath and reads

$$H_{LS} = \sum_\omega \sum_{\alpha,\beta} S_{\alpha,\beta}(\omega) A_\alpha^\dagger(\omega) A_\beta(\omega) \,, \tag{B.10}$$

where the functions $\gamma_{\alpha,\beta}$ and $S_{\alpha,\beta}$ are defined via the following decomposition of the Fourier transforms of the bath correlation functions

$$\gamma_{\alpha,\beta}(\omega) = C_{\alpha,\beta}(\omega) + C_{\beta,\alpha}^*(\omega); \quad S_{\alpha,\beta}(\omega) = \frac{1}{2i}\left(C_{\alpha,\beta}(\omega) - C_{\beta,\alpha}^*(\omega)\right); \tag{B.11}$$

where

$$C_{\alpha,\beta}(\omega) = \int_0^\infty dt' e^{i\omega t'} C_{\alpha,\beta}(t') \,. \tag{B.12}$$

This last approximation is valid whenever the inverse frequency differences involved in the problem ($|\omega - \omega'|^{-1}$) are small compared to the relaxation time of the system. The equation (B.9) is still not in Lindblad form but it can be written like that just by simple diagonalization of the quadratic forms.

To sumarize, we have performed three approximations and the regime of validity is the following:

- The central system does not affect to the bath statistics because the interaction is weak, compared to the bath correlation time.
- The bath correlations decay very fast compared to the relaxation time of the central system $\tau_\mathrm{B} \ll \tau_\mathrm{R}$.
- The inverse frequency differences (for $\omega \neq \omega'$) are small compared to the relaxation time of the central system $|\omega - \omega'|^{-1} \ll \tau_\mathrm{R}$.

The environment in our cases of study consists of a few leads each modeled as a free electron gas, therefore the Hamiltonian of the bath is

$$H_\mathrm{B} = \sum_{k,l} \epsilon_{k,l} f_{k,l}^\dagger f_{k,l} \,, \tag{B.13}$$

where the operator $f_{k,l}$ annihilates an electron in the kth mode of lead l and $\epsilon_{k,l}$ is the energy of that mode. Finally, let us investigate a particular choice of the coupling operators between central system and environment, i.e., a particular interaction Hamiltonian. To simplify we assume that the central system is a group of quantum dots (QDs) and that one of them (j) is tunnel-coupled to a lead via the coupling Hamiltonian

$$H_I = \sum_k \tau_k d_j^\dagger f_k + \tau_k^* f_k^\dagger d_j \ , \tag{B.14}$$

where f_k annihilates an electron in the kth mode of this lead and d_j annihilates an electron in the QD. By defining the hermitian coupling operators $A_1 = (d_j + d_j^\dagger)/2$, $A_2 = -i(d_j - d_j^\dagger)/2$, $B_1 = \sum_k (\tau_k f_k + \tau_k^* f_k^\dagger)$ and $B_2 = -i\sum_k (\tau_k f_k - \tau_k^* f_k^\dagger)$ this interaction Hamiltonian can be rewritten in the desired form

$$H_I = \sum_{\alpha=1,2} A_\alpha \otimes B_\alpha \ . \tag{B.15}$$

Now, we can compute the correlation functions of the bath, $C_{\alpha,\beta}(t') = \mathrm{tr_B}\left\{B_\alpha(t')B_\beta(0)\rho_B\right\}$. Using the definition of the Fermi functions

$$N(\epsilon_k) = \mathrm{tr_B}\left\{f_k^\dagger f_k \rho_B\right\} = \frac{1}{e^{\beta(\epsilon_k-\mu)}+1}; \quad \bar{N}(\epsilon_k) = \mathrm{tr_B}\left\{f_k f_k^\dagger \rho_B\right\} = \frac{1}{e^{-\beta(\epsilon_k-\mu)}+1} = 1 - N(\epsilon_k) \ ; \tag{B.16}$$

where μ is the chemical potential of the lead and β is the inverse of the temperature. The correlation functions read

$$C_{1,1}(t') = C_{2,2}(t') = \sum_k |\tau_k|^2 \left[\bar{N}(\epsilon_k) e^{-i\epsilon_k t'} + N(\epsilon_k) e^{i\epsilon_k t'}\right] \ ; \tag{B.17}$$

$$C_{1,2}(t') = -C_{2,1}(t') = i\sum_k |\tau_k|^2 \left[\bar{N}(\epsilon_k) e^{-i\epsilon_k t'} - N(\epsilon_k) e^{i\epsilon_k t'}\right] \ . \tag{B.18}$$

According to Eq. (B.11),

$$\gamma_{1,1}(\omega) = \gamma_{2,2}(\omega) = 2\pi \sum_k |\tau_k|^2 \left[\bar{N}(\omega)\delta(\omega-\epsilon_k) + N(\omega)\delta(\omega+\epsilon_k)\right] \ ; \tag{B.19}$$

$$\gamma_{1,2}(\omega) = -\gamma_{2,1}(\omega) = 2\pi i \sum_k |\tau_k|^2 \left[\bar{N}(\omega)\delta(\omega-\epsilon_k) - N(\omega)\delta(\omega+\epsilon_k)\right] \ . \tag{B.20}$$

It is common to define the tunneling rates $\Gamma(\omega) = 2\pi\sum_k |\tau_k|^2 \delta(\omega-\epsilon_k)$ such that

$$\gamma_{1,1}(\omega) = \gamma_{2,2}(\omega) = \left[\bar{N}(\omega)\Gamma(\omega) + N(\omega)\Gamma(-\omega)\right] \ ; \tag{B.21}$$

$$\gamma_{1,2}(\omega) = -\gamma_{2,1}(\omega) = i\left[\bar{N}(\omega)\Gamma(\omega) - N(\omega)\Gamma(-\omega)\right] \ ; \tag{B.22}$$

and diagonalize this matrix to obtain the diagonal Lindblad type master equation that reads

$$\dot{\varrho}(t) = -i\left[H_S + H_{LS}, \varrho(t)\right] \tag{B.23}$$

$$+ \sum_\omega \frac{\bar{N}(\omega)\Gamma(\omega)}{2}\left(2d_j^\dagger(\omega)\varrho(t)d_j(\omega) - d_j(\omega)d_j^\dagger(\omega)\varrho(t) - \varrho(t)d_j(\omega)d_j^\dagger(\omega)\right) \tag{B.24}$$

$$+ \sum_\omega \frac{N(\omega)\Gamma(-\omega)}{2}\left(2d_j(\omega)\varrho(t)d_j^\dagger(\omega) - d_j^\dagger(\omega)d_j(\omega)\varrho(t) - \varrho(t)d_j^\dagger(\omega)d_j(\omega)\right) \ . \tag{B.25}$$

As we can see, every lead contribute to each transition with two Lindblad dissipators. The Lamb-shift is often neglected because the effect is a small renormalization of the energies.

The final simplification that one can do is to consider that the chemical potential of the lead is far from the transition frequencies ω, in such a way that the Fermi functions are all either 1 or 0. This limit is often called *infinite bias* and implies that there is only one dissipator, either Eq. (B.24) or (B.25). Moreover, there is no need to work in the eigenbasis in this cases since $\sum_\omega A_\alpha(\omega) = A_\alpha$. Therefore, the master equation in the infinite bias limit, the one used along this thesis, is finally of the form

$$\dot{\varrho}(t) = -i\left[H_S, \varrho(t)\right] + \frac{\Gamma}{2}\left(2d_j^\dagger \varrho(t) d_j - d_j d_j^\dagger \varrho(t) - \varrho(t) d_j d_j^\dagger\right) , \tag{B.26}$$

if the chemical potential is above the levels (full lead), and

$$\dot{\varrho}(t) = -i\left[H_S, \varrho(t)\right] + \frac{\Gamma}{2}\left(2d_j \varrho(t) d_j^\dagger - d_j^\dagger d_j \varrho(t) - \varrho(t) d_j^\dagger d_j\right) , \tag{B.27}$$

if it is below (empty lead).

APPENDIX C

JORDAN-WIGNER TRANSFORMATION

In this appendix we show the mapping from the one-dimensional XY model to the Kitaev model by a Jordan-Wigner transformation. Due to this correspondence, the results in chapter 3 not only have relevance in the field of topological states of matter, but they also provide insight into quantum magnetism under non-equilibrium situations [255–258]. Apart from a mathematical tool to simplify the analysis, this correspondence sets a different framework to probe the phase transitions.

The Kitaev Hamiltonian in Eq. (3.1)

$$H(t) = \frac{\mu(t)}{2}\sum_{j=1}^{n}\left(2d_j^\dagger d_j - 1\right) - \frac{\tau(t)}{2}\sum_{j=1}^{n}\left(d_j^\dagger d_{j+1} + \text{h.c.}\right) - \frac{\Delta(t)}{2}\sum_{j=1}^{n}\left(d_j^\dagger d_{j+1}^\dagger + \text{h.c.}\right), \tag{C.1}$$

can be exactly mapped onto the Hamiltonian of the driven XY model in an external transverse field

$$H(t) = -\frac{\mu(t)}{2}\sum_{j=1}^{n}\sigma_j^x - \frac{J_z(t)}{2}\sum_{j=1}^{n-1}\sigma_j^z\sigma_{j+1}^z - \frac{J_y(t)}{2}\sum_{j=1}^{n-1}\sigma_j^y\sigma_{j+1}^y \tag{C.2}$$

by means of a Jordan-Wigner transformation [259]. Here, the Pauli matrices describe local spins and are defined in terms of the non-local fermionic operators as

$$\sigma_j^x = 1 - 2d_j^\dagger d_j\,; \tag{C.3}$$

$$\sigma_j^z = d_j^\dagger e^{i\pi\sum_{l<j}d_l^\dagger d_l} + d_j e^{-i\pi\sum_{l<j}d_l^\dagger d_l}\,; \tag{C.4}$$

$$\sigma_j^y = -id_j^\dagger e^{i\pi\sum_{l<j}d_l^\dagger d_l} + id_j e^{-i\pi\sum_{l<j}d_l^\dagger d_l}\,; \tag{C.5}$$

such that they fulfill the commutation relations $[\sigma_\alpha, \sigma_\beta] = 2i\epsilon_{\alpha,\beta,\gamma}\sigma_\gamma$, where $\epsilon_{\alpha,\beta,\gamma}$ is the Levi-Civita tensor. The time-dependent anisotropies are related to the hopping and the superconducting gap as:

$$J_z(t) = \frac{\tau(t) + \Delta(t)}{2}; \quad J_y(t) = \frac{\tau(t) - \Delta(t)}{2}\,. \tag{C.6}$$

In the time-independent case, there is a correspondence between the magnetic phases of the spin system and the topological phases of the fermion model, i.e., the paramagnetic phase is related to the trivial phase, and the ferromagnetic phase corresponds to the nontrivial phase [260]. Under monochromatic driving new magnetic phases arise, corresponding to new topological phases in the fermionic system.

Driving the chemical potential

It is instructive to understand the form of the effective Hamiltonian in Eq. (3.20) in terms of spins chain described by Pauli matrices. After a Jordan-Wigner and discrete Fourier transformation we obtain an effective time-independent XY Hamiltonian [259]

$$\tilde{H}^{\alpha}_{\text{eff}} = -\frac{\mu_{\text{eff}}}{2}\sum_{j=1}^{n}\sigma_j^x - \frac{1}{4}(\tau_0+\Delta_{\text{eff}})\sum_{j=1}^{n-1}\sigma_j^z\sigma_{j+1}^z - \frac{1}{4}(\tau_0-\Delta_{\text{eff}})\sum_{j=1}^{n-1}\sigma_j^y\sigma_{j+1}^y\ . \tag{C.7}$$

Apart from the existence of a paramagnetic phase, the effective anisotropies in Eq. (C.7) can be tuned to generate a ferromagnetic phase in z-direction or y-direction as it is discussed in Ref. [257].

Driving the hopping and BCS pairing

For the driven model considered in chapter 3.3 the Jordan-Wigner transformation provides a mathematical tool to find the effective Hamiltonians in a simple way. After a Jordan-Wigner transformation, this model corresponds to the one-dimensional Ising model in an external magnetic field

$$H(t) = -\frac{\mu_0}{2}\sum_{j=1}^{n}\sigma_j^x - \frac{\tau(t)}{2}\sum_{j=1}^{n-1}\sigma_j^z\sigma_{j+1}^z\ . \tag{C.8}$$

with

$$\tau(t) = \tau_0 + \frac{\tau_1}{2}\cos(\omega t)\ . \tag{C.9}$$

Under the duality transformation [260]

$$\sigma_j^x = \mu_j^z\mu_{j+1}^z;\quad \sigma_j^z = \Pi_{k\le j}\mu_k^x; \tag{C.10}$$

we get what is called the dual Hamiltonian of Eq. (C.8)

$$H^{(\text{D})}(t) = -\frac{\tau(t)}{2}\sum_{j=1}^{N}\mu_j^x - \frac{\mu_0}{2}\sum_{j=1}^{N}\mu_j^z\mu_{j+1}^z\ , \tag{C.11}$$

which is exactly the corresponding Ising model to the system studied in the last section with $\mu(t)\to\tau(t)$ and $\Delta(t)=\tau(t)\to\mu_0$ in Eq. (C.2)—in this case, however, written in terms of the Pauli matrices μ_i^λ. It means that the quasienergy spectrum is the same, and by performing the

inverse duality transformation to the effective Hamiltonians in Eq. (C.7), we obtain the effective Hamiltonians for the new driven system Eq. (C.8). The effective Hamiltonian in spin basis reads

$$\tilde{H}^{\alpha}_{\text{eff}} = -\frac{\tau_{\text{eff}}}{2}\sum_{j=1}^{n-1}\sigma_j^z\sigma_{j+1}^z - \frac{\mu_0}{4}\left[1+J_{-\alpha}\left(\frac{\tau_1}{\omega}\right)\right]\sum_{j=1}^{n}\sigma_j^x + \frac{\mu_0}{4}\left[1-J_{-\alpha}\left(\frac{\tau_1}{\omega}\right)\right]\sum_{j=2}^{n-1}\sigma_{j-1}^z\sigma_j^x\sigma_{j+1}^z\,, \tag{C.12}$$

where $\tau_{\text{eff}} = \tau_0 - \frac{\alpha\omega}{2}$. The first term is a nearest neighbors spin-spin interaction, the second an external magnetic field and the last term a three-spins interaction. The correspondence of the latter after a inverse Jordan-Wigner transformation in the spinless fermion basis is a second-neighbors hopping that will give rise to a new topological phase with larger winding number. It reads exactly

$$\begin{aligned}\tilde{H}^{\alpha}_{\text{eff}} &= \frac{\mu_0}{4}\left[1+J_{-\alpha}\left(\frac{\tau_1}{\omega}\right)\right]\sum_{j=1}^{n}\left(2d_j^\dagger d_j - 1\right) - \frac{\tau_{\text{eff}}}{2}\sum_{j=1}^{n}\left(d_j^\dagger d_{j+1} + d_j^\dagger d_{j+1}^\dagger + \text{h.c.}\right) &\text{(C.13)}\\ &+\frac{\mu_0}{4}\left[1-J_{-\alpha}\left(\frac{\tau_1}{\omega}\right)\right]\sum_{j=2}^{n-1}\left(d_{j-1}^\dagger d_{j+1} + d_{j-1}^\dagger d_{j+1}^\dagger + \text{h.c.}\right)\,. &\text{(C.14)}\end{aligned}$$

When the last term dominates, there are two edge states, as explained in chapter 3.3.

Driving the hopping

Finally, we derive the expression of the long-range Bardeen-Cooper-Schrieffer (BCS) superconducting pairing arising in Eq. (3.40) in terms of Pauli matrices in real space. This allows us to obtain the effective spin model

$$\begin{aligned}\tilde{H}_{\text{eff}} &= -\frac{\mu_0}{2}\sum_{j=1}^{n}\sigma_j^x - \frac{\tau_0}{4}\sum_{j=1}^{n-1}\left(\sigma_j^z\sigma_{j+1}^z + \sigma_j^y\sigma_{j+1}^y\right) &\text{(C.15)}\\ &-\frac{\Delta_0}{4}\sum_{j=1}^{n}\sum_{l=1,3\ldots}^{n} g_l(\tau_1/\omega)\left(\sigma_j^z M_{j,l}^x\sigma_{j+l}^z - \sigma_j^y M_{j,l}^x\sigma_{j+l}^y\right)\,, &\text{(C.16)}\end{aligned}$$

where $M_{j,l}^x = \sigma_{j+1}^x\ldots\sigma_{j+l-1}^x$. Long-range spin interactions are generated by means of the ac driving of the tunneling, which in the spins basis corresponds to a time-periodic anisotropy between Z and Y directions (see Eqs. C.2 and C.6).

APPENDIX D

ENTANGLEMENT OF TWO QUBITS

The entanglement measure used in this work is the entanglement of formation (E_F) [4, 243, 246], defined as the minimum average entanglement of an ensemble of pure states that represents the mixed state ρ. It quantifies the necessary resources to create a given entangled state. For a mixed state ρ of two qubits the concurrence is $\mathscr{C} = \max\{0, \lambda_1 - \lambda_2 - \lambda_3 - \lambda_4\}$, where λ_i are the square roots of the eigenvalues of the matrix $\rho A \rho^* A$ arranged in decreasing order, where A is the antidiagonal matrix with elements $\{-1, 1, 1, -1\}$. For two qubits it ranges from 0 (separable states) to 1 (maximally entangled states). The E_F can be calculated from the concurrence as

$$E_F = -\frac{1+\sqrt{1-\mathscr{C}^2}}{2}\log_2\frac{1+\sqrt{1-\mathscr{C}^2}}{2} - \frac{1-\sqrt{1-\mathscr{C}^2}}{2}\log_2\frac{1-\sqrt{1-\mathscr{C}^2}}{2} \tag{D.1}$$

and also ranges from 0 to 1.

APPENDIX E

FERMIONIC INPUT-OUTPUT FORMALISM

The input-output formalism provides another way to derive the master equation dominating the dynamics of a quantum system connected to macroscopic leads, but it goes beyond that since it allows to deal with travelling wave situations [261]. In this appendix we introduce the *fermionic* input-output formalism [262] and apply it to *cascaded quantum systems*, which consist of quantum nodes connected to a common unidirectional reservoir [263–265].

First of all, we address the interaction of a system with a Markovian reservoir of non-interacting fermions. The total Hamiltonian has the generic system Hamiltonian H_{S}, the bath Hamiltonian

$$H_B = \int_0^\infty d\omega \omega f^\dagger(\omega) f(\omega) \,, \tag{E.1}$$

where ω is the bath energy and $f(\omega)$ are bath fermionic annihilation operators with anticommutation relations $\left[f(\omega), f(\omega')^\dagger\right]_+ = \delta(\omega - \omega')$, and the interaction Hamiltonian

$$H_I = i\int_0^\infty d\omega \sqrt{\frac{\gamma}{2\pi}} \left\{ f^\dagger(\omega) d - d^\dagger f(\omega) \right\} \,, \tag{E.2}$$

where d is a fermionic annihilation operator acting on the system and the coupling to the reservoir is assumed to be independent of the frequency (Markov approximation). The Heisenberg equation of motion of the bath operators is

$$\dot{f}(\omega) = -i\omega f(\omega) + \sqrt{\frac{\gamma}{2\pi}} d \,, \tag{E.3}$$

which can be formally integrated as

$$f(\omega) = e^{-i\omega t} f(\omega, 0) + \sqrt{\frac{\gamma}{2\pi}} \int_0^t dt' e^{-i\omega(t-t')} d(t') \,. \tag{E.4}$$

Here $f(\omega, 0)$ is the value of $f(\omega)$ at time $t = 0$. A general system operator a may commute or anticommute with the bath operators depending on its nature. We call it if even if it commutes

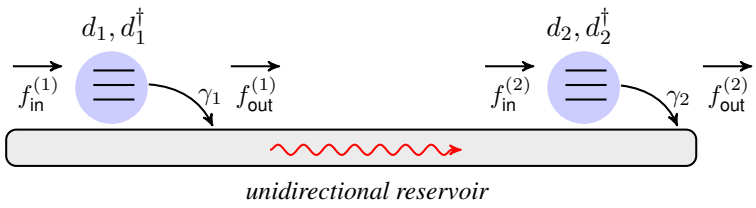

FIGURE E.1. Cascaded quantum system with two nodes connected to a common unidirectional reservoir.

with all bath operators and odd if not. The Heisenberg equation of motion is

$$\dot{a} = -\frac{i}{\hbar}[a, H_S] + \int_0^\infty d\omega \sqrt{\frac{\gamma}{2\pi}} \left\{ \mp f^\dagger(\omega)[a,d]_\pm - \left[a, d^\dagger\right]_\pm f(\omega) \right\} , \tag{E.5}$$

where the top (bottom) signs apply for odd (even) a operator and $[A,B]_\pm = AB \pm BA$. Inserting the expression (E.4) into Eq. (E.5) we derive the quantum Langevin equation

$$\dot{a} = -\frac{i}{\hbar}[a, H_S] \mp \left\{ \sqrt{\gamma} f_{\text{in}}^\dagger(t) + \frac{\gamma}{2} d^\dagger(t) \right\} [a,d]_\pm - \left[a, d^\dagger\right]_\pm \left\{ \sqrt{\gamma} f_{\text{in}}(t) + \frac{\gamma}{2} d(t) \right\} , \tag{E.6}$$

where

$$f_{\text{in}}(t) = \frac{1}{\sqrt{2\pi}} \int_0^\infty d\omega e^{-i\omega t} f(\omega, 0) \tag{E.7}$$

is called noise input field and is determined by the initial state of the bath. The noise output field, defined as the time-reversed evolution from the final time operator $f(\omega, t_f)$, is related to it via

$$f_{\text{out}}(t) - f_{\text{in}}(t) = \sqrt{\gamma} d(t) , \tag{E.8}$$

an identity known as the input-output relation. Up to this point, no assumption has been made concerning the density operator of the bath. We will use the white-noise approximation which assumes the following correlation functions for the input field:

$$\left\langle f_{\text{in}}^\dagger(\omega) f_{\text{in}}(\omega') \right\rangle = \bar{N} \delta(\omega - \omega') ; \quad \left\langle f_{\text{in}}(\omega) f_{\text{in}}^\dagger(\omega') \right\rangle = (1 - \bar{N}) \delta(\omega - \omega') . \tag{E.9}$$

Here $\bar{N}$ is the Fermi distribution function of a thermal reservoir. Moreover we will assume a weak system-reservoir coupling in the sense that the correlation functions of the bath are not affected by the interaction.

As we said above, the input-output formalism provides a powerful treatment for two or more subsystems sharing a common unidirectional reservoir, also known as cascaded quantum systems. Let us consider the case sketched in Fig. E.1: two nodes coupled to the reservoir via Eq. (E.2) with operators $d_j (j = 1,2)$. Following the previous argument a system operator of subsystem j, a_j, follows the Eq. (E.6) with the change $d \to d_j$, $\gamma \to \gamma_j$ and $f_{\text{in}} \to f_{\text{in}}^{(j)}$. The fact that the reservoir is common and unidirectional implies a relation between the output of subsystem 1 and the input in 2. For a dispersion-free channel $f_{\text{in}}^{(2)}(t) = f_{\text{out}}^{(1)}(t - L/v)$, where L is the distance between

the two subsystems and v the group velocity of the reservoir modes, i.e., all the output of the first subsystem is used later as the input into the second one, therefore we are able to write a generic equation for an odd (even) operator as [225]

$$\begin{aligned}\dot{a}(t) &= -\frac{i}{\hbar}[a,H_{\rm S}] \mp \left\{\sqrt{\gamma_1} f_{\rm in}^{\dagger(1)}(t) + \frac{\gamma_1}{2} d_1^\dagger(t)\right\}[a,d_1]_\pm - \left[a,d_1^\dagger\right]_\pm \left\{\sqrt{\gamma_1} f_{\rm in}^{(1)}(t) + \frac{\gamma_1}{2} d_1(t)\right\} \\ &\mp \left\{\sqrt{\gamma_2} f_{\rm in}^{(1)\dagger}(t-L/v) + \frac{\gamma_2}{2} d_2^\dagger(t) + \sqrt{\gamma_1\gamma_2}\, d_1^\dagger(t-L/v)\right\}[a,d_2]_\pm \\ &- \left[a,d_2^\dagger\right]_\pm \left\{\sqrt{\gamma_2} f_{\rm in}^{(1)}(t-L/v) + \frac{\gamma_2}{2} d_2(t) + \sqrt{\gamma_1\gamma_2}\, d_1(t-L/v)\right\} . \end{aligned} \tag{E.10}$$

Since the coupling operators $d_{1,2}$ are fermionic annihilation (odd) operators, they (anti)commute with any (odd) even operator a of the other subsystem. Then it is clear from Eq. (E.10) that the time evolution of an operator of the second subsystem depends on the first one but not the other way around, which reflects the unidirectionality condition. Following [264, 266], for a dispersionless channel, the fixed time delay may be set to zero, i.e., one can choose $L/v = 0^+$ without loss of generality. The previous equation can be easily rewritten as

$$\dot{a}(t) = -\frac{i}{\hbar}\left[a, H_{\rm S} + \frac{i\sqrt{\gamma_1\gamma_2}}{2}\left(d_1^\dagger d_2 - d_2^\dagger d_1\right)\right] - \left[a,d^\dagger\right]_\pm \left\{\frac{d}{2} + f_{\rm in}^{(1)}(t)\right\} \mp \left\{\frac{d^\dagger}{2} + f_{\rm in}^{\dagger(1)}(t)\right\}[a,d]_\pm \tag{E.11}$$

in terms of the nonlocal operator $d = \sqrt{\gamma_1} d_1 + \sqrt{\gamma_2} d_2$. Once we have derived this quantum Langevin equation, we can find a master equation for the partial density operator excluding the bath ϱ by tracing out the bath degrees of freedom from the total density operator $\mathscr{W}$, $\varrho = {\rm tr}_{\rm B}\{\mathscr{W}\}$. For this we make use of the relation ${\rm tr}\{\dot{a}(t)\mathscr{W}\} = {\rm tr}\left\{a\dot{\mathscr{W}}(t)\right\} = {\rm tr}_{\rm s}\left\{a\dot{\varrho}(t)\right\}$. Since any physical state is fully described by the expectation values of even observables (the odd ones have vanishing expectation value due to the parity superselection rule) we can restrict ourselves in Eq. (E.11) to the lower sign for all observables of interest and end up with the master equation

$$\dot{\varrho} = -i\left[H_{\rm S} + \frac{i\sqrt{\gamma_1\gamma_2}}{2}\left(d_1^\dagger d_2 - d_2^\dagger d_1\right), \varrho\right] + \frac{1}{2}\left(1-\bar{N}\right)\mathscr{D}[d]\varrho + \frac{1}{2}\bar{N}\mathscr{D}\left[d^\dagger\right]\varrho\,, \tag{E.12}$$

with the Lindblad dissipator $\mathscr{D}[x]\varrho = 2x\varrho x^\dagger - x^\dagger x\varrho - \varrho x^\dagger x$ and $\bar{N}$ is the Fermi distribution function of the fermionic reservoir. This expression contains the nonlocal coherent and incoherent contributions of the coupling between subsystems mediated by the reservoir. For simplicity we have neglected the spin index in this derivation. Moreover, in the main text we work in a rotating frame such that $H_{\rm S}$ drops out. For that one needs that the energy levels are aligned within γ, otherwise this would generate an undesired rotation of the nonlocal terms in Eq. (E.12) [225].

APPENDIX F

ADIABATIC ELIMINATION

The adiabatic elimination is a useful method when one has a main system weakly coupled to an auxiliary system, which undergoes fast dynamics (given by a Liouvillian $\mathscr{L}_0$). It allows us to determine the effective dynamics of the main system to (in principle) arbitrary order in the interaction [241]. Analogously to the Schrieffer-Wolff transformation for closed systems, it allows us to decouple the slow subspace, given by the steady state of the auxiliary system, i.e., $\mathscr{L}_0\rho_{\mathrm{a}}^{\mathrm{ss}} = 0$ [1], from the fast one. To this end, one defines the projector $\mathscr{P}$ by its action over the total density matrix $\mathscr{P}\varrho = \mathrm{tr}_{\mathrm{a}}\{\varrho\} \otimes \rho_{\mathrm{a}}^{\mathrm{ss}} = \rho \otimes \rho_{\mathrm{a}}^{\mathrm{ss}}$, where we have introduced the reduced density matrix as the trace over the auxiliary system $\rho \equiv \mathrm{tr}_{\mathrm{a}}\{\varrho\}$, and apply it to the total master equation of the form $\dot{\varrho} = (\mathscr{L}_0 + \mathscr{V})\varrho$, where $\mathscr{V}$ is the perturbative part. In this way we can obtain the subsequent orders of the effective Liouville operator expansion that governs the dynamics of the main system ($\dot{\rho} = \mathrm{tr}_{\mathrm{a}}\{L_{\mathrm{eff}}\varrho\}$) [241]. Defining the Laplace transform of $\mathscr{L}_0$ as $\mathscr{L}_0^{-1} = -\int_0^\infty d\tau e^{\mathscr{L}_0\tau}$, one can easily find

$$L_{\mathrm{eff},1} = \mathscr{P}\mathscr{V}\mathscr{P}\,; \tag{F.1}$$

$$L_{\mathrm{eff},2} = -\mathscr{P}\mathscr{V}\mathscr{Q}\mathscr{L}_0^{-1}\mathscr{Q}\mathscr{V}\mathscr{P}\,; \tag{F.2}$$

where $\mathscr{Q} = 1 - \mathscr{P}$ is the projector into the fast subspace. The perturbation $\mathscr{V}$ contains the interaction between the main and auxiliary systems as well as a main-system Hamiltonian, i.e., in general

$$\mathscr{V}\varrho = -i\sum_{m=1}^{N}\left[A_m \otimes S_m, \varrho\right] - i\sum_{m=1}^{N} b_m\left[S_m, \varrho\right]\,. \tag{F.3}$$

[1] We assume that $\mathscr{L}_0$ has a unique steady state $\rho_{\mathrm{a}}^{\mathrm{ss}}$

Here A_m and S_m are auxiliary and main-system operators, respectively, and $b_m \in \mathbb{R}$. The first-order term is

$$\mathrm{tr_a}\left\{L_{\mathrm{eff},1}\varrho\right\} = -i\sum_{m=1}^{N}\left[\langle A_m\rangle_{\mathrm{ss}} S_m,\rho\right] - i\sum_{j=m}^{N} b_m\left[S_m,\rho\right] \ , \tag{F.4}$$

which means that to first order the main system experiences the effect of the mean values of the auxiliary-system operators in the quasisteady state, $\langle A_m\rangle_{\mathrm{ss}} = \mathrm{tr_a}\left\{A_m\rho_{\mathrm{a}}^{\mathrm{ss}}\right\}$, plus the original main-system Hamiltonian. To second order, one can show

$$\mathrm{tr_a}\left\{L_{\mathrm{eff},2}\varrho\right\} = -\sum_{m,l}\mathrm{tr_a}\left\{\delta A_m\mathscr{L}_0^{-1}\delta A_l\rho_{\mathrm{a}}^{\mathrm{ss}}\right\}\left[S_l\rho,S_m\right] - \sum_{m,l}\mathrm{tr_a}\left\{\delta A_m\mathscr{L}_0^{-1}\rho_{\mathrm{a}}^{\mathrm{ss}}\delta A_l\right\}\left[S_m,\rho S_l\right] \ , \tag{F.5}$$

where δA_m are the fluctuations of the auxiliary-system operators: $\delta A_m = A_m - \langle A_m\rangle_{\mathrm{ss}}$. Using the quantum regression theorem

$$\begin{aligned}
\mathrm{tr_a}\left\{\delta A_m e^{\mathscr{L}_0\tau}\left[\delta A_l\rho_{\mathrm{a}}^{ss}\right]\right\} &= \langle\delta A_m(\tau)\delta A_l\rangle_{\mathrm{ss}} \ ; \\
\mathrm{tr_a}\left\{\delta A_m e^{\mathscr{L}_0\tau}\left[\rho_{\mathrm{a}}^{ss}\delta A_l\right]\right\} &= \langle\delta A_l\delta A_m(\tau)\rangle_{\mathrm{ss}} \ ;
\end{aligned} \tag{F.6}$$

and the relation $\langle\delta A_l\delta A_m(\tau)\rangle_{\mathrm{ss}}^{*} = \left\langle\delta A_m^{\dagger}(\tau)\delta A_l^{\dagger}\right\rangle_{\mathrm{ss}}$, Eq. (F.2) reads

$$\mathrm{tr_a}\left\{L_{\mathrm{eff},2}\varrho\right\} = \sum_{m,l}\mathscr{C}\left(A_m,A_l\right)\left[S_l\rho,S_m\right] + \sum_{m,l}\mathscr{C}^{*}\left(A_m^{\dagger},A_l^{\dagger}\right)\left[S_l^{\dagger}\rho,S_m^{\dagger}\right]^{\dagger} \ , \tag{F.7}$$

where we introduce the correlation functions

$$\mathscr{C}\left(A_m,A_l\right) = \mathrm{tr_a}\left\{\delta A_m\mathscr{L}_0^{-1}\delta A_l\rho_{\mathrm{a}}^{\mathrm{ss}}\right\} \ . \tag{F.8}$$

In the specific case under consideration in the main text, $\mathscr{L}_0 = \mathscr{L}_{\mathrm{tr}}$ and $\mathscr{V}\varrho = -i\left[H_{\mathrm{Z}} + H_{\mathrm{IN}},\varrho\right]$.

APPENDIX G

NOISE SOURCES

In this appendix we detail the different noise sources taken into account in the proposed setups for long-distance entanglement generation in chapter 7. First of all, we account for qubit dephasing induced by nuclear spins in the (GaAs) host environment. Second, we consider electron losses due to imperfections in the transport mechanisms. Then, we analyze the effect of an imperfect cancellation of the first-order terms, i.e., the effect of some residual gradient. Finally, in the surface acoustic wave (SAW)-based proposals we account for imperfections due to uncertainties in the effective electron interaction times.

To account for dephasing due to the nuclear spins, we follow the standard treatment [267] and assume that the spins in the quantum dots (QDs) experience non-Markovian noise. The fluctuations of the Overhauser field lead to a time-ensemble-averaged electron dephasing time T_2^*, that is related to the width of the nuclear field distribution σ_{nuc} as $T_2^* = \sqrt{2}/\sigma_{\text{nuc}}$. In order to model this effect, we have to include the Hamiltonian [31, 267, 268]

$$H_{\text{deph}} = \sum_{i=1,2} B_i^{\text{nuc}} S_i^{\text{z}} \tag{G.1}$$

with random parameters B_i^{nuc} sampled independently from a normal distribution with standard deviation σ_{nuc}.

Transport via QH edge states

In chapter 7 we obtained the approximated master equations (7.26) and (7.29) for the dynamics of the spin-qubits without accounting for noise sources. To observe the effect of nuclear dephasing for these proposals, we plot in Fig. G.1 the entanglement of formation (E_F) in the steady state for different values of the cooperativity-like parameter, defined as $C = J_0^2/\gamma\sigma_{\text{nuc}}$, which compares desired $\sim J_0^2/\gamma$ to undesired $\sim \sigma_{\text{nuc}} \sim 1/T_2^*$ rates. As expected from the analysis of the spectral gap

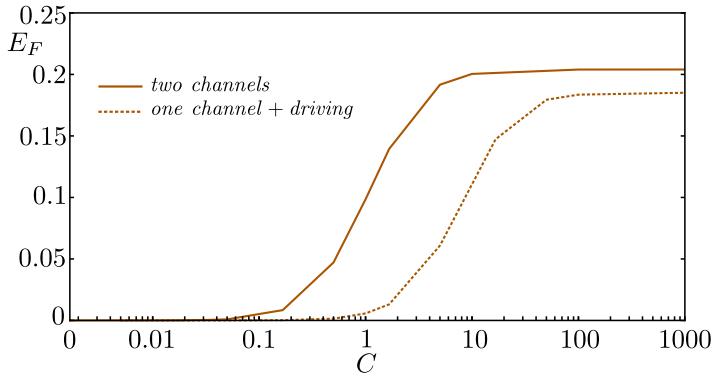

FIGURE G.1. Steady-state entanglement between two remote qubits quantified via the E_F for the two QH-based proposals as a function of the cooperativity $C = J_0^2/\gamma\sigma_{\rm nuc}$. The solid (dotted) line results are based on Eqs. (7.26) and (7.29), respectively. Numerical parameters: $\gamma_{\rm L} = \gamma = 30\mu$eV, $J_0 = 3\mu$eV, $\delta J/J_0 = 0.44$ ($\delta J/J_0 = 0.14$) for solid (dotted) line and $\delta_i \in (-2,2)\,\mu$eV.

in chapter 7, the purely dissipative proposal is typically found to be more robust. By choosing the values $\gamma = 30\mu$eV and $J_0 = 3\mu$eV we can predict that a value of $\sigma_{\rm nuc} = 0.03\mu$eV, which corresponds to a cooperativity $C = 10$, would be very good concerning the purely dissipative proposal. This standard deviation corresponds to a dephasing time $T_2^* \simeq 30$ns, which is experimentally feasible and can be improved up to 3μs using nuclear-state-narrowing techniques [244, 267].

To model the possible electron losses due to imperfections in the transport channel, we include a Lindblad dissipator with rate Γ_l acting in the first ancilla QD, i.e., $\sum_\sigma \Gamma_l/2\mathscr{D}\left[d_1^\sigma\right]$ (also in d_4^σ in

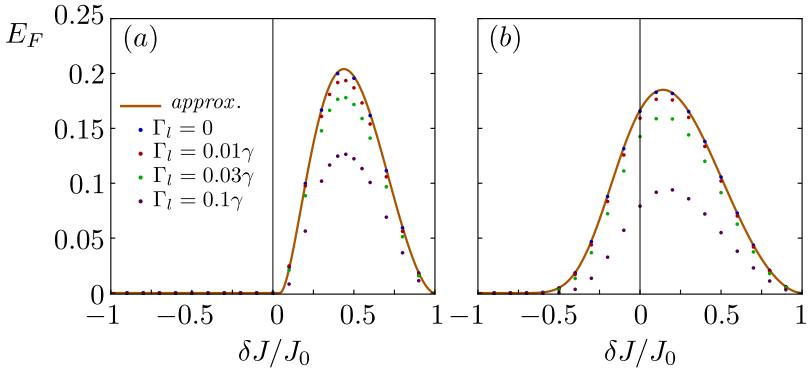

FIGURE G.2. Steady-state entanglement between two remote qubits quantified via the E_F for the two QH-based proposals as a function of δJ. The solid lines in (a) and (b) refer to Eqs. (7.26) and (7.29), respectively, while the dots are calculated with the full master equation including ancilla QDs and different losses rates Γ_l. Numerical parameters: $\gamma_{\rm L} = \gamma = 30\mu$eV, $J_0 = 3\mu$eV and $\delta_i \in (-2,2)\,\mu$eV. In (b), for each value of δJ, Ω_i has been optimized in the range $\Omega_i \in (0-50)$neV.

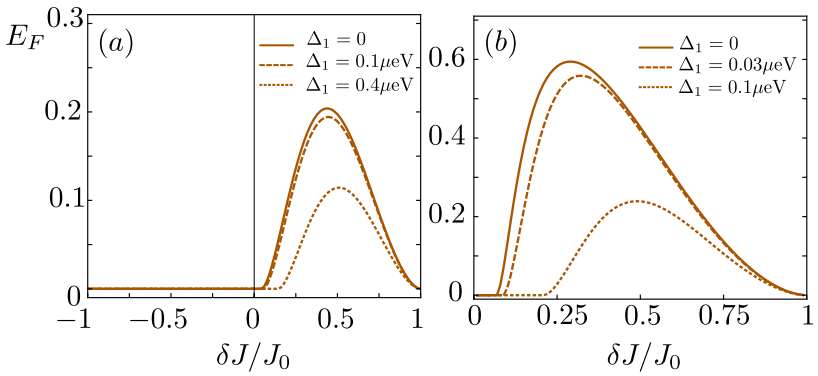

FIGURE G.3. Steady-state entanglement between two remote qubits quantified via the E_F for two proposals as a function of δJ. The solid lines in (a) and (b) refer to Eqs. (7.26) and (7.36), respectively, while the results in dashed and dotted lines account for different values of the residual gradient Δ_1 ($\Delta_2 = 0$). Numerical parameters: (a) $\gamma_L = \gamma = 30\mu$eV, $J_0 = 3\mu$eV. (b) $J_0 = 2.5\mu$eV, $\tau = 0.1$ns.

the two-channels proposal). The result, shown in Fig. G.2, predicts that we can afford a small percent of losses.

Finally, we verify in Fig. G.3 (a) that the perfect cancellation of the first-order terms is not necessary, provided that the residual gradients Δ_i are small compared to the gap.

Transport via SAW moving QDs

The approximated Eqs. (7.36) and (7.37) suggest that the simulation of the full problem given in Eq. (7.32) will drive the main qubits to an entangled steady state regardless of the initial state (as long as $\tau J_i \ll 1$). However, in a realistic experimental situation, there will be also some noise sources. In the following, we account for: (i) dephasing due to the nuclear spins, (ii) imperfections due to the uncertainty in the dwell time τ (time jitter), (iii) electron losses due to imperfections in the transport mechanism and (iv) residual gradients. (i) As explained above, we include a dephasing Hamiltonian as in Eq. (G.1) to model the non-Markovian noise due to the hyperfine interaction. We assume that the ancilla QDs are refilled very quickly after every step and thus neglect the evolution in the short intermittent intervals when the ancilla QD is empty. (ii) In a realistic experimental situation, there will be also some noise associated with the uncertainty in the dwell times [117]. We include this noise source by choosing the times τ_i randomly from a Gaussian distribution centered around the average (τ) with a standard deviation of σ_τ. (iii) To model the losses we assume during the time simulation that with a certain probability an ancilla spin never interacts with the second localized spin. (iv) We estimate how large the imperfections in the magnetic gradients can be such that the entanglement generation is not severely affected.

In Fig. G.4 we show the effect of the noise sources (i), (ii) and (iii) in the simulation in terms of

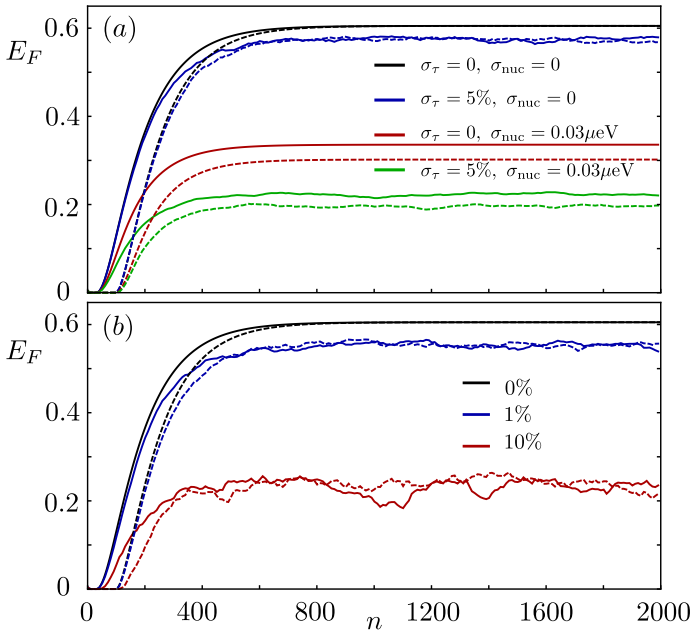

FIGURE G.4. Entanglement between two remote qubits quantified via the E_F for the SAW-based proposal corresponding to Eq. (7.36) as a function of time ($t = 2n\tau$) for two different initial states (solid and dashed lines, respectively) and $\delta J/J_0 = 0.28$, $J_0 = 2.5\mu$eV and $\tau = 0.1$ns. In both (a) and (b), the black curves depict the ideal case and the remaining curves show the effect of different kinds of noise [time jitter σ_τ and nuclear dephasing in (a); electron losses in (b)] averaged over several random trajectories of the respective processes.

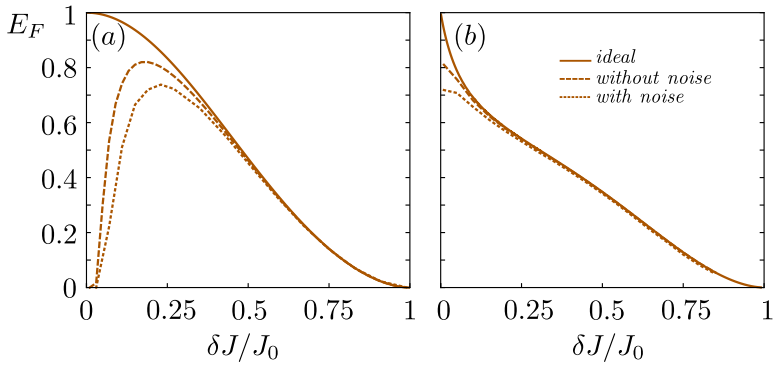

FIGURE G.5. Steady-state entanglement between two remote qubits quantified via the E_F for the two SAW-based proposals as a function of δJ ($J^{\uparrow}_{1(2)} = J_0 \mp \delta J$). (a) and (b) show the results of Eqs. (7.36) and (7.37), respectively. The solid lines refer to the ideal result, given by the lower order terms present in Eqs. (7.36) and (7.37), while the dashed lines correspond to the full evolution. The dotted lines also account for noise due to uncertainty in the dwell times and dephasing. Numerical parameters: $\sigma_\tau = 5\%$, $J_0\tau \approx 0.15$ and $T_2^*/\tau \approx 30000$. In (b), for each value of δJ, Ω_i has been optimized in the range $\Omega_i\tau \in (0-3)\cdot 10^{-3}$.

E_F of the state. The convergence is found after $\sim 10^3$ iterations, which corresponds to the regime of $(0.1-1)\mu$s for $\tau = (0.1-1)$ns. Note that if the product $J_0\tau$ is fixed, the results do not change, but the time to reach the steady state and consequently the undesired dephasing decrease with τ. Once a small enough τ is fixed, the result improves as J_0 decreases but obviously the time grows and we need to find a compromise between the conditions $\tau J_0 \ll 1$ and a time sufficiently short for the given nuclear dephasing time. In Fig. G.3 b) we show the effect of (iv) in the entanglement generation scheme with alternating spins.

The short dephasing times considered within the main text force us to choose a quite large value of $\tau J_0 = 0.38$; therefore the amount of entanglement generated is bounded to $E_F \gtrsim 0.4$. If the dephasing time reaches the maximal experimental reported value of $T_2^* = 3\mu$s, the amount of steady-state entanglement increases up to $E_F \gtrsim 0.7$, as shown in Fig. G.5.

Acronyms

2DEG two-dimensional electron gas. 1–3, 13, 83, 91

BCS Bardeen-Cooper-Schrieffer. 13, 15, 20, 29–32, 36, 115

BdG Bogoliubov-de Gennes. 13–15, 21, 31

CDT coherent destruction of tunneling. 73–75

CTAP coherent transfer by adiabatic passage. 45, 46, 53–55, 57

FCS full-counting statistics. 4, 10, 45, 46, 57, 59, 69, 101

FMBS Floquet Majorana bound state. 4, 8, 16, 19, 33, 35, 38–44

LZSM Landau-Zener-Stückelberg-Majorana. 45, 55–57

MBS Majorana bound state. 2–4, 16, 19, 20, 27, 29, 30, 32, 33, 35, 37, 40, 43

QD quantum dot. 1–4, 8, 9, 32, 35–46, 49, 51–57, 59, 60, 69, 70, 74, 78, 81–87, 89–96, 98, 100, 101, 110, 125–127

QH quantum Hall. 1, 4, 12–14, 81–83, 89, 93–95, 98–100, 126

QIP quantum information processing. 1, 9, 79, 81, 99

SAW surface acoustic wave. 4, 81, 82, 91–93, 97–99, 125, 128

SET single-electron transistor. 51, 52

SSH Su-Schrieffer-Heeger. 13, 16, 59–61, 70, 71, 73, 77, 79

TPT topological phase transition. 11, 12, 19, 20, 23–25, 27, 32, 59–61, 63, 66, 70, 79

BIBLIOGRAPHY

[1] H. Bruus and K. Flensberg, *Many-body quantum theory in condensed matter physics* (Oxford University Press, 2004).

[2] D. Loss and D. P. DiVincenzo, Phys. Rev. A **57**, 120 (1998).

[3] D. P. DiVincenzo, D. Bacon, J. Kempe, G. Burkard, and K. B. Whaley, Nature **408**, 339 (2000).

[4] M. A. Nielsen and I. L. Chuang, *Quantum Computation and Quantum Information* (Cambridge University Press, 2010).

[5] R. P. Feynman, Int. J. Theor. Phys. **21**, 467 (1982).

[6] D. Deutsch, Proceedings of the Royal Society of London A: Mathematical, Physical and Engineering Sciences **400**, 97 (1985).

[7] D. P. DiVincenzo, Fortschritte der Physik **48**, 771 (2000).

[8] C. Monroe, Nature **416**, 238 (2002).

[9] T. D. Ladd, F. Jelezko, R. Laflamme, Y. Nakamura, C. Monroe, and J. L. O'Brien, Nature **464**, 45 (2010).

[10] D. D. Awschalom, L. C. Bassett, A. S. Dzurak, E. L. Hu, and J. R. Petta, Science **339**, 1174 (2013).

[11] J. I. Cirac and P. Zoller, Phys. Rev. Lett. **74**, 4091 (1995).

[12] C. Monroe, D. M. Meekhof, B. E. King, W. M. Itano, and D. J. Wineland, Phys. Rev. Lett. **75**, 4714 (1995).

[13] D. Jaksch, C. Bruder, J. I. Cirac, C. W. Gardiner, and P. Zoller, Phys. Rev. Lett. **81**, 3108 (1998).

[14] J. I. Cirac and P. Zoller, Science **301**, 176 (2003).

[15] I. Bloch, Nat. Phys. **1**, 23 (2005).

[16] I. Bloch, J. Dalibard, and W. Zwerger, Rev. Mod. Phys. **80**, 885 (2008).

[17] J. M. Raimond, M. Brune, and S. Haroche, Rev. Mod. Phys. **73**, 565 (2001).

[18] H. Walther, B. T. H. Varcoe, B.-G. Englert, and T. Becker, Rep. Prog. Phys. **69**, 1325 (2006).

[19] B. E. Kane, Nature **393**, 133 (1998).

[20] N. Y. Yao, L. Jiang, A. V. Gorshkov, P. C. Maurer, G. Giedke, J. I. Cirac, and M. D. Lukin, Nat. Commun. **3**, 800 (2012).

[21] J. Clarke and F. K. Wilhelm, Nature **453**, 1031 (2008).

[22] K. v. Klitzing, G. Dorda, and M. Pepper, Phys. Rev. Lett. **45**, 494 (1980).

[23] C. Nayak, S. H. Simon, A. Stern, M. Freedman, and S. Das Sarma, Rev. Mod. Phys. **80**, 1083 (2008).

[24] M. Leijnse and K. Flensberg, Semiconductor Science and Technology **27**, 124003 (2012).

[25] J. Alicea, Rep. Prog. Phys. **75**, 076501 (2012).

[26] J. Alicea, Nat. Nanotechnol. **8**, 623 (2013).

[27] M. A. Kastner, Physics Today **46**, 24 (1993).

[28] L. P. Kouwenhoven and C. M. Marcus, Physics World **11**, 35 (1998).

[29] S. M. Reimann and M. Manninen, Rev. Mod. Phys. **74**, 1283 (2002).

[30] R. Hanson, L. P. Kouwenhoven, J. R. Petta, S. Tarucha, and L. M. K. Vandersypen, Rev. Mod. Phys. **79**, 1217 (2007).

[31] C. Kloeffel and D. Loss, Annu. Rev. Condens. Matter Phys. **4**, 51 (2013).

[32] P. Barthelemy and L. M. K. Vandersypen, Ann. Phys. **525**, 808 (2013).

[33] F. Grossmann, T. Dittrich, P. Jung, and P. Hänggi, Phys. Rev. Lett. **67**, 516 (1991).

[34] F. Großmann and P. Hänggi, Europhys. Lett. **18**, 571 (1992).

[35] C. E. Creffield and G. Platero, Phys. Rev. B **65**, 113304 (2002).

[36] C. E. Creffield and G. Platero, Phys. Rev. B **69**, 165312 (2004).

[37] A. Gómez-León and G. Platero, Phys. Rev. B **84**, 121310 (2011).

[38] R. Menchon-Enrich, A. Benseny, V. Ahufinger, A. D. Greentree, T. Busch, and J. Mompart, Rep. Prog. Phys. **79**, 074401 (2016).

[39] G. Floquet, Annales scientifiques de l'École Normale Supérieure **12**, 47 (1883).

[40] J. H. Shirley, Phys. Rev. **138**, B979 (1965).

[41] H. Sambe, Phys. Rev. A **7**, 2203 (1973).

[42] J. Inoue and A. Tanaka, Phys. Rev. Lett. **105**, 017401 (2010).

[43] N. H. Lindner, G. Refael, and V. Galitski, Nat. Phys. **7**, 490 (2011).

[44] L. Jiang, T. Kitagawa, J. Alicea, A. R. Akhmerov, D. Pekker, G. Refael, J. I. Cirac, E. Demler, M. D. Lukin, and P. Zoller, Phys. Rev. Lett. **106**, 220402 (2011).

[45] T. Kitagawa, M. A. Broome, A. Fedrizzi, M. S. Rudner, E. Berg, I. Kassal, A. Aspuru-Guzik, E. Demler, and A. G. White, Nat. Commun. **3**, 882 (2012).

[46] A. Gómez-León and G. Platero, Phys. Rev. Lett. **110**, 200403 (2013).

[47] A. G. Grushin, A. Gómez-León, and T. Neupert, Phys. Rev. Lett. **112**, 156801 (2014).

[48] W. G. van der Wiel, S. De Franceschi, J. M. Elzerman, T. Fujisawa, S. Tarucha, and L. P. Kouwenhoven, Rev. Mod. Phys. **75**, 1 (2002).

[49] J. M. Elzerman, R. Hanson, L. H. Willems van Beveren, B. Witkamp, L. M. K. Vandersypen, and L. P. Kouwenhoven, Nature **430**, 431 (2004).

[50] J. R. Petta, A. C. Johnson, J. M. Taylor, E. A. Laird, A. Yacoby, M. D. Lukin, C. M. Marcus, M. P. Hanson, and A. C. Gossard, Science **309**, 2180 (2005).

[51] F. H. L. Koppens, C. Buizert, K. J. Tielrooij, I. T. Vink, K. C. Nowack, T. Meunier, L. P. Kouwenhoven, and L. M. K. Vandersypen, Nature **442**, 766 (2006).

[52] K. C. Nowack, F. H. L. Koppens, Y. V. Nazarov, and L. M. K. Vandersypen, Science **318**, 1430 (2007).

[53] K. C. Nowack, M. Shafiei, M. Laforest, G. E. D. K. Prawiroatmodjo, L. R. Schreiber, C. Reichl, W. Wegscheider, and L. M. K. Vandersypen, Science **333**, 1269 (2011).

[54] M. D. Shulman, O. E. Dial, S. P. Harvey, H. Bluhm, V. Umansky, and A. Yacoby, Science **336**, 202 (2012).

[55] R. K. Puddy, L. W. Smith, H. Al-Taie, C. H. Chong, I. Farrer, J. P. Griffiths, D. A. Ritchie, M. J. Kelly, M. Pepper, and C. G. Smith, Appl. Phys. Lett. **107**, 143501 (2015).

[56] D. M. Zajac, T. M. Hazard, X. Mi, E. Nielsen, and J. R. Petta, Phys. Rev. Applied **6**, 054013 (2016).

[57] F. Braakman, P. Barthelemy, C. Reichl, W. Wegschneider, and L. Vandersypen, Nat. Nanotechnol. **8**, 432 (2013).

[58] M. Busl, G. Granger, L. Gaudreau, R. Sánchez, A. Kam, Pioro-Ladrière, S. A. Studenikin, P. Zawadzki, Z. R. Wasilewski, A. S. Sachrajda, and G. Platero, Nat. Nanotechnol. **8**, 261 (2013).

[59] L. R. Schreiber and H. Bluhm, Nat. Nanotechnol. **9**, 966 (2014).

[60] J. F. Poyatos, J. I. Cirac, and P. Zoller, Phys. Rev. Lett. **77**, 4728 (1996).

[61] M. B. Plenio, S. F. Huelga, A. Beige, and P. L. Knight, Phys. Rev. A **59**, 2468 (1999).

[62] A. Beige, D. Braun, B. Tregenna, and P. L. Knight, Phys. Rev. Lett. **85**, 1762 (2000).

[63] D. Braun, Phys. Rev. Lett. **89**, 277901 (2002).

[64] F. Benatti, R. Floreanini, and M. Piani, Phys. Rev. Lett. **91**, 070402 (2003).

[65] B. Kraus, H. P. Büchler, S. Diehl, A. Kantian, A. Micheli, and P. Zoller, Phys. Rev. A **78**, 042307 (2008).

[66] S. Diehl, A. Micheli, A. Kantian, B. Kraus, H. P. Buchler, and P. Zoller, Nat. Phys. **4**, 878 (2008).

[67] F. Verstraete, M. M. Wolf, and J. I. Cirac, Nat. Phys. **5**, 633 (2009).

[68] S. Diehl, E. Rico, M. A. Baranov, and P. Zoller, Nat. Phys. **7**, 971 (2011).

[69] J. T. Barreiro, M. Muller, P. Schindler, D. Nigg, T. Monz, M. Chwalla, M. Hennrich, C. F. Roos, P. Zoller, and R. Blatt, Nature **470**, 486 (2011).

[70] H. Krauter, C. A. Muschik, K. Jensen, W. Wasilewski, J. M. Petersen, J. I. Cirac, and E. S. Polzik, Phys. Rev. Lett. **107**, 080503 (2011).

[71] Y. Lin, J. P. Gaebler, F. Reiter, T. R. Tan, R. Bowler, A. S. Sorensen, D. Leibfried, and D. J. Wineland, Nature **504**, 415 (2013).

[72] S. Shankar, M. Hatridge, Z. Leghtas, K. M. Sliwa, A. Narla, U. Vool, S. M. Girvin, L. Frunzio, M. Mirrahimi, and M. H. Devoret, Nature **504**, 419 (2013).

[73] A. Eckardt, arXiv:1606.08041 (2016).

[74] A. Eckardt and E. Anisimovas, New J. Phys. **17**, 093039 (2015).

[75] S. Blanes, F. Casas, J. Oteo, and J. Ros, Phys. Rep. **470**, 151 (2009).

[76] N. Goldman and J. Dalibard, Phys. Rev. X **4**, 031027 (2014).

[77] M. Grifoni and P. Hänggi, Phys. Rep. **304**, 229 (1998).

[78] G. Platero and R. Aguado, Phys. Rep. **395**, 1 (2004).

[79] S. Kohler, J. Lehmann, and P. Hänggi, Phys. Rep. **406**, 379 (2005).

[80] W. D. Oliver, Y. Yu, J. C. Lee, K. K. Berggren, L. S. Levitov, and T. P. Orlando, Science **310**, 1653 (2005).

[81] M. Sillanpää, T. Lehtinen, A. Paila, Y. Makhlin, and P. Hakonen, Phys. Rev. Lett. **96**, 187002 (2006).

[82] J. Stehlik, Y. Dovzhenko, J. R. Petta, J. R. Johansson, F. Nori, H. Lu, and A. C. Gossard, Phys. Rev. B **86**, 121303 (2012).

[83] F. Forster, G. Petersen, S. Manus, P. Hänggi, D. Schuh, W. Wegscheider, S. Kohler, and S. Ludwig, Phys. Rev. Lett. **112**, 116803 (2014).

[84] F. Gallego-Marcos, R. Sánchez, and G. Platero, J. Appl. Phys. **117**, 112808 (2015).

[85] G. Lindblad, Comm. Math. Phys. **48**, 119 (1976).

[86] D. Weinmann, W. Häusler, and B. Kramer, Phys. Rev. Lett. **74**, 984 (1995).

[87] K. Ono, D. G. Austing, Y. Tokura, and S. Tarucha, Science **297**, 1313 (2002).

[88] E. M. Weig, R. H. Blick, T. Brandes, J. Kirschbaum, W. Wegscheider, M. Bichler, and J. P. Kotthaus, Phys. Rev. Lett. **92**, 046804 (2004).

[89] J. Koch and F. von Oppen, Phys. Rev. Lett. **94**, 206804 (2005).

[90] R. Leturcq, C. Stampfer, K. Inderbitzin, L. Durrer, C. Hierold, E. Mariani, M. G. Schultz, F. von Oppen, and K. Ensslin, Nat. Phys. **5**, 327 (2009).

[91] P. Barthold, F. Hohls, N. Maire, K. Pierz, and R. J. Haug, Phys. Rev. Lett. **96**, 246804 (2006).

[92] R. Sánchez, S. Kohler, P. Hänggi, and G. Platero, Phys. Rev. B **77**, 035409 (2008).

[93] M. J. Kastoryano, F. Reiter, and A. S. Sørensen, Phys. Rev. Lett. **106**, 090502 (2011).

[94] C. A. Muschik, E. S. Polzik, and J. I. Cirac, Phys. Rev. A **83**, 052312 (2011).

[95] K. Stannigel, P. Rabl, and P. Zoller, New J. Phys. **14**, 063014 (2012).

[96] F. Ticozzi and L. Viola, Philosophical Transactions of the Royal Society of London A: Mathematical, Physical and Engineering Sciences **370**, 5259 (2012).

[97] R. Sánchez and G. Platero, Phys. Rev. B **87**, 081305 (2013).

[98] M. J. A. Schuetz, E. Kessler, L. M. K. Vandersypen, J. I. Cirac, and G. Giedke, Phys. Rev. Lett. **111**, 246802 (2013).

[99] J. B. Brask, G. Haack, N. Brunner, and M. Huber, New J. Phys. **17**, 113029 (2015).

[100] A. C. Y. Li, F. Petruccione, and J. Koch, Sci. Rep. **4**, 4887 (2014).

[101] F. Benatti, A. Nagy, and H. Narnhofer, Journal of Physics A: Mathematical and Theoretical **44**, 155303 (2011).

[102] M. Nakahara, *Geometry, Topology and Physics, Second Edition*, Graduate student series in physics (Taylor & Francis, 2003).

[103] B. A. Bernevig, *Topological Insulators and Topological Superconductors* (Princeton University Press, Princeton, NJ, 2013).

[104] M. V. Berry, Proceedings of the Royal Society of London A: Mathematical, Physical and Engineering Sciences **392**, 45 (1984).

[105] D. Xiao, M.-C. Chang, and Q. Niu, Rev. Mod. Phys. **82**, 1959 (2010).

[106] M. Z. Hasan and C. L. Kane, Rev. Mod. Phys. **82**, 3045 (2010).

[107] J. Zak, Phys. Rev. Lett. **62**, 2747 (1989).

[108] S. Ryu, A. P. Schnyder, A. Furusaki, and A. W. W. Ludwig, New J. Phys. **12**, 065010 (2010).

[109] A. Altland and M. R. Zirnbauer, Phys. Rev. B **55**, 1142 (1997).

[110] A. P. Schnyder, S. Ryu, A. Furusaki, and A. W. W. Ludwig, Phys. Rev. B **78**, 195125 (2008).

[111] L. Li, C. Yang, and S. Chen, Europhys. Lett. **112**, 10004 (2015).

[112] D. K. Ferry, in *Transport in Semiconductor Mesoscopic Devices*, 2053-2563 (IOP Publishing, 2015) pp. 6–1 to 6–26.

[113] M. Franz, Nat. Nanotechnol. **8**, 149 (2013).

[114] Y. Hadad, A. B. Khanikaev, and A. Alù, Phys. Rev. B **93**, 155112 (2016).

[115] R. B. Laughlin, Phys. Rev. B **23**, 5632 (1981).

[116] D. J. Thouless, M. Kohmoto, M. P. Nightingale, and M. den Nijs, Phys. Rev. Lett. **49**, 405 (1982).

[117] E. Bocquillon, V. Freulon, J. M. Berroir, P. Degiovanni, B. Plaçais, A. Cavanna, Y. Jin, and G. Fève, Science **339**, 1054 (2013).

[118] J. Bardeen, L. N. Cooper, and J. R. Schrieffer, Phys. Rev. **108**, 1175 (1957).

[119] M. Tinkham, *Introduction to Superconductivity: Second Edition* (Dover Publications, 2004).

[120] P. G. de Gennes, *Superconductivity of Metals and Alloys* (Benjamin. New York, 1966).

[121] A. Y. Kitaev, Phys. Usp. **44**, 131 (2001).

[122] E. Majorana, Il Nuovo Cimento (1924-1942) **14**, 171 (2008).

[123] F. Wilczek, Nat. Phys. **5**, 614 (2009).

[124] C. Beenakker, Ann. Rev. Condens. Matter Phys. **4**, 113 (2013).

[125] Y. Oreg, G. Refael, and F. von Oppen, Phys. Rev. Lett. **105**, 177002 (2010).

[126] R. Lutchyn, J. Sau, and S. D. Sarma, Phys. Rev. Lett. **105**, 077001 (2010).

[127] F. Domínguez, F. Hassler, and G. Platero, Phys. Rev. B **86**, 140503 (2012).

[128] V. Mourik, K. Zuo, S. M. Frolov, S. R. Plissard, E. P. a. M. Bakkers, and L. P. Kouwenhoven, Science **336**, 1003 (2012).

[129] L. P. Rokhinson, X. Liu, and J. K. Furdyna, Nat. Phys. **8**, 795 (2012).

[130] A. Das, Y. Ronen, Y. Most, Y. Oreg, M. Heiblum, and H. Shtrikman, Nat. Phys. **8**, 887 (2012).

[131] M. T. Deng, C. L. Yu, G. Y. Huang, M. Larsson, P. Caroff, and H. Q. Xu, Nano Lett. **12**, 6414 (2012).

[132] D. E. Liu, A. Levchenko, and H. U. Baranger, Phys. Rev. Lett. **111**, 047002 (2013).

[133] W. P. Su, J. R. Schrieffer, and A. J. Heeger, Phys. Rev. Lett. **42**, 1698 (1979).

[134] W. P. Su, J. R. Schrieffer, and A. J. Heeger, Phys. Rev. B **22**, 2099 (1980).

[135] M. Atala, M. Aidelsburger, J. T. Barreiro, D. Abanin, T. Kitagawa, E. Demler, and I. Bloch, Nat. Phys. **9**, 795 (2013).

[136] P. Delplace, D. Ullmo, and G. Montambaux, Phys. Rev. B **84**, 195452 (2011).

[137] A. Kundu and B. Seradjeh, Phys. Rev. Lett. **111**, 136402 (2013).

[138] P. Wang, Q.-f. Sun, and X. C. Xie, Phys. Rev. B **90**, 155407 (2014).

[139] C. C. Wu, J. Sun, F. J. Huang, Y. D. Li, and W. M. Liu, Europhys. Lett. **104**, 27004 (2013).

[140] A. Reynoso and D. Frustaglia, Phys. Rev. B **87**, 115420 (2013).

[141] M. Thakurathi, A. A. Patel, D. Sen, and A. Dutta, Phys. Rev. B **88**, 155133 (2013).

[142] Q.-J. Tong, J.-H. An, J. Gong, H.-G. Luo, and C. H. Oh, Phys. Rev. B **87**, 201109 (2013).

[143] Y. Niu, S. B. Chung, C.-H. Hsu, I. Mandal, S. Raghu, and S. Chakravarty, Phys. Rev. B **85**, 035110 (2012).

[144] S. Tewari and J. D. Sau, Phys. Rev. Lett. **109**, 150408 (2012).

[145] J. D. Sau and S. D. Sarma, Nat. Commun. **3**, 964 (2012).

[146] I. C. Fulga, A. Haim, A. R. Akhmerov, and Y. Oreg, New J. Phys. **15**, 045020 (2013).

[147] S. De Franceschi, L. Kouwenhoven, C. Schönenberger, and W. Wernsdorfer, Nat. Nanotechnol. **5**, 703 (2010).

[148] A. Martín-Rodero and A. L. Yeyati, Advances in Physics **60**, 899 (2011).

[149] S. Weiss and M. Governale, Phys. Rev. B **90**, 220501 (2014).

[150] M. Leijnse and K. Flensberg, Phys. Rev. B **86**, 134528 (2012).

[151] M.-X. Deng, S.-H. Zheng, M. Yang, L.-B. Hu, and R.-Q. Wang, Chinese Physics B **24**, 037302 (2015).

[152] Y. Li, A. Kundu, F. Zhong, and B. Seradjeh, Phys. Rev. B **90**, 121401 (2014).

[153] B. Sothmann, J. Li, and M. Büttiker, New J. Phys. **15**, 085018 (2013).

[154] A. R. Wright and M. Veldhorst, Phys. Rev. Lett. **111**, 096801 (2013).

[155] J. Eldridge, M. G. Pala, M. Governale, and J. König, Phys. Rev. B **82**, 184507 (2010).

[156] M. C. Rogge and R. J. Haug, New J. Phys. **11**, 113037 (2009).

[157] G. Granger, L. Gaudreau, A. Kam, M. Pioro-Ladrière, S. A. Studenikin, Z. R. Wasilewski, P. Zawadzki, and A. S. Sachrajda, Phys. Rev. B **82**, 075304 (2010).

[158] T. Takakura, A. Noiri, T. Obata, T. Otsuka, J. Yoneda, K. Yoshida, and S. Tarucha, Appl. Phys. Lett. **104**, 113109 (2014).

[159] K. Flensberg, Phys. Rev. B **82**, 180516 (2010).

[160] M. X. Deng, R. Q. Wang, B. Q. Ai, M. Yang, L. B. Hu, Q. H. Zhong, and G. H. Wang, Phys. Lett. A **378**, 2256 (2014).

[161] D. K. C. Macdonald, Rep. Prog. Phys. **12**, 56 (1949).

[162] Ya. M. Blanter and M. Büttiker, Phys. Rep. **336**, 1 (2000).

[163] M. Büttiker, Phys. Rev. B **46**, 12485 (1992).

[164] L. S. Levitov and G. B. Lesovik, JETP Lett. **58**, 230 (1993).

[165] D. A. Bagrets and Yu. V. Nazarov, Phys. Rev. B **67**, 085316 (2003).

[166] W. Belzig, Phys. Rev. B **71**, 161301 (2005).

[167] T. Brandes, Ann. der Phys. **17**, 477 (2008).

[168] C. Beenakker and C. Schönenberger, Phys. Today **56**, 37 (2003).

[169] X. Jehl, M. Sanquer, R. Calemczuk, and D. Mailly, Nature **405**, 50 (2000).

[170] N. Lambert, F. Nori, and C. Flindt, Phys. Rev. Lett. **115**, 216803 (2015).

[171] S. Camalet, J. Lehmann, S. Kohler, and P. Hänggi, Phys. Rev. Lett. **90**, 210602 (2003).

[172] L. Fricke, M. Wulf, B. Kaestner, V. Kashcheyevs, J. Timoshenko, P. Nazarov, F. Hohls, P. Mirovsky, B. Mackrodt, R. Dolata, T. Weimann, K. Pierz, and H. W. Schumacher, Phys. Rev. Lett. **110**, 126803 (2013).

[173] B. Kaestner and V. Kashcheyevs, Rep. Prog. Phys. **78**, 103901 (2015).

[174] A. Croy and U. Saalmann, Phys. Rev. B **93**, 165428 (2016).

[175] M. Kataoka, N. Johnson, C. Emary, P. See, J. P. Griffiths, G. A. C. Jones, I. Farrer, D. A. Ritchie, M. Pepper, and T. J. B. M. Janssen, Phys. Rev. Lett. **116**, 126803 (2016).

[176] J. Huneke, G. Platero, and S. Kohler, Phys. Rev. Lett. **110**, 036802 (2013).

[177] A. D. Greentree, J. H. Cole, A. R. Hamilton, and L. C. L. Hollenberg, Phys. Rev. B **70**, 235317 (2004).

[178] K. Eckert, M. Lewenstein, R. Corbalán, G. Birkl, W. Ertmer, and J. Mompart, Phys. Rev. A **70**, 023606 (2004).

[179] R. Sánchez, S. Kohler, and G. Platero, New J. Phys. **10**, 115013 (2008).

[180] S. A. Gurvitz and Ya. S. Prager, Phys. Rev. B **53**, 15932 (1996).

[181] B. Kubala, J. Ankerhold, and A. D. Armour, arXiv:1606.02200 (2016).

[182] A. G. Redfield, IBM J. Res. Dev. **1**, 19 (1957).

[183] K. Blum, *Density Matrix Theory and Applications*, 2nd ed. (Springer, New York, 1996).

[184] H.-P. Breuer and F. Petruccione, *Theory of open quantum systems* (Oxford University Press, Oxford, 2003).

[185] N. G. van Kampen, *Stochastic processes in physics and chemistry* (North-Holland, Amsterdam, 1992).

[186] D. Darau, G. Begemann, A. Donarini, and M. Grifoni, Phys. Rev. B **79**, 235404 (2009).

[187] C. Flindt, T. Novotný, A. Braggio, M. Sassetti, and A.-P. Jauho, Phys. Rev. Lett. **100**, 150601 (2008).

[188] C. Flindt, T. Novotný, A. Braggio, and A.-P. Jauho, Phys. Rev. B **82**, 155407 (2010).

[189] D. Kambly, C. Flindt, and M. Büttiker, Phys. Rev. B **83**, 075432 (2011).

[190] D. Kambly and C. Flindt, Journal of Computational Electronics **12**, 331 (2013).

[191] C. Flindt, C. Fricke, F. Hohls, T. Novotný, K. Netočný, T. Brandes, and R. J. Haug, Proc. Natl. Acad. Sci. USA **106**, 10116 (2009).

[192] C. Emary, D. Marcos, R. Aguado, and T. Brandes, Phys. Rev. B **76**, 161404 (2007).

[193] M. Niklas, A. Trottmann, A. Donarini, and M. Grifoni, (2016).

[194] C. W. Groth, B. Michaelis, and C. W. J. Beenakker, Phys. Rev. B **74**, 125315 (2006).

[195] F. Domínguez, G. Platero, and S. Kohler, Chem. Phys. **375**, 284 (2010).

[196] N. V. Vitanov, T. Halfmann, B. W. Shore, and K. Bergmann, Ann. Rev. Phys. Chem. **52**, 763 (2001).

[197] J. Rech and S. Kehrein, Phys. Rev. Lett. **106**, 136808 (2011).

[198] S. N. Shevchenko, S. Ashhab, and F. Nori, Phys. Rep. **492**, 1 (2010).

[199] M. Strass, P. Hänggi, and S. Kohler, Phys. Rev. Lett. **95**, 130601 (2005).

[200] D. Marcos, C. Emary, T. Brandes, and R. Aguado, Phys. Rev. B **83**, 125426 (2011).

[201] P. Stegmann and J. König, Phys. Rev. B **94**, 125433 (2016).

[202] H.-P. Breuer, B. Kappler, and F. Petruccione, Annals of Physics **291**, 36 (2001).

[203] F. Kaiser and S. Kohler, Ann. Phys. **16**, 702 (2007).

[204] D. Taubert, D. Schuh, W. Wegscheider, and S. Ludwig, Rev. Sci. Instrum. **82**, 123905 (2011).

[205] F. J. Kaiser, M. Strass, S. Kohler, and P. Hänggi, Chem. Phys. **322**, 193 (2006).

[206] G. Kießlich, E. Schöll, T. Brandes, F. Hohls, and R. J. Haug, Phys. Rev. Lett. **99**, 206602 (2007).

[207] P. W. Anderson, Phys. Rev. **109**, 1492 (1958).

[208] N. Kocić, P. Weiderer, S. Keller, S. Decurtins, S.-X. Liu, and J. Repp, Nano Lett. **15**, 4406 (2015).

[209] M. Holthaus, Phys. Rev. Lett. **69**, 351 (1992).

[210] V. Dal Lago, M. Atala, and L. E. F. Foa Torres, Phys. Rev. A **92**, 023624 (2015).

[211] M. Bello, C. E. Creffield, and G. Platero, Sci. Rep. **6**, 22562 (2016).

[212] F. Forster, M. Mühlbacher, R. Blattmann, D. Schuh, W. Wegscheider, S. Ludwig, and S. Kohler, Phys. Rev. B **92**, 245422 (2015).

[213] J. K. Asbóth, B. Tarasinski, and P. Delplace, Phys. Rev. B **90**, 125143 (2014).

[214] H. Risken, *The Fokker-Planck equation*, 2nd ed., Springer Series in Synergetics, Vol. 18 (Springer, Berlin, 1989).

[215] G. Platero and R. Aguado, Appl. Phys. Lett. **70**, 3546 (1997).

[216] G. Usaj, P. M. Perez-Piskunow, L. E. F. Foa Torres, and C. A. Balseiro, Phys. Rev. B **90**, 115423 (2014).

[217] R. Hanson and D. D. Awschalom, Nature **453**, 1043 (2008).

[218] E. Knill, Nature **434**, 39 (2005).

[219] N. H. Nickerson, Y. Li, and S. C. Benjamin, Nat. Commun. **4**, 1756 (2013).

[220] L. Trifunovic, O. Dial, M. Trif, J. R. Wootton, R. Abebe, A. Yacoby, and D. Loss, Phys. Rev. X **2**, 011006 (2012).

[221] L. Trifunovic, F. L. Pedrocchi, and D. Loss, Phys. Rev. X **3**, 041023 (2013).

[222] G. Yang, C.-H. Hsu, P. Stano, J. Klinovaja, and D. Loss, Phys. Rev. B **93**, 075301 (2016).

[223] S. Komiyama, H. Hirai, M. Ohsawa, Y. Matsuda, S. Sasa, and T. Fujii, Phys. Rev. B **45**, 11085 (1992).

[224] Y. Ji, Y. Chung, D. Sprinzak, M. Heiblum, and D. Mahalu, Nature **422**, 415 (2003).

[225] T. Stace, C. Barnes, and G. Milburn, Phys. Rev. Lett. **93**, 126804 (2004).

[226] P. Roulleau, F. Portier, P. Roche, A. Cavanna, G. Faini, U. Gennser, and D. Mailly, Phys. Rev. Lett. **100**, 126802 (2008).

[227] E. Bocquillon, V. Freulon, F. D. Parmentier, J. M. Berroir, B. Plaçais, C. Wahl, J. Rech, T. Jonckheere, T. Martin, C. Grenier, D. Ferraro, P. Degiovanni, and G. Fève, Ann. Phys. **526**, 1 (2014).

[228] R. Thalineau, A. D. Wieck, C. Bäuerle, and T. Meunier, arXiv:1403.7770 (2014).

[229] A. Wixforth, J. Scriba, M. Wassermeier, J. P. Kotthaus, G. Weimann, and W. Schlapp, Phys. Rev. B **40**, 7874 (1989).

[230] C. H. W. Barnes, J. M. Shilton, and A. M. Robinson, Phys. Rev. B **62**, 8410 (2000).

[231] J. A. H. Stotz, R. Hey, P. V. Santos, and K. H. Ploog, Nat. Mater. **4**, 585 (2005).

[232] S. Hermelin, S. Takada, M. Yamamoto, S. Tarucha, A. D. Wieck, L. Saminadayar, C. Bäuerle, and T. Meunier, Nature **477**, 435 (2011).

[233] R. P. G. McNeil, M. Kataoka, C. J. B. Ford, C. H. W. Barnes, D. Anderson, G. A. C. Jones, I. Farrer, and D. A. Ritchie, Nature **477**, 439 (2011).

[234] H. Sanada, Y. Kunihashi, H. Gotoh, K. Onomitsu, M. Kohda, J. Nitta, P. V. Santos, and T. Sogawa, Nat. Phys. **9**, 280 (2013).

[235] B. Bertrand, S. Hermelin, S. Takada, M. Yamamoto, S. Tarucha, A. Ludwig, A. D. Wieck, C. Bäuerle, and T. Meunier, Nat. Nanotechnol. **11**, 672 (2016).

[236] M. Pioro-Ladrière, T. Obata, Y. Tokura, Y. S. Shin, T. Kubo, K. Yoshida, T. Taniyama, and S. Tarucha, Nat. Phys. **4**, 776 (2008).

[237] F. Forster, M. Mühlbacher, D. Schuh, W. Wegscheider, and S. Ludwig, Phys. Rev. B **91**, 195417 (2015).

[238] R. Hanson, L. M. K. Vandersypen, L. H. W. Van Beveren, J. M. Elzerman, I. T. Vink, and L. P. Kouwenhoven, Phys. Rev. B **70**, 241304 (2004).

[239] M.-C. Bañuls, J. I. Cirac, and M. M. Wolf, Phys. Rev. A **76**, 022311 (2007).

[240] D. Dasenbrook, J. Bowles, J. B. Brask, P. P. Hofer, C. Flindt, and N. Brunner, New J. Phys. **18**, 043036 (2016).

[241] E. M. Kessler, Phys. Rev. A **86**, 012126 (2012).

[242] H. Christ, J. I. Cirac, and G. Giedke, Phys. Rev. B **75**, 155324 (2007).

[243] W. K. Wootters, Phys. Rev. Lett. **80**, 2245 (1998).

[244] M. D. Shulman, S. P. Harvey, J. M. Nichol, S. D. Bartlett, A. C. Doherty, V. Umansky, and A. Yacoby, Nat. Commun. **5**, 5156 (2014).

[245] C. H. Bennett, G. Brassard, S. Popescu, B. Schumacher, J. A. Smolin, and W. K. Wootters, Phys. Rev. Lett. **76**, 722 (1996).

[246] R. Horodecki, P. Horodecki, M. Horodecki, and K. Horodecki, Rev. Mod. Phys. **81**, 865 (2009).

[247] C. H. Bennett, D. P. DiVincenzo, J. A. Smolin, and W. K. Wootters, Phys. Rev. A **54**, 3824 (1996).

[248] I. Devetak and A. Winter, Proceedings of the Royal Society of London A: Mathematical, Physical and Engineering Sciences **461**, 207 (2005).

[249] A. Auer, R. Schwonnek, C. Schoder, L. Dammeier, R. F. Werner, and G. Burkard, Appl. Phys. B **122**, 51 (2016).

[250] K. Hamaya, S. Masubuchi, K. Hirakawa, S. Ishida, Y. Arakawa, K. Sawano, Y. Shiraki, and T. Machida, Phys. Rev. B **73**, 121304 (2006).

[251] M. Veldhorst, J. C. C. Hwang, C. H. Yang, A. W. Leenstra, B. de Ronde, J. P. Dehollain, J. T. Muhonen, F. E. Hudson, K. M. Itoh, A. Morello, and A. S. Dzurak, Nat. Nanotechnol. **9**, 981 (2014).

[252] O. Viyuela, D. Vodola, G. Pupillo, and M. A. Martin-Delgado, Phys. Rev. B **94**, 125121 (2016).

[253] M. Bukov, L. D'Alessio, and A. Polkovnikov, Advances in Physics **64**, 139 (2015).

[254] C. Müller and T. M. Stace, Phys. Rev. A **95**, 013847 (2017).

[255] J. Dziarmaga, Phys. Rev. Lett. **95**, 245701 (2005).

[256] A. Das, Phys. Rev. B **82**, 172402 (2010).

[257] V. M. Bastidas, C. Emary, G. Schaller, and T. Brandes, Phys. Rev. A **86**, 063627 (2012).

[258] A. Russomanno, A. Silva, and G. E. Santoro, Phys. Rev. Lett. **109**, 257201 (2012).

[259] E. Lieb, T. Schultz, and D. Mattis, Annals of Physics **466**, 407 (1961).

[260] W. DeGottardi, M. Thakurathi, S. Vishveshwara, and D. Sen, Phys. Rev. B **88**, 165111 (2013).

[261] C. W. Gardiner and P. Zoller, *Quantum Noise* (Springer, New York, 2004).

[262] C. W. Gardiner, Optics Communications **243**, 57 (2004).

[263] H. J. Carmichael, Phys. Rev. Lett. **70**, 2273 (1993).

[264] C. W. Gardiner, Phys. Rev. Lett. **70**, 2269 (1993).

[265] M. I. Kolobov and I. V. Sokolov, Optics and Spectroscopy **62**, 69 (1987).

[266] J. I. Cirac, P. Zoller, H. J. Kimble, and H. Mabuchi, Phys. Rev. Lett. **78**, 3221 (1997).

[267] E. A. Chekhovich, M. N. Makhonin, A. I. Tartakovskii, A. Yacoby, H. Bluhm, K. C. Nowack, and L. M. K. Vandersypen, Nat. Mater. **12**, 494 (2013).

[268] J. M. Taylor, J. R. Petta, A. C. Johnson, A. Yacoby, C. M. Marcus, and M. D. Lukin, Phys. Rev. B **76**, 035315 (2007).